Author/s:
Ventura, Emanuele Maria

Title:
From primordial clouds to first light: modeling and detecting Population III stars in the early Universe

Date:
2025

Persistent Link:
https://hdl.handle.net/11343/361256

From Primordial Clouds to First Light: Modeling and Detecting Population III Stars in the Early Universe

Emanuele Maria (Manu) Ventura
ORCID 0000-0003-3502-4929

July, 2025

A thesis submitted in complete fulfilment
of the requirements for the degree of

Doctor of Philosophy
Physics
The University of Melbourne

"Il segreto è fare come gli alberi: prima cerchi e dopo tronchi."
— Caparezza, Exuvia —

Abstract

The formation of the first stars—Population III (Pop. III) marks a fundamental transition in cosmic history, transforming the Universe from a dark, metal-free environment into one shaped by radiation, feedback, and chemical enrichment. These primordial stars, formed out of pristine gas in mini-halos, are thought to have played a vital role in initiating reionization and enriching the intergalactic medium with the first heavy elements. However, due to their transient nature and high redshift, direct observations of Pop. III stars remain elusive.

This thesis presents a comprehensive investigation into the formation, evolution, and observability of Pop. III stars through a combination of semi-analytical modeling and cosmological simulations. In this thesis I extend the MERAXES semi-analytical framework to incorporate Pop. III star formation by modeling molecular hydrogen cooling, Lyman-Werner feedback, streaming velocities, and both internal and external metal enrichment. In particular, I implement a physically motivated model for the spatial propagation of metals into the intergalactic medium and its effects on subsequent star formation, enabling us to track the Pop. III to Pop. II transition self-consistently.

With this updated version of MERAXES, I explore how Pop. III stars influence the UV luminosity function of high-redshift galaxies. After exploring a wide parameter space, I demonstrate that Pop. III-dominated galaxies may be observable by the James Webb Space Telescope under optimistic assumptions about the Pop. III initial mass function and star formation efficiency. I also show that accurate treatment of metal enrichment, particularly external pollution from nearby halos, has a strong impact on the duration and prevalence of Pop. III star formation during the Epoch of Reionization.

Then, I investigate the large-scale consequences of Pop. III stars on the 21cm global signal and power spectrum during the Cosmic Dawn and Epoch of Reionization. Based on the new version of MERAXES, I develop a novel method to bridge the gap between small-volume, high-resolution simulations and large cosmological boxes by calibrating star formation scaling relations and applying them to extended volumes. I show that variations in Pop. III star formation parameters, primarily in the initial mass function and X-ray heating, significantly affect the timing and amplitude of 21cm fluctuations. These differences, especially at $z \lesssim 10$, will be likely detectable with future deep observations by the Square Kilometre Array.

By combining physically motivated modeling with state-of-the-art simulations, this thesis sheds light on the role of Pop. III stars in early galaxy formation and their potential observational signatures. The results underscore the promise of current and upcoming facilities such as JWST and SKA in probing the Universe's first luminous sources and advancing our understanding of the earliest stages of cosmic history and galaxy formation.

Declaration

This page certifies that:

- This thesis contains only original work towards a Doctor of Philosophy, except where indicated in the preface
- Due acknowledgement has been made in the text to all other material used
- This thesis is fewer than 100 000 words in length, exclusive of tables, figures, bibliographies, and appendices

Emanuele Maria Ventura

Preface

Here and henceforth, "the author" refers to Emanuele M. Ventura, the author of this thesis. This thesis is an original work by the author reporting research done alone or in collaboration with other authors. This section provides a chapter-by-chapter summary of the author's contributions and the publication status of all material.

Chapter 1 provides the cosmological framework including the theory of ΛCDM and galaxy formation and it is written by the author for this thesis. It is an original work of the author, with editing from Y. Qin and J. S. B. Wyithe, and has not been submitted for publication.

Chapter 2 is a comprehensive literature review on Population III stars including theory of Pop. III star formation and observational probes. It is an original work of the author, with editing from Y. Qin and J. S. B. Wyithe, and has not been submitted for publication.

Chapter 3 is based on the published work *E. M. Ventura, Y. Qin, S. Balu, J. S. B. Wyithe, Monthly Notices of the Royal Astronomical Society, Volume 529, Issue 1, March 2024, Pages 628–646.* It was written primarily by the author, with scientific input and editing from the co-authors. The author was responsible for developing and generating the simulations and data analyses. All figures and tables are the work of the author.

Chapter 4 is based on a preliminary draft of work in preparation to be published *E. M. Ventura, A. Venditti, R. Schneider, V. Bromm, J. B. Muñoz, J. S. B. Wyithe, Monthly Notices of the Royal Astronomical Society* It was written primarily by the author, with scientific input and editing from the co-authors. The author was responsible for developing and generating the simulations and data analyses. All figures and tables are the work of the author.

Chapter 5 is based on the published work *E. M. Ventura, Y. Qin, S. Balu, J. S. B. Wyithe, Monthly Notices of the Royal Astronomical Society, Volume 540, Issue 1, June 2025, Pages 483–497.* It was written primarily by the author, with scientific input and

editing from the co-authors. The author was responsible for developing and generating the simulations and data analyses. All figures and tables are the work of the author.

Chapter 6 summarises the work in the previous chapters. It includes some exploratory future directions for the work in this thesis. It was written by the author, with editing from Y. Qin and J. S. B. Wyithe.

The author also led another publication during their PhD candidature, which is not included for examination in this thesis but is listed here for completeness:

- *E. M. Ventura, A. Trinca, R. Schneider, L. Graziani, R. Valiante and J. S. B. Wyithe, Monthly Notices of the Royal Astronomical Society, Volume 529, Issue 3, April 2023, Pages 3609-3625.* It was written primarily by the author, with scientific input and editing from the co-authors. The author was responsible for data analyses and post-process of the numerical simulations. All figures and tables are the work of the author.

The author acknowledges funding support through the Australian Research Council Centre of Excellence for All Sky Astrophysics in 3 Dimensions (ASTRO 3D) through project #CE170100013. The works in this thesis utilized the OzSTAR national facility at the Swinburne University of Technology. The OzSTAR program partially receives funding from the Astronomy National Collaborative Research Infrastructure Strategy (NCRIS) allocation provided by the Australian Government. This thesis was also undertaken with the assistance of resources from the National Computational Infrastructure (NCI Australia), an NCRIS-enabled capability supported by the Australian Government. The author is supported by a Melbourne Research Scholarship, which includes a fee offset.

Acknowledgments

The 7^{th} of January 2022 I landed in the down under. I would have never imagined three and half years later I would have think to call this place home. It would be extremely arrogant to say that whatever I accomplished in the past 3 years and half is solely because of me and my hard work. For this reason I want to spend a few words properly acknowledging all the people that walked with me in this journey. Academically or personally. I am an extremely lucky person.

To Gianni, Edu and Elo: my second family here in Melbourne
Everything started from a random phone video call while I was still in Italy and me sending the deposit to a perfect stranger without having seen the house in person. That was one of the best decision of my life. We shared a home for almost two years. Thank you for being there, for all the cooking, movie and game nights and all the parties. I could not have hoped for better flatmates. I love y'all.

To Tommaso
The first and only contact I had in Melbourne before I arrived. I met you as a brother of the flatmate of a good friend. Now you are simply one of my best friends in Melbourne.

To Marina, Jordi, Edèl, Mai, Karen
For all the pizzas, the camping weekends, dinners and sauna sessions. To prove why catalan (or spanish) speakers are the best people in the world.

To all the ROC popular club members
For patiently belaying me and still allow me to join awesome climbing trips even though my climbing skills get progressively worse. For all the Arapiles weekends and the pizzas at the Natimuk oven. A special mention to Alex for being the best meat chef that I know and to Lizzie for your contagious positive energy.

To all the non-astro people who welcomed me in the first year of my australian life: Praj, Celia, Oceane, Kenya, Sinny, Mariella, Lana, Liam, Rayanna, Sammy, Martin, Charles, Andrew, Jess. Thanks for all the parties and the fun memories.

To Yuxiang Giacomo Qin
For simply being the best supervisor, collaborator and friend I could have asked for. Thanks for pushing me to give my best, for helping me with my projects and for always being genuine and supportive.

To Raffaella Schneider
The most important academic mentor. Without you I would have never started a PhD. For your guidance since my beginning as a researcher helping me with my very first paper and presentation.

To Michele Trenti
For all the scientific inputs and being a mentor. For the coffee machine that significantly improved the astro-floor.

To Stuart Wyithe
For providing great guidance over the past three years and significantly improving my science and papers.

To Simon Mutch and Bradley Greig
I arrived in Melbourne with zero knowledge of C and proper coding. Thanks for all the help in setting up, running and finally publishing MERAXES.

To Chris Power
For being an amazing collaborator. Thank you for providing all the complicated N-body simulations. Without those, my project would have never existed.

To Balu Carlo Pio Sreedhar
For guiding me as an older academic brother. For all the dinners when I was down, when the code was not working and the hardest times. For cheering me up, for partying with me and for helping me to improve my science.

To Alessandra
A friend, a collaborator and one of the smartest people I know.

To Andrès Felipe Vargas Sanchez
For being a friend, a model and a real caballero. Thank you for all the chats at the benches, for your positive attitude and for being the papa of the astro department. Without you my PhD would have been way more boring.

To Gio
For starting and finishing this journey together. For sharing the office. For all the good scientific prompts you gave me. For all the stimulating conversations. For being a good friend.

To Nico
For being a good friend inside - but most importantly - outside the office. For the 6am runs. For sharing with me the burden and the joy of organizing holidays, parties and weekends away.

To Justin
For sharing many lunches, morning coffees, pool games and the struggles (but also the perks) of the PhD life.

To Aadarsh
For being a fantastic groupmate. For *la cazza* and all the funny memories.

To the legend
For being a legend and a trustworthy drinking, climbing and poker mate.

To all the astro people that shared a part of this journey with me: Eduardo, Sonja, Filippo, Sarita Maria, Joe, Aman, Behzad, Kevin, Oliver, Kit, Nicha, Christine, Liam, Jiayi, Tree, PK, Arwa, Haritha, Firda, Steven, Sruthi, Tong, Benji, Matt, Hudson, Cameron, Ash, Jenn. Thanks for the coffees/volleyball matches/meetings and Clyde sessions we shared.

Un grazie infinito a chi c'è stato da prima che venissi quì. Ai tantissimi amici che sono fortunato di avere, che mi hanno accompagnato da casa anche solo con una chiamata o un messaggio. A Max, Maria, Chiara, Lorenzo, Anna e Francesco che sono venuti a trovarmi dall'altro lato del mondo. Ad Antonio per esserci stato nei momenti più critici nonostante la distanza ed il fuso orario. Ad Ale, Cheno, Marco, Gio, Anna, Livia, Luca e Pompa perchè la distanza non è stata sufficiente a separarci.

A mamma e papà. So che vi ho messi a dura prova andando dall'altra del mondo. Per farmi credere in me stesso, per spronarmi a non accontentarmi, per insegnarmi l'importanza di essere onesti e sinceri. Per avermi messo nelle migliori condizioni possibili.

Ad Ilaria. Per gli 8 anni insieme e tutti quelli a venire. Per aver rischiato molto. Per essere la mia persona preferita e colei con cui spero di passare il resto della mia vita.

A final note on Caparezza, a great artist who captured the struggling of making choices. *Un dubbio mi tallona e mi sta addosso. Sarò già stufo di ogni mia canzone, ma canto per nutrire un paradosso? E mentre mi tormenta la questione, due strade si diramano dal parco; ciascuna custodita da un piantone. Il primo Ludovico, l'altro Marco. Discorrono per darmi un buon consiglio; ciascuno caldeggiando il proprio varco.*

Contents

List of figures

List of Tables

CHAPTER 1

A brief history of the Universe

Camina, guerrero camina

Por el sendero del dolor, Y la alegría

Caparezza - Sendero (2021)

1.1. "Let there be light," and there was light.

Over the past few decades, our understanding of the early Universe has significantly advanced, largely due to detailed studies of the Cosmic Microwave Background (CMB), such as those conducted by the Planck mission (Planck Collaboration et al. 2016, 2020). In addition, numerous surveys across a wide range of wavelengths have provided valuable insights into the formation and characteristics of local cosmic structures. Despite these achievements, a key chapter in the Universe's history remains unclear: how did the first luminous objects emerge, and what role did they play in shaping the large-scale structure of the cosmos?

During its first hundred million years, between the last scattering surface of the CMB and formation of first stars, the Universe was a cold and dark place (i.e. "The Dark Ages"). Then, the first stars lighted on. The so-called Population (Pop.) III stars are the

first luminous sources in the Universe. These stars born out of metal-free cloud (the Big Bang nucleosynthesis produced only H and He along with few traces of Li) and provided the first *metals* (all elements heavier than He) for the second-generation of stars (i.e. Pop. II stars). Despite their key importance, we know very little about these elusive objects as no observation of a metal-free star has been confirmed.

In the last decade, thanks to the availability of powerful computing clusters and the development of advanced numerical technique, we started to detail modeling the first episodes of star formation including a number of physical effects such as molecular gas cooling, radiative feedback, magnetic fields and primordial streaming velocities. Any realistic model of Pop. III star formation needs to take into account all of these processes since the formation of the first stars is no simpler than present day stellar birth. The arrival of cutting-edge observatories like the "James Webb Space Telescope" (JWST), the Hydrogen Epoch of Reionization Array (HERA) and Euclid, together with the future generation "Extremely Large Telescope" (ELT), and the Square Kilometer Array (SKA) we are now looking through the keyhole of the Universe in its first few hundreds million years revising our views on early galaxy formation and hoping to finally witness the onset of the first stars.

In this chapter, I first introduce (section 1.2) the relevant concepts of the ΛCDM concordance model of cosmology, and then, in section 1.3, I summarise how the first structures formed in the Universe including both dark matter halos and the first baryons. In section 1.4 I provide a review of the Epoch of Reionization, a key event in the Universe's evolution happened in its first billion years. Finally, in the last two sections I summarise how our knowledge of the Early Universe has significantly improved in the last few years thanks to the advanced numerical simulations (1.5) and to the cutting-edge observations of JWST (1.6). Within section 1.5 there is also a subsection entirely devoted to the semi-analytical model MERAXES (see 1.5.3) which has been co-developed and extensively used by the author for the research topics discussed in this thesis. This first chapter closely follows Peebles (1980); Barkana & Loeb (2001); Mo et al. (2010). The interested reader is urged to consult these for a historical and comprehensive overview.

1.1.1. *A few useful quantities*

Before diving into the introduction, I will define here a few useful quantities that are often referred to in this thesis.

- **Proper** and **comoving** coordinates:

  Due to the expansion of the Universe, the distance between any two points in space will increase with cosmic time. If one measures the coordinates using a fixed reference system, these coordinates will change with cosmic time and these are referred as *proper coordinates* (**r**). On the other hand, if one measures the coordinates with a system whose grid lines also expand with that of the Universe, then, in the absence of peculiar motion, the coordinates will remain fixed in time. These coordinates are defined as *comoving coordinates* (**x**) and are the ones in which an observer moves along the Hubble expansion. The relation between the two is $\mathbf{r}(t) = a(t)\mathbf{x}$ where $a(t)$ is the scale factor of the Universe. At the present day the scale factor is $a(t_0) = 1$ such that comoving and proper coordinates are equivalent.

- **Cosmological redshift** z**:**

  Cosmological redshift refers to the shift towards longer wavelengths of any spectral line due to the expansion of the Universe. The cosmological redshift is given by $z = \frac{\lambda - \lambda_0}{\lambda_0}$ with λ_0 and λ the rest-frame and the observed wavelength respectively. The cosmological redshift is related to the scale factor through $a(t) = (1+z)^{-1}$.

1.2. The ΛCDM model

The standard cosmological model (ΛCDM) describes the Universe as homogeneous, isotropic, and expanding, with its energy content dominated by dark energy — driving the accelerated expansion — and most of its matter existing as Cold Dark Matter (CDM). This spacetime is described by Robertson-Walker metric (Robertson 1935; Walker 1937), usually written using comoving spherical coordinates (R, Θ, Φ):

$$ds^2 = dt^2 - a^2(t)\left[\frac{dR^2}{1-kR^2} + R^2(d\Theta^2 + \sin^2\Theta d\Phi^2)\right]. \tag{1.1}$$

The value of the constant k relates to the global curvature of the Universe: it is negative for an open Universe, positive for a closed Universe, and zero for a flat Universe. From the scale factor $a(t)$, it is useful to define the rate of expansion of the Universe using the Hubble parameter $H(t) = \frac{\dot{a(t)}}{a(t)}$. By solving the Einstein Field Equations of General Relativity using the Robertson-Field metric in Eq. 1.1, the Friedmann equation is obtained:

$$H^2(t) = \frac{8\pi G}{3}\rho - \frac{k}{a^2}. \tag{1.2}$$

This relation, together with the equation of energy conservation:

$$d(\rho R^3) = -p d(R^3) \tag{1.3}$$

relates the expansion of the Universe to its energy-matter content via the total energy density (ρ) and pressure (p). An useful quantity often used in cosmology is the critical density ρ_c defined by taking $k = 0$ in Eq. 1.2:

$$\rho_c = \frac{3H^2(t)}{8\pi G}. \tag{1.4}$$

It is now possible to rewrite Eq. 1.2 using the ratio of the density of each source - matter (m), radiation (r), dark energy or cosmological constant (Λ) and curvature (k) - with respect to the critical density ($\Omega_{i=[m,r,\Lambda,k]} = \frac{\rho_i}{\rho_c}$):

$$H(t) = H_0\left[\frac{\Omega_r}{a^4} + \frac{\Omega_m}{a^3} + \frac{\Omega_k}{a^2} + \Omega_\Lambda\right]^{1/2} \tag{1.5}$$

where the subscript '0' refers to the values of these parameters in the present day (H_0 is usually referred to as *Hubble constant*).* At the present day, the main contributions to the energy density come from the cosmological constant ($\Omega_\Lambda \simeq 0.75$) and matter ($\Omega_m \simeq 0.25$). Eq. 1.5 is often written accounting only for these two contributions and as a function of redshift instead of time using $a(t) = (1+z)^{-1}$. Hence, throughout this

*The Hubble's constant is often expressed in literature and sometimes in this thesis as $H_0 = 100h$ km s^{-1} Mpc^{-1}.

thesis the following expression will be used:

$$H(z) = H_0[\Omega_\Lambda + \Omega_m(1+z)^3]^{1/2}. \tag{1.6}$$

1.3. Structure formation

The ΛCDM model provides the initial conditions necessary for cosmic structure formation. In the framework of the Hot Big Bang, the early Universe was extremely hot and dominated by radiation. As it expanded and cooled adiabatically, matter began to dominate the energy density around redshift $z \sim 10^4$. During this radiation-to-matter transition, temperatures were still high enough to keep the primordial gas ionized. However, by $z \sim 1100$, the temperature had fallen below $3300,\mathrm{K}$, enabling hydrogen recombination (e.g. Eisenstein et al., 2005). Once protons and electrons combined into neutral hydrogen, photons decoupled from matter and began to travel freely—forming the cosmic microwave background (CMB), the oldest observable light in the Universe.

While the present-day Universe displays a complex, hierarchical network of galaxies and clusters, CMB observations reveal that the Universe at recombination was remarkably uniform, with only tiny density fluctuations on the order of 10^{-5} (e.g. Planck Collaboration et al., 2016). These small perturbations grew over time through gravitational instability: initially in the linear regime, as overdense regions attracted surrounding matter, and later evolving into non-linear structures that ultimately formed galaxies and galaxy clusters (Peebles, 1980).

1.3.1. Linear growth

Let us consider a flat universe with uniform matter density $\bar{\rho}$ and, on top of this, some small perturbations with fractional amplitude $|\delta| << 1$ where $\delta = \frac{\rho}{\bar{\rho}} - 1$ as set by the CMB observations. Under these approximations, the evolution of such perturbations can be described using the linear perturbative approach. Treating the matter density field as an ideal fluid, its behaviour follows a set of four equations known as:

1. *Continuity equation* (or mass conservation)

$$\left.\frac{\partial \rho}{\partial t}\right|_{\bar{r}} + \bar{\nabla}_{\bar{r}}(\rho \bar{v}) = 0 \tag{1.7}$$

2. *Euler equation* (or momentum conservation)

$$\left.\frac{\partial \bar{v}}{\partial t}\right|_{\bar{r}} + (\bar{v} \cdot \bar{\nabla}_{\bar{r}})\bar{v} + \frac{1}{\rho}\bar{\nabla}_{\bar{r}} P + \bar{\nabla}_{\bar{r}}\Phi = 0 \tag{1.8}$$

3. *Poisson equation*

$$\nabla^2_{\bar{r}}\Phi = 4\pi G\rho \tag{1.9}$$

4. *Equation of State* (EOS)

$$P = P(\rho) \tag{1.10}$$

where P is pressure, Φ is the gravitational potential and all the quantities are written in proper coordinates. In a cosmological context these equations can be rewritten in comoving coordinates (Gamow & Teller 1939) such that $\bar{v} = \dot{\bar{r}} = H\bar{r} + \bar{u}$ where $\bar{u} = a\dot{\bar{x}}$ is the peculiar velocity due to the proper motion of the fluid. With the linear perturbative approach, the above equations in comoving coordinates can be rewritten using the perturbed quantities, then linearized and finally solved in the Fourier space. The evolution of the density perturbations is hence written as:

$$\frac{\partial^2 \delta_k}{\partial t^2} + 2H\frac{\partial \delta_k}{\partial t} + (k^2 v_s^2 - 4\pi G\bar{\rho})\delta_k = 0 \tag{1.11}$$

where k is the wave number and $v_s^2 = c_s^2/a^2$ with c_s the adiabatic speed of sound. Note that this is essentially the same result found in the *Jeans theory* (Jeans 1902) who first described the evolution of spherical overdensities at various scales within a uniform fluid. Such an evolution is the determined by the competing effects of free streaming (given by the term $k^2 v_s^2 \delta_k$) which damps the perturbations and the gravitational instability ($-4\pi G\bar{\rho}$) which makes the perturbations grow. In a cosmological context there is the additional term $2H\frac{\partial \delta_k}{\partial t}$ due to the expansion of the Universe. In a matter dominated Universe, any given perturbation δ_k with $k << k_J$ ($k_J \equiv \frac{\sqrt{4\pi G\bar{\rho}}}{v_s}$ i.e. the *Jeans wave number*)

grows in time (or redshift) following the growth factor $D(z)$[†] and maintaining its shape (in comoving coordinates).

Once the time evolution of the individual Fourier modes δ_k is known, the evolution of the density field can be computed knowing that the density field is a superposition of a complete set of periodic Fourier modes, each evolving independently. This arises from the fact that, according to modern cosmology, the initial perturbations are generated by inflation (a period of rapid accelerated expansion of the very Early Universe) and are distributed according to a Gaussian random field (Kolb & Turner 1990) such that

$$\delta_{\bar{k}} = \int d^3x \delta(\bar{x}) e^{i\bar{k}\cdot\bar{x}}. \tag{1.12}$$

Like any other random field, the density field can be described using the Power Spectrum $P(k)$ defined from the two point correlation function. Standard models of inflation predict a primordial matter power spectrum $P_{\rm pri}(k) \propto k^{n_s}$ with $n_s \simeq 1$[‡] (Harrison 1970; Zeldovich 1972). Hence, while in linear regime, $P(k,z) \propto P_{\rm pri}(k)D(z)$. From this picture it arises the so-called *bottom-up* or *hierarchical* scenario of structure formation (i.e. the size of the collapsed structures being formed out of gravitational collapse gets bigger with time).

Finally, to determine the size (or mass) of a collapsed object, the variance σ^2 of the density field smoothed with a spherical top-hat filter is computed. This is given by:

$$\sigma^2(M) = \sigma^2(R) = \int_0^\infty \frac{dk}{2\pi^2} k^2 P(k) \left[\frac{3j_1(kR)}{kR}\right]^2 \tag{1.13}$$

where j_1 is the first order Bessel function and the above integral is normalised to the value of $\sigma_8 = \sigma(R = 8h^{-1}\ \text{Mpc})$ inferred from observations (Planck Collaboration et al. 2020).

[†]This is obtained as one of the two indipendent solutions of Eq. 1.11. For a detailed derivation of these solutions we refer the reader to Peebles (1980).

[‡]Measurements from Planck Collaboration et al. (2020) found it to be indeed very close to 1 (0.96).

1.3.2. *Non-linear regime and dark matter halos*

When the overdensities grow and δ approaches 1, the linear approximation breaks and the individual k modes cease to be independent. At this point, the growth of the first structures cannot be followed analytically[§] and dark matter N-body simulations are essential. These are particularly crucial to follow the formation of the *dark matter halos*: the first building blocks of galaxies.

A dark matter halo is a stable, self-gravitating structure of gravitationally bounded dark matter particles. This is achieved with a violent dynamical relaxation process denoted as virialization. A dark matter halo is characterised by its virial properties like its virial radius ($r_{\rm vir}$), circular velocity ($V_{\rm vir}$) and temperature ($T_{\rm vir}$) all linked to the virial mass ($M_{\rm vir}$) and to the final overdensity relative to the critical density ($\Delta_c = 18\pi^2 + 82[\Omega_m(z) - 1] - 39[\Omega_m(z) - 1]$, Bryan & Norman 1998) as follows (Barkana & Loeb 2001):

$$
\begin{aligned}
r_{\rm vir} &= 0.784 \left[\frac{\Omega_m \Delta_c}{\Omega_m(z) 18\pi^2}\right]^{-1/3} \left(\frac{M_{vir}}{10^8 h^{-1} M_\odot}\right)^{1/3} \left(\frac{1+z}{10}\right)^{-1} h^{-2/3} \ {\rm kpc} \\
V_{\rm vir} &= \left(\frac{GM}{r_{vir}}\right)^{1/2} = 23.4 \left(\frac{M_{vir}}{10^8 h^{-1} M_\odot}\right)^{1/3} \left[\frac{\Omega_m \Delta_c}{\Omega_m(z) 18\pi^2}\right]^{1/6} \left(\frac{1+z}{10}\right)^{1/2} \ {\rm km\ s^{-1}} \\
T_{\rm vir} &= \frac{\mu m_p V_{vir}^2}{2 k_B} = 1.98 \times 10^4 \left(\frac{\mu}{0.6}\right) \left(\frac{M_{vir}}{10^8 h^{-1} M_\odot}\right)^{2/3} \left[\frac{\Omega_m \Delta_c}{\Omega_m(z) 18\pi^2}\right]^{1/3} \left(\frac{1+z}{10}\right) {\rm K}
\end{aligned}
\tag{1.14}
$$

where μ is the mean molecular weight.[¶]

N-body simulations come handy also to investigate the density profile of dark matter halos. The most widely adopted is the Navarro-Frenk-White (NFW) profile (Navarro et al. 1996) which has been verified by many numerical simulations. For small and large radii, the NFW profile is often corrected with the Einasto profile (Einasto 1965) which mitigates the problem of the central r^{-1} cusp.

Finally, after characterizing the properties of each individual dark matter halo, only their statistics is left to investigate. This is described by the number density of dark

[§]Except for a few simple and highly symmetric cases like the spherical collapse (see e.g. Gunn & Gott 1972).

[¶]Its value is set by the chemical composition and ionization state of the gas. For a primordial gas cloud typical values are $\mu \simeq 0.59$ for a fully ionized gas and 1.22 for a neutral gas.

matter halos as a function of their virial or, in short, the halo mass function. This can be predicted analytically with the Press-Schechter (PS) formalism (Press & Schechter 1974). In short, the PS approach estimates the fraction of dark matter particles that are part of a collapsed halo of a certain mass from the smoothed overdensity field (Eq. 1.13) by integrating the Gaussian density field beyond a critical density threshold δ_c. Despite being fully analytical, the PS halo mass function is fairly accurate at low redshift although numerical simulations are necessary for more precise results especially at high redshift. Popular corrections to the PS halo mass function that give a better agreement with numerical simulations can be found in Sheth et al. (2001); Tinker et al. (2008); Watson et al. (2013).

1.3.3. *Baryonic matter and the first galaxies*

If galaxies were made only out of dark matter, the Universe would be a rather dark and cold place. Despite constituting only $\sim 4\%$ of the total matter, baryons assemble into galaxies and their main components (gas, stars and dust) and are the only observable part in the Universe.

The theory of galaxy formation is rather complex due to the numerous physical processes that operates on a wide range of scales (from sub-parsec to Mpc, see e.g. Fig. 1.1). However, there have been a number of attempts to build a general framework of galaxy formation that can explain the rich morphology of galaxy that we observe today and their evolution. The first attempt of a comprehensive theory of galaxy formation was outlined by White & Rees (1978). These frameworks are the foundation for the numerical simulations of galaxy formation, in particular for *semi-analytical models* which will be discussed in Section 1.5.1. Without dwelling into too main details, here I will summarise only the key processes relevant to form a galaxy and we refer the reader to Mo et al. (2010) for a complete review.

When a dark matter halo collapses[‖] (as discussed in 1.3.2) the baryonic matter bounded

[‖]In reality we would expect to have a mixture of dark matter and baryon particles bounded together. When this is considered, the Jeans mass for a gaseous halo can be derived analytically. A more accurate description of gas uses the filtering mass, which accounts for the time-averaged Jeans effect (see more in Gnedin & Hui 1998 and in Section 2.1). These critical masses sets the minimum mass for a gaseous halo $\sim 10^{5-6} M_\odot$ at $z \sim 30 - 40$.

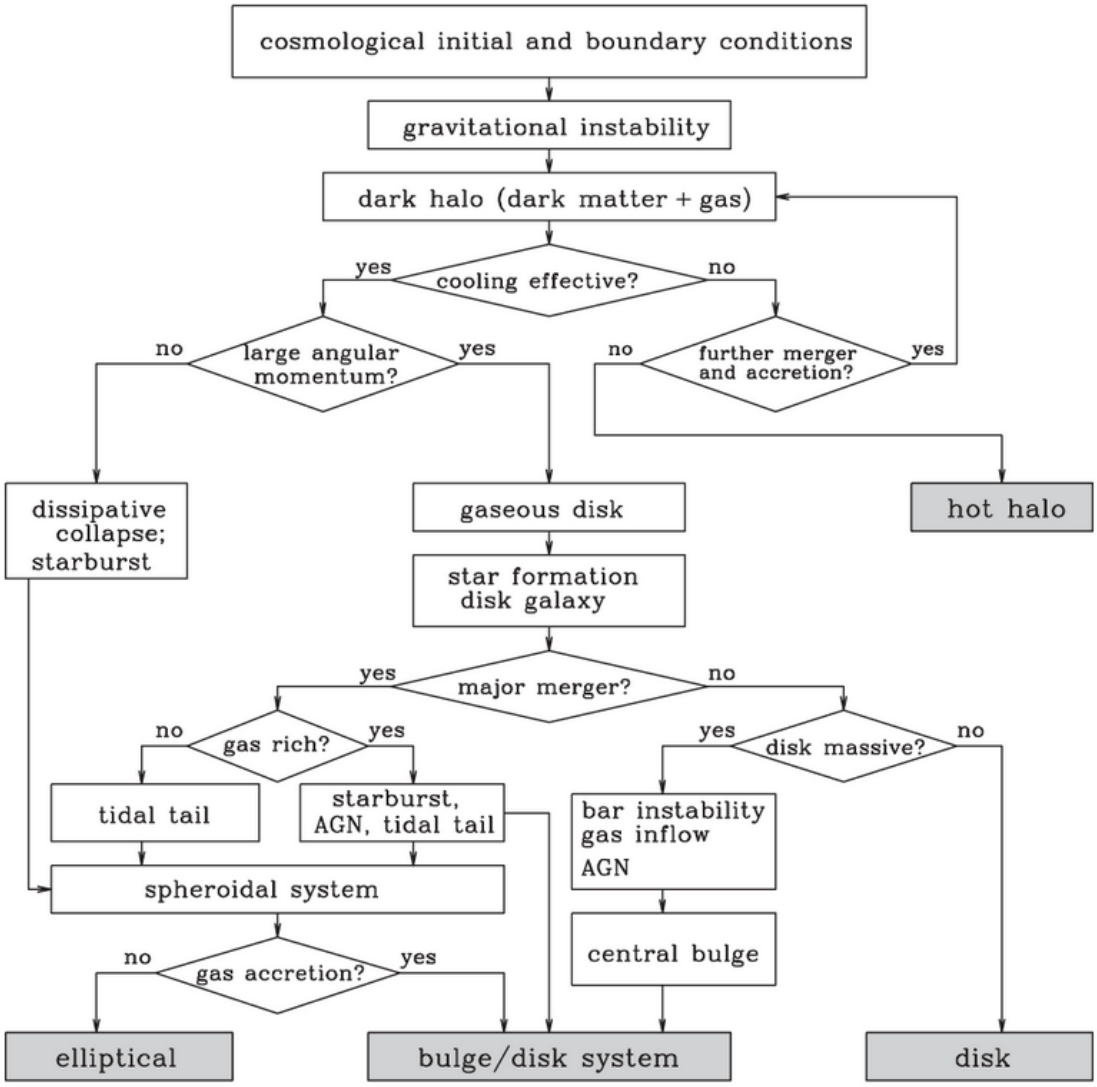

Figure 1.1: A logic flow chart for galaxy formation. In the standard scenario, the initial and boundary conditions for galaxy formation are set by the cosmological framework. The paths leading to the formation of various galaxies are shown along with the relevant physical processes. Adopted from Mo et al. (2010).

to that halo is shocked to its virial temperature T_{vir} and can settle into hydrostatic equilibrium in the potential well of the halo.

In order to form galaxies, the gas has to cool down and settle on a disk-like structure towards the mid-plane of the halo. Depending on the halo mass (or virial temperature), there are different cooling mechanisms. For low-mass halos ($T_{vir} < 10^4 K$, i.e. *mini-halos*) the gas is expected to be neutral and cooling is possible only through excitation/de-excitation lines of heavy elements or roto-vibrational lines of molecules. This latter mechanism is particularly important in pristine halos where H_2 is the main coolant (see discussion in Section 2.1). For halos with $10^4 K \leq T_{vir} \lesssim 10^6 K$, line cooling due to atoms recombinations from a collisionally ionised medium is particularly effective. In a pristine gas only H and He are available while in chemically enriched halos metal lines are very effective coolants (see Sutherland & Dopita 1993). Finally, for halos with $T_{vir} \gtrsim 10^{6-7} K$ the gas is fully ionized and it cools down via bremsstrahlung emission from free e^-. In all these halos, at $z \gtrsim 6$ (when electrons are hotter than the CMB) an additional cooling channel is provided by inverse Compton scattering of CMB photons.

After the gas has settle down onto a disk, cold and dense molecular clouds can form. A gravitational instability in these clouds will trigger a runaway collapse which increases the density and temperature of the gas. As this collapse proceeds, the gas cloud fragments into smaller high density cores that eventually form stars.

The life cycle of a galaxy is heavily impacted by its stars as they enrich the interstellar medium with metals (through stellar winds and supernovae explosions, i.e. *chemical feedback*) and eject gas through powerful supernovae explosion from the interstellar medium (ISM) to the circumgalactic medium (CGM). The process of gas cycling between different phases within the galaxy and in the intergalactic medium (IGM) is often referred to as *baryon cycle*. Other processes that are relevant in a galaxy is the feedback from its central supermassive black hole (AGN feedback) and mergers with other galaxies. All these processes listed here ultimately determine how a galaxy evolves and assemble in cosmic time.

1.4. The Epoch of Reionization

The formation of the first stars not only affects their host galaxies but it changes the state of the IGM. The main constituent of the Universe is hydrogen ($\sim 75\%$ of the total baryonic mass). After the recombination and up until the first galaxies form, the Universe is filled with neutral hydrogen. As soon as the first stars light up, these will start emitting photons with $\lambda \leq 912$ Å that eventually escape the host galaxy and ionize the HI in the IGM. By $z \sim 5$[**] the whole IGM became fully ionized. This event marks the last major phase transition in the Universe and it is referred to as *Epoch of Reionization* (EoR).

This phase transition is mostly studied using Lyman-α photons. The Lyman-α line is a strong UV emission line of the hydrogen atom at 1216 Å corresponding to a transition between the energy level $n = 2$ to $n = 1$. Lyman-α photons are very sensitive to neutral hydrogen, both in the ISM and the IGM and even small fractions of HI can suppress this emission (Gunn & Peterson 1965). The first evidence for the reionization was provided by the *Gunn-Peterson trough* (i.e. a spectrum in which all photons with $\lambda < 1216$ Å are absorbed) in the SDSS quasar spectra by Becker et al. (2001).

In the last twenty years many observational probes have been used to study the EoR. These focus on constraining the evolution of the neutral hydrogen fraction (x_{HI}) during $z \sim 12 - 5$. The main ones are summarised below including the 21cm signal to which, given the importance for this thesis, is dedicated a separate subsection.

1.4.1. Observational probes and constraints

Quasar absorption spectra

Given their large brightness, quasars are ideal candidates to probe the ionization state of the IGM. While observing their trough at $z \gtrsim 6$ just proves the presence of HI, its fraction can be constrained by looking at the *damping wings* (i.e. extended absorption redward of the Lyman-α line) and the *dark pixels* (i.e. pixels with no detectable flux blueward of the Lyman-α line). The former is sensitive to larger x_{HI} ($\sim 0.4 - 0.7$ at

[**]The exact timing at which reionization is completed is still debated although there is increasing evidence that the whole process finished around z$\simeq$ 5.3 (see e.g. Bosman et al. 2022).

$z \sim 7$ e.g. Davies et al. 2018; Wang et al. 2020; Greig et al. 2022; Spina et al. 2024) while the latter provides conservative upper limits on the neutral fraction towards the end of the EoR (e.g. $x_H \lesssim 0.06$ at $z \sim 5.9$ as shown in McGreer et al. 2015). Damping wings can also be observed in other bright sources such as Gamma Ray Bursts (GRB, e.g. Totani et al. 2014).

Lyman-α emission from galaxies

Galaxies whose Lyman-α emission is visible are referred to as Lyman-α emitters (LAE). By looking at the distribution of the equivalent width of Lyman-α lines from galaxies at $z \sim 7-8$ it can be inferred that the reionization is still proceeding with $x_{HI} \sim 0.4-0.8$ (see e.g. Mason et al. 2019; Hoag et al. 2019; Jung et al. 2020). Alternatively one can look at the Lyman-α luminosity function (the number density and brightness of LAEs) which exhibits a sharp decline at $z \sim 7$ providing similar constraints to the ones from the equivalent width (see e.g. Ouchi et al. 2010; Umeda et al. 2024).

CMB

CMB observations can help constraining the duration and timing of the EoR through measurements of the integrated Thompson scattering optical depth (τ_e). This quantifies the probability that a CMB photon scattered off free electrons on its way from the surface of last scattering to us. This can be estimated as:

$$\tau_e = \int_0^z dz' \left| c \frac{dt'}{dz'} \right| \sigma_T n_e(z') \tag{1.15}$$

where n_e the number density of free electrons and σ_T the Thomson cross section. This quantity has been measured by the Planck mission (Planck Collaboration et al. 2020) and its state-of-the-art value is set at $\tau_e = 0.054 \pm 0.007$ disfavouring an early reionization.[††].

[††]Although this might be in tension with the abundance of very high-z galaxies detected with JWST, see Muñoz et al. (2024) for an interesting discussion.

1.4.2. 21cm signal

An extremely powerful probe of the Universe between the recombination and the reionization is the hyperfine spin-flip HI transition or, in short, *21cm line* (see Furlanetto et al. 2006; Pritchard & Loeb 2012; Liu & Shaw 2020 for detailed reviews). Despite being a forbidden line, since the Universe is filled with neutral hydrogen before the reionization is completed, it is often detected in many astrophysical sources. As the name suggests, this transition produces radiation at a rest-frame wavelength of 21cm (low-frequency radio). The observed brightness temperature of the 21cm line is often measured relative to the CMB[‡‡] (i.e. the *differential brightness temperature* (DBT) δT_b) and it strongly depends on the spin temperature of the neutral hydrogen (T_S) and on x_{HI} so it can be used to trace the thermal and ionization history of the IGM during the Universe at $z \gtrsim 6$. The DBT can be estimated as Furlanetto 2006:

$$\delta T_b \simeq 27 x_{HI}(1+\delta)\left(\frac{H}{dv/dr + H}\right)\left(1 - \frac{T_S}{T_{\rm CMB}}\right)\left(\frac{1+z}{10}\frac{0.15}{\Omega_m h^2}\frac{\Omega_b h^2}{0.023}\right) \text{mK}. \tag{1.16}$$

Neglecting the effect of the peculiar velocity (dv/dr) and the dependence on the cosmological parameters, before the reionization starts x_{HI} is close to unity, hence δT_b is mostly sensitive to relative difference of $T_{\rm CMB}$ and T_S which can be written as:

$$T_S^{-1} = \frac{T_{\rm CMB}^{-1} + x_\alpha T_\alpha^{-1} + x_c T_K^{-1}}{1 + x_\alpha + x_c}. \tag{1.17}$$

T_α is the colour temperature which is roughly equal to T_K while x_α and x_c are the Lyman-α and collisional coupling coefficients, respectively. These coefficients quantify the strength of the processes (resonant scattering of Lyman-α photons, Wouthuysen 1952 and collisions with free electrons) that drive the spin temperature towards the kinetic temperature (when $x_\alpha + x_c >> 1$, $\mathrm{T}_S \sim \mathrm{T}_K$ otherwise $\mathrm{T}_S \sim \mathrm{T}_{\rm CMB}$).

Across cosmic time the 21cm signal exhibits different features. Soon after recombination ($z \gtrsim 200$) the gas is fully thermally coupled to the CMB ($\mathrm{T}_S = \mathrm{T}_K = \mathrm{T}_{\rm CMB}$) hence we expect $\delta T_b = 0$. Later on ($200 \gtrsim z \gtrsim 40$) the IGM cools adiabatically ($\mathrm{T}_K < \mathrm{T}_{\rm CMB}$) and

[‡‡]In principle it could be measured relative to a radio-loud background source through the 21cm forest although the existence of these objects is highly debated, see e.g. Šoltinský et al. (2025).

collisions with free e^- couple the spin temperature to the kinetic temperature causing the 21cm signal to be seen in absorption. As the Universe expands, the IGM becomes less dense decreasing the efficiency of the collisional coupling bringing the spin temperature closer to the CMB hence damping the 21cm DBT. When the first sources light on, the Lyman-α photons start to couple T_S to T_K - which is colder than the CMB - causing the signal to be seen in absorption. Once T_S is fully coupled to T_K the evolution of the 21cm signal is entirely determined by the kinetic temperature of HI. The X-rays in the early Universe eventually heat up the IGM above the CMB causing the signal to be seen in the emission. Concurrently, the reionization is in progress decreasing x_{HI}, weaking the 21cm emission and eventually erasing it completely once the reionization is completed.

The one described above is the evolution of the sky-averaged 21cm signal (or the *global signal*). This quantity is incredibly hard to measure due to the challenges of accurately model the foregrounds which are order of magnitudes larger than the expected signal ($\sim mK$). The only claimed detection by the EDGES (Experiment to Detect the Global EoR Signature) team (Bowman et al. 2018) was refused by independent reanalysis of the signal (e.g. Sims & Pober 2019) and by other experiments like SARAS (Shaped Antenna measurement of the background Radio Spectrum, Singh et al. 2022). Nonetheless a number of current facilities like REACH (Radio Experiment for the Analysis of Cosmic Hydrogen) or future radio experiments on the moon are trying to detect the $z \sim 10-20$ absorption feature predicted from the light of the first sources.

When looking at the 21cm signal, other than its sky-averaged quantity, one can study its fluctuations as a function of scale. This information is encoded in the 21cm Power Spectrum which is the prime target of radio interferometers such as NenuFAR, Murchison Widefield Array (MWA), LOw-Frequency ARray (LOFAR), Giant Metrewave Radio Telescope (GMRT), Precision Array for Probing the Epoch of Reionization (PAPER), Hydrogen Epoch of Reionization Array (HERA) and the upcoming SKA. Even though at the time of writing a detection has not yet been achieved, the upper limits between $z \sim 7-10$ are significantly improving (e.g. HERA Collaboration et al. 2023; Mertens et al. 2025; Nunhokee et al. 2025) offering promising prospects for a future detection.

1.5. Modelling the high-z Universe

The two key protagonists of any cosmological simulations are galaxies and the IGM. Modeling both in a self-consistent way is not an easy task that requires to compromise between *(i)* complexity of the physical processes that are included, *(ii)* resolution and *(iii)* size of the simulated volume.

1.5.1. Galaxy formation

Any simulation of galaxy formation, needs to account for both the dark matter halo growth discussed in Section 1.3.2 and the baryonic physics (Section 1.3.3).

The evolution of dark matter halos can be captured analytically through the Press-Schechter approach (Press & Schechter 1974) or the Extended Press Schechter (EPS) formalism (Lacey & Cole 1993). The latter one provided foundations for Monte Carlo techniques used to generate the hierarchical merger history (i.e. *merger tree*) of dark matter halos at selected mass and redshift. These techniques were originally developed in Cole et al. (2000) and later improved in Parkinson et al. (2008) with the main advantages of being very fast and efficient, not suffering of limitations in resolution and retrieving the same statistical properties (like the halo mass function) of N-body simulations. However, the merger trees obtained with these Monte Carlo techniques do not provide any spatial information of the dark matter halos and tend to have a worse agreement with full N-body simulations at very high-z.

To fully capture the complex structure of the cosmic web, one needs to use a N-body simulation in which the dark matter fluid is discretized in point mass particles which move inside a simulated volume under the action of gravity. Cosmological N-body simulations are collisionless (dark matter particles do not interact through physical collisions or close encounters). These simulations are typically post-processed with a *halo finder* algorithm (e.g. Knebe et al. 2011) that uses the position and velocity of the particles to identify the dark matter halos. Once all the halos are identified in all the snapshots of the simulation, it is possible to reconstruct the merger trees of all the halos. N-body simulations are typically very accurate* however they are computationally very expensive and

*However, halo finder algorithms often fail at high-z to correctly identify structures that are bound

limited either by resolution or volume. Typically the largest N-body have a simulated volumes of ~Gpc^3 and can resolve halos down to $\sim 10^{10} M_\odot$ (e.g. Angulo et al. 2012) while to resolve mini-halos ($\sim 10^5 M_\odot$) only volumes of Mpc^3 (e.g. Visbal et al. 2020) are feasible.

Semi-analytical models

Semi-analytical models (SAMs) are efficient algorithms that include all the main baryonic processes relevant for galaxy formation by solving analytical equations for each astrophysical process considered. Typically, these include gas infall and cooling, star formation, supernova feedback, mergers and Active Galactic Nuclei (AGN) evolution. They often use merger-trees - either obtained via Monte Carlo techniques or from a N-body simulation - and they "paint" galaxies on top of the dark matter halos. In their astrophysical prescriptions, SAMs include free parameters (e.g. star formation efficiency) that are calibrated against observations (like the stellar mass function or the UV luminosity). These algorithms are typically very fast (especially when run on Monte Carlo merger trees) and allow an efficient exploration of the parameter space which can be particularly efficient to discuss the impact of different physical processes. The main drawback of SAMs is that they heavily rely on parametrization and the simplified analytical prescriptions they use not always capture the complexity of the physical processes involved. Examples of well-established SAMs based on Monte Carlo merger trees are the Cosmic Archaeology Tool (CAT, Trinca et al. 2022) and GALFORM (Cole et al. 2000) or based on N-body L-GALAXIES (Henriques et al. 2015), Semi-Analytic Galaxy Evolution (SAGE, Croton et al. 2016) and the Santa Cruz SAM (Gabrielpillai et al. 2022).

Hydrodynamical simulations

Hydrodynamical simulations directly evolve baryons together with dark matter using gravitational N-body techniques and fluid hydrodynamics solvers. Famous examples include Illustris (Genel et al. 2014), EAGLE (Schaye et al. 2014), and TNG (Springel et al. 2017). These simulations are significantly more complex than SAMs and are able to resolve structure formation at high spatial and mass resolution and naturally capture com-

together, see e.g. Chandro-Gómez et al. (2025)

plex interactions like feedback-driven outflows and environmental effects. Despite their accuracy, even hydrodynamical simulations need to implement sub-grid prescriptions to model physical processes (like star formation) that act on scales below the resolution of the simulation. Finally, they are computationally extremely expensive requiring millions of CPU hours on state-of-the-art supercomputers. We refer the interested reader to Somerville & Davé (2015) for a more in depth review of the numerical techniques implemented in hydrodynamical simulations.

1.5.2. Reionization and IGM

The Universe is not just galaxies, and especially when focusing on $z \gtrsim 6$, it is important to model the evolution of the IGM and the EoR. Similarly to the galaxy formation models, in order of increasing complexity there are analytical, semi-numerical and full radiative transfer simulations of cosmic reionization. Here I will only briefly explain each class of simulations, detailed reviews are provided by Morales & Wyithe (2010) and Gnedin & Madau (2022).

Analytical models

Analytical models of reionization were firstly developed by Miralda-Escudé et al. (2000) and Furlanetto et al. (2004) in order to follow the global ionization fraction as a function of redshift using the balance between ionizing photon production and recombinations in the IGM. This is described using the *volume filling fraction* of ionized hydrogen $Q_{\rm HII}$:

$$\frac{dQ_{\rm HII}}{dt} = \frac{\dot{n}_{\rm ion}}{< n_H >} - \frac{Q_{\rm HII}}{t_{\rm rec}} \tag{1.18}$$

where $< n_H >$ is the mean hydrogen density $t_{\rm rec}$ is the recombination time and $\dot{n}_{\rm ion}$ is the ionizing photon production rate. The latter term can be expressed as the product between the total comoving UV luminosity density ($\rho_{\rm UV}$), the ionising photon production efficiency per unit UV luminosity density ($\zeta_{\rm ion}$) and the fraction of ionizing photons that escape the galaxy (i.e. the *escape fraction*, $f_{\rm esc}$):

$$\dot{n}_{\rm ion} = f_{\rm esc}\zeta_{\rm ion}\rho_{\rm UV}. \tag{1.19}$$

While analytical models offer valuable physical insight and are computationally inexpensive they lack spatial information and cannot capture the patchy, inhomogeneous nature of reionization. Nevertheless, they have been greatly informative and were historically the first attempt to model the EoR.

Semi-numerical models

Semi-numerical models are able to generate ionization maps using fast approximations starting from dark matter density fields (either generated analytically or from N-body simulations). The most famous code is 21cmFAST (Mesinger et al. 2011; Murray et al. 2020) which implements the excursion-set formalism from Furlanetto et al. (2004) to follow the growth of the ionizing bubbles together with a correction to deal with the overlap of bubbles[†]. This model is able to produce also other IGM fields including X-rays, Lyman-α and 21cm brightness temperature. Other similar examples are SimFast21 (Santos et al. 2010) and IslandFAST (Xu et al. 2017).

Algorithms based on the excursion-set formalism do not explicitly conserve photons. For this reason, more refined techniques that solve radiative transfer equation by ray-tracing have been developed. To keep the calculation computationally efficient this can be done only along a small number of directions. Examples of this approach are the Asymmetric Radiative Transfer In Shells Technique" (ARTIST, Molaro et al. 2019) and the "Semi-numerical Code for ReionIzation with PhoTon Conservation (SCRIPT, Maity & Choudhury 2022). For completeness we list also the "Abundance Matching Box for the Epoch of Reionization" (AMBER, Trac et al. 2022) which is based on an entirely different approach called *abudance matching* that assumes a relation between the reionization field and some other base field.

Radiative transfer

The radiative transfer (RT) approach to model reionization involves numerically solving the propagation of ionizing photons through the inhomogeneous IGM, accounting for absorption, emission, and scattering processes. Although highly accurate in following

[†]Recently, in Behling et al. (2025) it was found that semi-numerical models struggle to properly evaluate the impact of reionization on mini-halos, as they often hide in filaments which are not properly captured by 21cmFAST like approaches

the spatial and temporal evolution of reionization, RT simulations are computationally intensive and require significant resources to achieve adequate resolution and dynamic range.

These models can be coupled with dark matter only N-body simulations and in this case they are referred to as *partially coupled* (since the baryonic physics is missing not all the physical processes are coupled). Examples of these are C^2-Ray (Iliev et al. 2006), GRIZZLY, (Ghara et al. 2018), CRASH (Eide et al. 2018, 2020). Finally, when RT methods are *fully coupled* to hydrodynamical simulations, the growth and overlap of ionized regions around early galaxies and quasars is accurately tracked. This approach captures the complex interplay between radiation and structure formation, including shadowing effects, photon mean free paths, and anisotropic ionization fronts. These are undoubtably the most expensive simulations reaching volumes up to ~ 100 cMpc. The current state-of-the-art simulations are CosmicDawn (CoDa, Ocvirk et al. 2020), Cosmic Reionization On Computers (CROC, Gnedin 2014) THESAN (Kannan et al. 2022) and SPHINX (Rosdahl et al. 2018).

1.5.3. Meraxes

In this thesis the SAM MERAXES has a pivotal role as the author contributed to its development and all the research presented is obtained through post-processing of its outputs. In MERAXES, the merger trees are built from a N-body simulation so that the spatial information of the galaxies is provided. This model was the first of its kind to couple the galaxy formation model to a semi-numerical model of reionization enabling self-consistent predictions of both galaxy evolution and the ionization state of the IGM. MERAXES was first introduced by Mutch et al. (2016) and since then, it underwent several updates by Qin et al. 2017 (AGN feedback), Qiu et al. 2019 (dust models) Marshall et al. 2019 (galaxy morphologies and bulges) and Balu et al. 2023a (X-rays and 21cm evolution). MERAXES takes a number of free parameters (e.g. star formation efficiency) that needs to be tuned to match the available observational data. These are calibrated towards the UV luminosity functions up to $z \sim 12$, the stellar mass functions up to $z \sim 8$ and the reionization history including constrains on $x_{\rm HI}$ at $z \sim 5-10$ and the Thomson scatter optical depth from Planck Collaboration et al. (2020). Below are summarised the

main astrophysical prescriptions included in MERAXES. These will not include the latest update by Ventura et al. (2024) which is extensively discussed in Section 3.2.

From the N-body simulation, MERAXES inherits two structures: the halos (or Friend-of-Friend groups) defined as groups of gravitationally bound particles. These are further divided in sub-halos: the mass dominant one is referred to as *central* along with zero or more subdominant *satellites*. Each sub-halo hosts a galaxy, which in MERAXES is modeled with three primary gas reservoirs: hot gas $m_{\rm hot}$, cold gas $m_{\rm cold}$ and ejected gas $m_{\rm ejected}$. The hot gas — which represents the CGM — resides in the halo and is shock-heated to the virial temperature of the sub-halo. The cold gas, found in the disk, constitutes the ISM and serves as the fuel for star formation. The ejected gas is no longer gravitationally bound to the galaxy and effectively becomes part of the IGM. Each galaxy, after being identified from the merger tree, evolves according to the following processes:

Gas Infall

At each snapshot of the simulation, each dark matter halo (FoF) accretes pristine gas according to:

$$m_{\rm infall} = f_{\rm mod} f_b M_{\rm vir} - \sum_{i=0}^{N_{\rm gal}-1} m^i_{\rm star} + m^i_{\rm cold} + m^i_{\rm hot} + m^i_{\rm ejected} \tag{1.20}$$

where $f_b = \Omega_b/\Omega_m$ is the universal baryon fraction set by cosmology and the summation for all the gas and stellar ($m_{\rm star}$) reservoirs is over every galaxy in the FoF halo. $0 \leq f_{\rm mod} \leq 1$ is the *baryon fraction modifier* and it parametrizes the attenuation of the total baryon mass captured by an FoF group. This suppression is due to local UV background and photo-ionizing feedback from reionization (see e.g. Dijkstra et al. 2004). Note that Eq. 1.20 can be negative (e.g. when $f_{\rm mod}$ decreases) causing the baryons to be stripped from the hot reservoir and assigned to the ejected one. All the accreted mass is then added to $m_{\rm hot}$ of the central galaxy.

Gas Cooling

Some fraction of the hot gas can then cool down and settle into the central region of the galaxy. To estimate the amount of gas that cools down in a snapshot it is adopted the

methodology described in White & Frenk (1991). Firstly, it is computed the cooling rate per unit volume:

$$t_{\rm cool}(r) = \frac{1.5\bar{\mu} m_{\rm p} k T_{\rm vir}}{\Lambda(T_{\rm vir}, Z)\rho_{\rm hot}(r)} \tag{1.21}$$

where $m_{\rm p}$ is the proton mass, k the Boltzmann constant and $\rho_{\rm hot}(r)$ the hot gas density profile (a single isothermal sphere is assumed). $\Lambda(T_{\rm vir}, Z)$ is the temperature ($T_{\rm vir}$) and metallicity (Z) dependent cooling function from Sutherland & Dopita (1993)[‡]. $t_{\rm cool}$ is then compared to the dynamical time of the halo $t_{\rm dyn}^{\rm FoF}$ to find the cooling radius $r_{\rm cool}$ such that $t_{\rm cool}(r_{\rm cool}) = t_{\rm dyn}^{\rm FoF}$. All the hot gas within $r_{\rm cool}$ is moved to the cold gas reservoir over a dynamical (free-fall) time.

Star formation

All the cold gas is assumed to settle into a rotationally supported disk with an exponential surface density profile. The disk radius $r_{\rm disk}$ is estimated from the spin parameter of the halo λ and the virial radius $R_{\rm vir}$ following Bullock et al. 2001.[§] In order for the gas to form stars, this has to have a surface density large enough to undergo fragmentation and form stars ($\Sigma_{\rm cold} \geq \Sigma_{\rm SF}$, see Kauffmann 1996; Kennicutt 1998). This density criterion can be converted into a critical mass $m_{\rm crit}$ needed to form stars:

$$m_{\rm crit} = \Sigma_{\rm SF}\left(\frac{V_{\rm max}}{100\ {\rm km\ s^{-1}}}\right)\left(\frac{r_{\rm disk}}{10\ {\rm kpc}}\right) \times 10^{10} {\rm M}_{\odot}. \tag{1.22}$$

with $V_{\rm max}$ the maximum circular velocity of the halo. When $m_{\rm cold} > m_{\rm crit}$ stars are formed following the star formation efficiency $\alpha_{\rm SF}$ and the star formation rate (SFR) is given by:

$$\dot{m}_{\rm SF} = \alpha_{\rm SF} \times \frac{m_{\rm cold} - m_{\rm crit}}{t_{\rm disk}^{\rm dyn}}. \tag{1.23}$$

where $t_{\rm disk}^{\rm dyn}$ is the dynamical time of the disk. The distribution of the initial stellar is assumed to follow the Kroupa (Kroupa 2001) initial mass function (IMF).

[‡]These do not include H_2 cooling rates so in the original version of MERAXES mini-halos cannot cool down the gas.

[§]In Marshall et al. (2019) a more precise calculation of the disk radius was developed assuming the conservation of angular momentum throughout all processes that add/remove gas from the disk. See more in Chapter 4.

Supernova feedback

The main effect of supernova feedback is to inject energy and release metals into the cold gas. When the energy injection is large enough, the gas can be mechanically heated and moved from the cold reservoir to the hot one ($\Delta m_{\rm reheat}$). In some extreme cases the energy injection is so efficient that the gas can be ejected outside the halo and moved from the hot to the ejected reservoir ($\Delta m_{\rm eject}$).

Firstly, it is assumed that the energy is released by Type II supernovae occurring for stars with $M \geq 8M_{\odot}$. The fraction of stars in a galaxy going supernovae is found by integrating the IMF from $8M_{\odot}$ to $120M_{\odot}$ (the upper limit of the IMF). Given that the cadence of the snapshots in MERAXES is shorter than the typical lifetime of a $8M_{\odot}$ star (~ 40 Myr), it is implemented a delayed supernova scheme that allows stars to go off in a future snapshot compared to when they are formed. With these information the energy injected into the ISM is computed as:

$$\Delta E_{\rm SN} = \varepsilon \times \int_{t}^{t+\Delta t} dt' \int_{0}^{\infty} d\tau \frac{d\epsilon}{d\tau} \dot{m}_{\rm SF}(t' - \tau) \tag{1.24}$$

where Δt is the timestep of the simulation, ε the energy coupling efficiency, and $d\epsilon/d\tau$ the rate of energy released by stars of age between τ and $\tau + d\tau$ as Type II supernovae. The latter is computed using the stellar population code STARBURST99 (Leitherer et al. 1999). $\Delta E_{\rm SN}$ is used to compute $\Delta m_{\rm reheat}$ and $\Delta m_{\rm eject}$ assuming a mass loading factor (η) which describes a mass-energy coupling efficiency.

The metal enrichment is treated in an analogous fashion. To find the amount of metals $\Delta m_{\rm Z}$ injected in the ISM, Eq. 1.24 is used without ε and in which $d\epsilon/dt$ is replaced with the mass of metals released by stars of age between τ and $\tau + d\tau$ ($dm_{\rm Z}/d\tau$) computed with STARBURST99. The metals released into the cold gas are assumed to mix homogeneously with the gas.

UV luminosities and dust models

MERAXES also implements a dust model that follows Charlot & Fall (2000) and allows to compute the dust transmission function $T_{\lambda}(t)$. Photons emitted by young stars are absorbed by both the ISM in the galaxy and by the surrounding molecular cloud where

these stars formed. This molecular cloud is assumed to have a lifetime of 10 Myr so that the starlight coming from stars older than this lifetime is absorbed only by the ISM dust.

With this dust model, the UV luminosity for galaxies in MERAXES is computed as:

$$L_{\rm UV} = \int_{1550}^{1650} d\lambda \int_0^t dt \int_{Z_{\rm min}}^{Z_{\rm max}} dZ \dot{m}_{\rm SF}(t-\tau, Z) S_\lambda(\tau, Z) T_\lambda(\tau) \tag{1.25}$$

where $S_\lambda(\tau, Z)$is the luminosity of a stellar population of age τ and metallicity Z calculated from STARBURST99. Note that a top-hat filter centered at $\lambda = 1600$ Å has been applied.

Mergers

As in all SAMs, galaxy mergers are triggered by the merging of their host dark matter halos. When a dark matter halo is marked as merged, the time taken for the orbit of the infalling galaxy to decay and the corresponding time for the galaxy–galaxy merger to occur is computed utilizing dynamical friction arguments (see Mutch et al. 2016 for more details).

When a merger occurs, all the gas and stellar reservoirs are simply added. However, especially when the mass ratio between the infalling galaxy and the parent gets closer to 1 (i.e. *major merger*), galaxy mergers can drive strong shocks and turbulence in the ISM triggering an efficient burst of star formation. The fraction of cold gas converted in stars by such a burst is modeled as:

$$\frac{m_{\rm burst}}{m_{\rm cold}} = \alpha_{\rm burst} \left(\frac{m_{\rm gal}}{m_{\rm parent}} \right)^{\gamma_{\rm burst}} \tag{1.26}$$

with $\alpha_{\rm burst}$ and $\gamma_{\rm burst}$ free parameters of the model.

Reionization

The reionization is computed via a semi-numerical approach based on the excursion-set formalism similarly to 21CMFAST. The uniqueness of MERAXES is the fully coupling between the galaxy population and the reionization through the baryon fraction modifier $f_{\rm mod}$ (computed ala Sobacchi & Mesinger 2013) which is used to determine the amount

of the infalling gas. For each snapshot, after all the galaxies have been evolved via the processes highlighted above, star formation rate and stellar mass grids are generated using the spatial information of the galaxies. These grids are used to compute UV ionizing background ($\bar{J}_{21}$) and $x_{\rm HI}$ fields. $f_{\rm mod}$ is finally computed as a function of $\bar{J}_{21}$ and then applied in the next snapshot to all galaxies to compute their baryonic infall.

Other radiative backgrounds and 21cm signal

The same approach outlined above is also applied to compute all the radiative backgrounds relevant for the calculation of the 21cm brightness temperature. In particular, X-ray and Lyman-α are linked to the star formation rate grids and are used to compute the spin and kinetic temperature in each pixel. The main difference with the UV ionizing background is given by the different mean free path (e.g. for X-rays is significantly larger than the UV). Using the density, ionization and temperature grids the differential brightness temperature (δT_b) field is computed allowing the estimation of the 21cm global signal and power spectrum (see Balu et al. 2023a).

1.6. The high-z Universe through the eyes of JWST

JWST has revolutionized our understanding of the high-z Universe by pushing the observational frontier to earlier cosmic times with unprecedented sensitivity and resolution. Its spectroscopic capabilities have also enabled detailed studies of the chemical composition and ionization state of early galaxies, offering new insights into the timeline and drivers of cosmic reionization and metal enrichment. Within its first years of operation, JWST has identified a surprisingly large population of bright, massive galaxies at redshifts $z > 10$ (e.g. Harikane et al., 2023; Pérez-González et al., 2023; Donnan et al., 2023; Castellano et al., 2024) including the most distant spectroscopically confirmed source at $z \sim 14.5$ (Naidu et al. 2025). Additionally, results from Carnall et al. (2023) and Labbé et al. (2023) revealed a population of massive ($\gtrsim 10^{10} M_{\odot}$) and quiescent (red) galaxies at $z \gtrsim 4$. Both these observations challenge the existing models of galaxy formation and suggest that star formation and galaxy assembly began earlier and proceeded more rapidly than what previously thought. It is too early to claim that ΛCDM is broken (see

e.g. Yung et al. 2025) given the huge uncertainties in the physics driving early galaxy formation. To explain this overabudance of UV-bright galaxies at $z > 10$ a number of explanation have been suggested including:

- *high star formation efficiency* in high-z galaxies either due to weaker feedback (see e.g. Dekel et al., 2023) or due to a density dependence (Somerville et al. 2025).
- *burstiness* in star formation histories (e.g. Sun et al., 2023; Gelli et al., 2024) which might cause galaxies that recent underwent a starburst to outshine. This has been shown to alleviate a tension up to $z \sim 12$ but struggles to explain the most luminous candidates at $z \sim 14$.
- *a hidden population of AGN* contributing to the luminosity of the galaxy (e.g. Hegde et al., 2024). This might help explaining some of the compact bright sources but not the extended ones.
- *A decreased dust-attenuation* in high-z galaxies (e.g. Ferrara et al., 2023). This scenario might be associated with the burstiness in star formation as a starburst may be associated with efficient clearing of dust due to radiation pressure.
- *A more top-heavy IMF* (e.g. Trinca et al., 2023) implying a higher light to mass ratio. In this case the mass estimated from the UV bright galaxies would significantly decrease. A more top-heavy IMF is indeed expected at high-z due to very low metallicity of gas however a more top-heavy IMF would also lead to a large number of stars going supernova, making the feedback stronger and potentially quenching the star formation. This scenario is particularly intriguing because a more top-heavy IMF might be the first hint towards a Pop. III stellar population. This scenario will be widely discussed in this thesis in Section 3.4.

CHAPTER 2

Population III stars

Io non voglio andare in cerca di me stesso
Perchè rischio di trovarmi per davvero
Eyes Wide Shut
Vanno in scena le mie maschere

Caparezza - Eyes Wide Shut (2021)

The two main properties to classify stars are mass and *metallicity* (Z). The latter quantity is defined as the ratio between the mass of *metals* - elements heavier than Hydrogen and Helium* - and the total mass of the system (a star, a galaxy etc.) considered. A commonly used unit is the *solar metallicity* $Z_\odot \simeq 0.02$ (Asplund et al. 2009 i.e. the $\sim 2\%$ of the mass of the Sun is in form of elements heavier than He). According to their metallicity, stars are classified as *Pop. I* - young and high metallicity with $Z \gtrsim Z_\odot$ -, *Pop. II* - with a lower content of metals ($Z \lesssim 0.5\ Z_\odot$) - and *Pop. III* - with a truly pristine ($Z \sim 0$) chemical composition† -. The star with the lowest metallicity reported as of

*The reason for this classification, other than the laziness of astronomers, is that H and He were mainly produced during the Big Bang nucleosynthesis, while all the other heavier elements are produced in various stages of stellar evolution; see Kobayashi et al. (2020) for a complete review on the origin of the elements.

†In practice, Pop. III stars are often defined not as strictly pristine but as forming below a critical metallicity threshold, Z_{crit}, below which cooling is inefficient; see more in section 2.1.

today is SDSS J102915+172927 with $Z_\star \simeq 6.6 \times 10^{-5} Z_\odot$ (Caffau et al. 2011; Lagae et al. 2023). Despite several observations of extremely metal poor stars, no *zero-metallicity* star have yet been found. This absence points to a fundamental gap in our observational understanding of the earliest stages of star formation.

After having provided a broad overview of the assembly and early evolution of cosmic structures, in this chapter I will zoom-in into the very first episodes of star formation arising from the metal-free clouds in pristine dark matter halos. I will first review the standard Pop. III formation scenario in Section 2.1 and then discuss in 2.2 the state-of-the-art numerical simulations that include Pop. III star formation. I will conclude this chapter in Section 2.3 with a broad summary of the main observational probes that are currently being used to directly or indirectly detect Pop. III stars at both high and low redshift. For a more in-depth discussion of the topics reviewed here, we refer the interested reader to Bromm (2013) and Klessen & Glover (2023).

2.1. Standard Pop. III formation scenario

To describe the formation of the first Pop. III stars from the initial collapse phase to the disk fragmentation that ultimately determines the masses of the first stars, the starting point is to determine *what is the smallest dark matter halo that can host Pop. III star formation.* This can be derived analytically requiring that a halo needs to be massive enough to accrete gas and to efficiently cool the gas. The first condition is linked to the definition of the *Filtering mass* described below.

Filtering mass

From the argument of the growth of density perturbations considering a dark matter halo already virialized and baryons accreting onto it, Barkana & Loeb (2001) found that the minimum halo mass to develop a substantial baryonic overdensity ($\delta_b \gtrsim 100$) is:

$$M_{\rm crit} \simeq 5 \times 10^3 \left(\frac{\Omega_m h^2}{0.143}\right)^{-0.5} \left(\frac{\Omega_b h^2}{0.022}\right)^{-0.6} \left(\frac{1+z}{10}\right)^{1.5} {\rm M}_\odot. \tag{2.1}$$

implying a minimum mass of $\sim 10^4$ $M_\odot$ at $z \sim 30$. This equation is only an approximation of the correct result (see definition of Filtering mass in Gnedin & Hui 1998 and Naoz & Barkana 2007) as it assumes that the Universe is static while the baryonic perturbations grow. In particular Eq. 2.1 does not include neither the expansion of the Universe nor physical processes able to strip the gas from the dark matter halo such as the X-ray and photo-ionizing background (e.g. Park et al. 2021) and the baryon-dark matter streaming velocities (e.g. Tseliakhovich & Hirata 2010).

This latter effect arise from the different behaviors of baryons (coupled to photons until the recombination) and dark matter (evolving independently). When baryons decoupled from the photons at recombination they had a relative velocity to dark matter of ~ 30 km s^{-1}‡ which is referred to as *stream velocity*. After recombination, baryons started to fall into the potential wells of dark matter halos, however, they retained memory of this relative velocity damping the accretion of baryons onto the dark matter overdensites. As the Universe expands, the streaming velocity gradually decays so that their effect is expected to be significant only up to $z \sim 20$. Naoz et al. (2013) incorporated this effect in the definition of the filtering mass finding that, the inclusion of streaming velocities, ($v_{\rm bc}$) leads to an increase of the minimum halo mass of one order of magnitude when $v_{\rm bc} = \sigma_{\rm vbc}$. This result has been further verified in numerical simulations (e.g. Kulkarni et al., 2021; Schauer et al., 2021). Finally, the minimum halo mass required to retain gas also depends on the underlying cosmological model. Alternative dark matter scenarios - such as warm dark matter (Maio & Viel 2015) or fuzzy (Mocz et al. 2020) - tend to suppress small-scale structure formation, thereby delaying the collapse of the first halos and effectively raising the threshold mass needed to host a gaseous halo.

Primordial cooling processes

The second crucial requirement for a pristine halo to form Pop. III stars, is its ability to cool the gas effectively. In a metal-free halo, the only possible coolant must be in some form of H. As we saw in 1.5.1, in halos with $T_{\rm vir} \gtrsim 10^4$ K, the atomic hydrogen is an efficient coolant via Lyman series de-excitations lines (i.e. Lyman-α cooling). At lower

‡This is the root-mean-square value of the Maxwellian distribution at recombination ($\sigma_{\rm vbc}$), values in different regions of the Universe are usually expressed as multiples of $\sigma_{\rm vbc}$.

temperatures, cooling can happening only through H_2. Such a molecule is highly symmetric and lacks of dipole momentum; the only transitions through which can radiate energy are via forbidden magnetic quadrupole lines. This makes molecular hydrogen a quite inefficient coolant able to bring the temperature of the gas only down to ~ 200 K (Greif 2015). The temperature can drop further only in presence of deuterium through the HD molecule. HD has a non-zero dipole momentum and can make the gas temperature to drop down to ~ 128 K (this is sometimes referred to as Pop. III.2 formation scenario as it implies that the halo is either more massive or externally irradiated, enhancing the fractional ionization in the halo and leading to the formation of HD).

To form H_2 there are three main channels (for a full review see Bovino & Galli 2019):

- A two-stage reaction using e^- (either from recombination or from collisional ionization in the gas) as a catalyst. $H + e^- \rightarrow H^- + \gamma$ followed by $H^- + H \rightarrow H_2 + e^-$. This reaction involves the formation of H^- as an intermediate product.
- A two-stage reaction using free protons (H^+) as a catalyst and involving H_2^+ molecule as an intermediate product: $H + H^+ \rightarrow H_2^+ + \gamma$ followed by $H_2^+ + H \rightarrow H_2 + H^+$.
- A three body reaction $H + H + H \rightarrow H_2 + H$ followed by $H + H + H_2 \rightarrow H_2 + H_2$.

The first two channels are dominant in low density systems and require a partially ionized medium. These formation pathways are not very efficient and the molecular hydrogen fraction (f_{H_2}) obtained via these routes is typically $\sim 10^{-3}$. The second channel is dominant at very high-z ($z \gtrsim 100$) since CMB photons are energetic enough to destroy H^- ions. The last channel is very effective in high density medium and for $n \sim 10^{11}$ cm^{-3} the gas becomes fully molecular. By requiring that a halo needs to have enough molecular hydrogen in order to cool down the gas, Tegmark et al. (1997)[§] found a typical value of the critical mass for a halo to host Pop. III stars $\sim 10^6$ $M_\odot$ at $z \sim 20 - 30$ (roughly equivalent to a $T_{vir} \simeq 10^3$ K). These halos have typically $f_{H_2} \sim 10^{-4}$.

Molecular hydrogen is a relatively fragile molecule and it can be dissociated by UV photons with energy between 11.2 and 13.6 eV (i.e. the *Lyman-Werner (LW)* band, see Stecher & Williams 1967). As soon as the first stars form, they emit photons in the LW

[§]This calculation was later on updated in order to account for more precise reaction rates, see e.g. Nebrin et al. (2023).

band. These photons can propagate to large distances through the IGM (their mean free path can be up to ~ 100 Mpc, Dijkstra et al. 2008). Once a halo is irradiated by a LW background, the fraction of H_2 will decrease. As a net effect, the threshold halo mass to host Pop. III star formation will increase in presence of LW background (e.g. Haiman et al., 2000). This effect can be counteracted in high density halos where the H_2 is self-shielded. The typical strength (J_{21}) of a LW background required to effectively dissociate H_2 is (Oh & Haiman 2002):

$$\left(\frac{J_{21}}{n}\right) \simeq 10^{-4} f_{sh} \tag{2.2}$$

expressed in units of 10^{-21} erg $s^1 cm^{-2} Hz^{-1} sr^{-1}$ and n is the density of the gas at the halo center. f_{sh} is the *self-shielding factor* which is usually estiamted from numerical simulations (e.g. Kulkarni et al., 2021). The above equation yields to values of $J_{21} \sim 10^{-3}$ in absence of self-shielding.

Finally, the presence of a X-ray background can boost the H_2 formation due to the photo-ionization of the IGM which leads to an increase in the density of free electrons used in the production of H_2 (Haiman et al. 2000). All these physical processes (LW photo-dissociation, self-shielding and X-rays) impact the minimum mass of a mini-halo able to host stars. Analytical expressions that take into account all these effect simultaneously are difficult to find, typically fitting formulas are used based on results from numerical simulations where all these astrophysical processes are included (see e.g. Visbal et al. 2015 or Kulkarni et al. 2021).

Initial collapse of the gas

After assessing the minimum mass for a mini-halo to form Pop. III stars and how this is influenced by different astrophysical mechanisms, I dive into the process of Pop. III star formation starting from the initial collapse of the gas in a pristine mini-halo. Fig. 2.1 shows the evolution of the gas temperature and molecular hydrogen fraction as a function of density. Labels from A to G mark key phases of the collapse.

At the beginning (A), the gas is in the hot phase shockly heated to the virial temperature of the halo. At this point $f_{H_2} \sim 10^{-4}$ which is high enough to start cooling the gas (B) down to ~ 200 K (C). At this point the gravity of the gas overcomes the dark

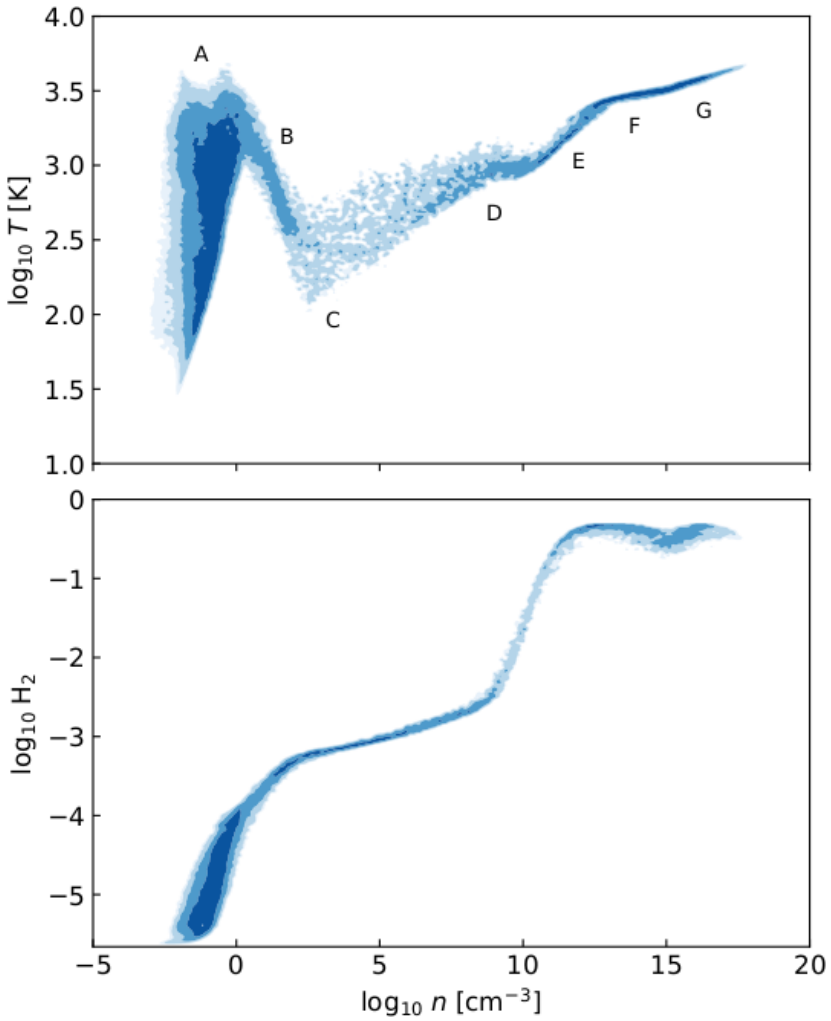

Figure 2.1: The relation between temperature T and hydrogen number density n during the initial collapse phase (**top**) and the corresponding fraction of molecular hydrogen (**bottom**). Figure is taken from Klessen & Glover (2023) showing data from Schauer et al. (2021).

matter one and the contraction proceeds causing the temperature to rise up to ~ 1000 K (D). The density of the gas is now high enough to favour the formation of H_2 through three-body reactions and the hydrogen becomes fully molecular (E). As the density and temperature keep increasing, H_2 starts to decrease (F) due to collisional dissociation. In the final phases of the collapse, the gas is now approaching proto-stellar conditions (G) reaching $n \sim 10^{16}\mathrm{cm}^{-3}$ with the H_2 further depleting and the collapse becomes adiabatic at $n \sim 10^{20}\mathrm{cm}^{-3}$.

Disk formation and fragmentation

The final product of the initial collapse is a hydrostatic proto-stellar core (mass of $\sim 10^{-3}\mathrm{M}_\odot$ surrounded by a disk-like structure. The first simulations able to follow the initial collapse (e.g. Omukai & Nishi, 1998; Bromm et al., 1999; Abel et al., 2000; Yoshida et al., 2003), found a central object with very little angular momentum and mostly supported by pressure. This result supported the idea that the final product of the collapse was a single very massive star. However, these simulations stopped when the final density of the object was $\sim 10^{16}$ cm^{-3} due to computational cost limits. In the last decade, through more advanced numerical simulations extending beyond the proto-stellar collapse, this picture was revised. A number of works (e.g. Greif et al., 2011a; Hirano et al., 2014; Stacy et al., 2016; Sugimura et al., 2020; Prole et al., 2022) showed that these primordial accretion disks are prone to fragmentation suggesting the formation of Pop. III stellar cluster rather than a single high-mass star. This high fragmentation is mostly due to the high mass load onto the disk from the infalling envelope which exceeds the gas capability to transport material inwards. Ultimately, this causes a build up of massive spiral arms speeding the inward transport.

A number of processes can further complicate this picture either enhancing or suppressing fragmentation. In presence of a strong LW background a mini-halo cannot cool the gas via H_2 and needs to exceeds the atomic cooling threshold ($T_{vir} \sim 10^4$ K) before cooling the gas. In such a scenario, once the cooling begins via atomic hydrogen, the mass of gas is very large and so are the associated infall velocities making the inflow motion turbulent. Turbulency is one of the main driver of fragmentation so the ultimate result of a pristine halo beyond the atomic cooling threshold cooling down the gas is an

increase in fragmentation (Greif et al. 2008; Wise & Abel 2008). A similar result can also be obtained by the streaming velocity between dark matter and baryons which delays the gas assembly and increases the halo mass before it is able to cool down the gas.

On the opposite side, magnetic fields can reduce disk fragmentation by removing angular momentum from the star forming gas. Recent studies showed that at very high-z, the magnetic energy density can be between 1 - 10% of the kinetic energy density with a field topology highly tangled (Seta & Federrath 2021). Such magnetic fields can affect the evolution of protostellar accretion disks leading to more massive fragments ultimately preventing the formation of low-mass stars ($M \gtrsim 1 M_{\odot}$, Sharda et al. 2021). However, the details of how magnetic fields influence the early star formation are still subject of research.

On the Pop. III IMF

What is the initial mass distribution of Pop. III stars is arguably one of the most crucial questions as it determines their fundamental properties and potential observability. Unfortunately, as of today, it is impossible to simulate the star formation process throughout the entire duration of the disk evolution and the simulations usually stop when the fragment form. The final fate of these fragments is still highly debated with various studies indicating that roughly two thirds of the fragments quickly disappear, leaving only the remaining one third to survive (e.g. Stacy & Bromm, 2013; Latif et al., 2022). The final fate of a surviving fragment is then set by the mechanism terminating its accretion which could be:

1. The system runs out of mass (all the mass accretes on the proto-star) leaving a relatively massive star.

2. Stellar feedback removes the accreting material. In this case a wide range of scenario opens up and different simulations provide different outcomes.

3. The fragment is ejected of the disk when this is still relatively low-mass. This would lead to the formation of a low-mass object potentially still detectable in stellar archaeology surveys targeting halos of present day galaxies.

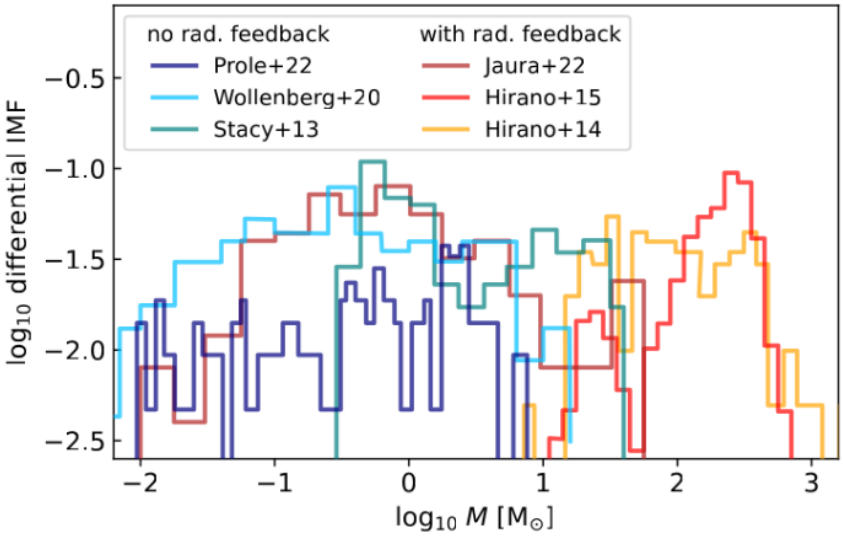

Figure 2.2: Predicted Pop. III IMFs from three high-resolution models with no feedback (Stacy & Bromm 2013; Wollenberg et al. 2020; Prole et al. 2022), and from three simulations including radiative feedback (Hirano et al. 2014, 2015; Jaura et al. 2022). Adopted from Klessen & Glover (2023).

As of today, the available simulations provide wildly inconclusive answers (see Fig. 2.2) with the astrophysical processes and the numerical details included in the simulations severely impacting the results. On average, models that include stellar (and radiative) feedback predict larger stellar masses. Nevertheless, despite the large variation in mass range, all the predicted IMFs are approximately flat in the log space. Hence, the commonly adopted assumption that the Pop. III IMF is more *top-heavy* (i.e. larger power at the high-mass end) compared to the present-day, *bottom-heavy* IMF (e.g. Kroupa 2001).

Transitioning from Pop. III to Pop. II stars

Once they form, Pop. III stars play a pivotal role in the cosmic metal enrichment that drives the transition to later generations of stars. Through their short but energetic lives, Pop. III stars inject the first metals into the ISM and IGM via stellar winds and SNe explosions. The two main types of SN explosions are core-collapse SN (CCSN)[¶] and pair instability SN (PISN, see e.g. Heger & Woosley 2002). [‖] This chemical enrichment

[¶]CCSN represents the end of the life for stars with initial mass $8M_\odot \lesssim M \lesssim 40\ M_\odot$. After the formation of a Fe core, the star undergoes a sudden collapse triggering a SN explosion and leaving behind a neutron star or a black hole.

[‖]Stars with $M \sim 140 - 260 M_\odot$ (although see Yoon et al. 2012; Woosley 2017; Farmer et al. 2019 for further discussion on these mass limits) at the end of their life, reach high enough temperatures in their He cores to convert photons into $e^- e^+$ pairs through the interaction with surrounding nuclei. This causes

raises the metallicity of their surroundings above a critical threshold ($Z_{\rm crit}$), enabling more efficient cooling and fragmentation of gas, which marks the shift from Pop. III to Pop. II star formation. As a result, Pop. III stars not only shape their local environments but also set the stage for the end of primordial star formation and the onset of more chemically enriched stellar populations across the Universe.

The value of the critical metallicity that defines the transition between Pop. III and Pop. II is tied to how the thermodynamics of collapsing gas clouds change in presence of metals and dust. There are two main theoretical pathways used to estimate the critical metallicity: *(i)* metal line cooling and *(ii)* dust cooling. The former takes α elements such C and O as main coolants and sets the value of $Z_{\rm crit} \sim 10^{-3.5} Z_{\odot}$ (e.g. Chon et al., 2021) while in the second mechanism, dust grains formed in SN ejecta exchange thermal energy with gas and radiate it away, allowing the gas to cool. In such a case, the critical metallicity can be significantly lower ($Z_{\rm crit} \sim 10^{-6} Z_{\odot}$, Schneider et al. 2006, 2012)

The impact of the first Pop. III stars does not restrict to the local and cosmic metal enrichment and they profoundly change the evolution of the Universe across both small and large scales. On small scales, their intense radiation, stellar winds, and supernovae rapidly heat and ionize the surrounding gas, suppressing further star formation in their host halos. On larger scales, Pop. III stars contribute to the early stages of cosmic reionization, alter the thermal and ionization state of the intergalactic medium, and shape the conditions for subsequent galaxy formation. Additionally, they build up the LW background delaying or suppressing star formation in other mini-halos. In conclusion, the feedback of the first Pop. III stars acts as a critical bridge between the pristine early Universe and the emergence of the first galaxies.

2.2. Pop. III stars in numerical simulations

Given the complete absence of observations of Pop. III stars, our current knowledge of these objects is purely based on numerical simulations. These usually investigate their properties (e.g. initial masses), the environment where they form or their cosmological implications (e.g. the Pop. III / Pop. II transition). To study in detail the astrophysical

a sudden collapse due to loss in radiation pressure support and triggers a dynamical implosion of the core. The typical energy of a PISN is 1 or 2 order of magnitude higher than CCSN.

processes regulating Pop. III star formation, hydrodynamical simulations are needed, while SAMs are more suited to investigate their environments or for more statistical studies. Once again, the biggest challenge of including Pop. III stars in numerical simulations is the trade off between the mass and scale resolution against the volume.

To follow the entire process of Pop. III star formation from the initial collapse to the disk fragmentation, *zoom-in* hydrodynamical simulations are required. These typically begin by running a lower-resolution cosmological simulation ($L \sim 1-10$ cMpc) to identify suitable halos (e.g., pristine, metal-free minihalos), and then "zoom in" with much higher resolution to simulate baryonic physics in that environment. With this technique, spatial scales of ~AU and mass scales of $\sim M_\odot$ can be resolved ultimately aiming to determine a priori the Pop. III IMF. These model often cannot include the effects of chemical and mechanical SNe feedback although sometimes they include radiative feedback and magnetic fields. To list a few based on Smoothed Particle Hydrodynamic (SPH) codes such as GADGET: Stacy & Bromm 2013; Hirano et al. 2014, 2015; Stacy et al. 2016; Hirano et al. 2018; Chon et al. 2021 or based on Adaptive Mesh Refinement (AMR) techniques:, Greif et al. 2011b; Wollenberg et al. 2020; Jaura et al. 2022; Prole et al. 2022; Chiaki & Yoshida 2022 (using AREPO), Sharda et al. (2021) (using FLASH), Sugimura et al. (2020) (using SFUMATO) and Latif et al. (2022) (using ENZO).

Zoom-in simulations often stop once the fragments are formed and do not follow the evolution of Pop. III stars. To model quantities such as the star formation rate density (SFRD) as a function of redshift, or the transition between Pop. III and Pop. II stars as well as the build up of the cosmic LW background, cosmological simulations with bigger volumes than the zoom-in are required. These typical attempt to model volumes of $(\sim 1-10 \text{ cMpc})^3$ resolving scales down to tens of parsecs and with baryonic mass resolution of $\sim 10^3$ $M_\odot$ (in these cases a star particle represents a star cluster rather than a single star). Examples of simulations that include Pop. III stars are described in e.g. Pallottini et al. (2014); Smith et al. (2015); Xu et al. (2016, 2017); Sarmento et al. (2018); Jaacks et al. (2018); Skinner & Wise (2020); Sarmento & Scannapieco (2022); Zier et al. (2025). These simulations are highly different from each other as they start from different setups depending on the astrophysical effect that is investigated. For example, simulations that focus on detailed chemical enrichment (e.g. Smith et al. 2015) still require a high mass and

spatial resolution to follow in great detail the various astrophysical processes hence are limited to small volumes. Conversely, when studying cosmological implications, larger volumes with coupled radiation-hydrodynamics simulations are preferred (e.g. Xu et al. 2016) requiring to adopt a simplified treatment of various feedback processes.

Pop. III stars can be also included in SAMs. In this case, their free parameters regulating Pop. III star formation are calibrated on the zoom-in simulations. SAMs are particularly useful to explore the cosmological implications of different Pop. III models (e.g. impact on cosmic reionization and metal enrichment) and to study the environments of Pop. III star formation. In the last decade, a huge plethora of SAMs has been introduced. These include (but are not restricted to) the ones described in Trenti & Stiavelli (2009); Hartwig et al. (2015b, 2018a); Visbal et al. (2018, 2020); Mebane et al. (2018, 2020); Trinca et al. (2022); Hegde & Furlanetto (2023); Feathers et al. (2024). I will not dive into further details here as the chapters 3, 4 and 5 of this thesis extensively discuss and show the strength of SAMs including Pop. III stars.

2.3. Observational prospects of Pop. III stars

Not having achieved a Pop. III detection so far is not a valid reason to stop trying. A number of efforts are currently underway to either directly observe or indirectly detect Pop. III stars which I will briefly summarise hereafter.

2.3.1. Direct detection

A direct observation of a single Pop. III star or a Pop. III stellar population forming in a mini-halo at $z \gtrsim 15$ is basically sci-fi even with JWST. Even though their intense UV radiation would make them intrinsically luminous in the rest-frame UV, their formation sites are rare, short-lived, and located at extreme distances, making them incredibly faint. Schauer et al. (2020) highlighted the problem showing that a 1000 $M_\odot$ Pop. III star would produce a flux of three to five order of magnitudes below the NIRCAM sensitivity and that such a detection could be achieved only with an extraterrestrial 100m telescope*.

*Especially with the recent cuts in the scientific NASA budget, it does not sound such a telescope will be built soon.

The only feasible way to achieve a direct detection with JWST is to move at lower redshift ($z \lesssim 10$) and to consider a cluster rather than a single star. Zackrisson et al. (2011) and Trussler et al. (2023) showed that, Pop. III star clusters of mass $\sim 10^{5-6}$M$_\odot$ at $z \lesssim 10$ should be observable with JWST with 10-100 hours exposure time of an appropriate combination of NIRCAM and MIRI filters. However, the existence of such massive systems is highly argued in the literature. While there is a general consensus that Pop. III stars can form in pockets of pristine gas down to the EoR (e.g. Venditti et al., 2023), their characteristic masses are highly debated. Some simulations (e.g. Xu et al., 2016; Skinner & Wise, 2020) find the mass of Pop. III clusters at $z \sim 6-10$ to be $\sim 10^3$ M$_\odot$ while other works (e.g. Pallottini et al., 2014; Sarmento et al., 2018) find more optimistic values of $\sim 10^5$ M$_\odot$. The main physical mechanism that can lead to the formation of such massive systems is a strong LW background that significantly delays the Pop. III star formation in mini-halos until they surpass the atomic cooling threshold. At this point there is enough gas mass that, even with not very high star formation efficiencies, massive Pop. III clusters can form. If we account for gravitational lensing, the prospects for observability significantly improve, although a magnification factor of ~ 100 is required to detect a 10^{3-4} M$_\odot$ star cluster at $z \sim 8$. High magnifications can be obtained only in very small regions (i.e. close to *lensing caustics*) so only a very small percentage of the Universe is magnified at this level. Nevertheless, an example of an extremely magnified star at $z \sim 6.2$ exists (*Earendel*, see Welch et al. 2022). Recently, Zackrisson et al. (2024) showed that a population of highly lensed ~ 100 M$_\odot$ Pop. III stars at $z \sim 6$ may be detected by JWST in surveys covering large numbers of strong-lensing clusters.

The main observational feature associated with a Pop. III star cluster is the presence of the Helium II recombination line at $\lambda = 1640$ Å (HeIIλ1640, Schaerer 2002; Raiter et al. 2010)[†]. Since its launch, JWST detected four potential Pop. III photometric candidates at $z \sim 6-10$ (Vanzella et al. 2023; Maiolino et al. 2024; Wang et al. 2024; Fujimoto et al. 2025b). The confirmation of these sources is still pending - a JWST spectroscopic follow-up of the source identified by Fujimoto et al. (2025b) has been recently approved - and, until then, one should be cautious before announcing any bold claims (see CR7,

[†]This emission is expected from any massive source providing very hard radiation able to doubly ionize helium (e.g. Wolf-Rayet star or AGN). Hence, the HeII line alone does not prove the presence of a Pop. III star and it needs to be associated with the absence of metal lines.

Sobral et al. 2015; Bowler et al. 2017; Matthee et al. 2017). Nevertheless, if such relatively massive Pop. III clusters exist in the EoR, there is hope to detect them with campaigns such as the JWST Cycle 4 treasury program, Vast Exploration for Nascent, Unexplored Source (VENUS, Fujimoto et al. 2025a) targeting a wide survey area around sixty lensing clusters.

Finally, if (at least some) Pop. III stars form with mass below 0.8 $M_\odot$, these must have survived to the present day and they should be detectable as such (metal pollution from the ISM is negligible as shown by Tanaka et al. 2017). The best place to look for such *fossils* Pop. III stars are the low-mass satellites of the Milky Way which are expected to host the largest fraction of Pop. III survivors compared to their total stellar mass (Magg et al. 2018)[‡]. So far, no detection has been reported but even a non-detection has interesting implications as it allows to exclude the existence of low-mass Pop. III stars (e.g. Salvadori et al., 2010; Hartwig et al., 2015a; Rossi et al., 2021).

2.3.2. *Indirect detection*

While the quest for the first Pop. III direct observation continues, many studies are focusing on the observational signatures left by these objects on various high and low-redshift probes.

Given their expected large masses, the first obvious thing to look for is the associated transient events (e.g. SNe explosions and GRBs). While CCSNe are hard to detect at $z \gtrsim 6$, JWST (and possibly even the Nancy-Roman Space Telescope) should be sensitive to PISN exploding at $7 \lesssim z \lesssim 15$ (e.g. Whalen et al., 2013; Smidt et al., 2015; Venditti et al., 2024). The two main challenges are given by the rarity of these events[§] and by the difficulty in distinguishing Pop. III SNe produced by low metallicity Pop. II stars (Moriya et al. 2022). Another viable transient probe is GRBs associated with Pop. III stars, particularly long-duration events from rapidly rotating progenitors. Thanks to their brightness and detectability at very high-z (e.g. GRB 090423 at $z \simeq 8.2$ Tanvir et al.

[‡]The Milky Way bulge is expected to host the largest number of low-mass Pop. III stars although they are likely impossible to find buried by many Pop. II stars.

[§]This depends on the Pop. III SFRD and IMF. Both quantities - hence the expected PISN detection rate - are quite uncertain and model dependent. For a typical JWST NIRcam field the predicted rate is $\sim 10^{-4} - 10^{-5}$ PISNe per year (Johnson et al. 2013; Hartwig et al. 2018b; Venditti et al. 2024.

2009 or GRB 090429B at $z \sim 9.4$ Cucchiara et al. 2011), Pop. III GRBs could be captured by future missions like THESEUS (Amati et al. 2018). Still, confirming their primordial origin remains difficult due to the lack of clear distinguishing features. Additionally, their predicted detection rate is even less constrained than the SNe one since it also depends on the initial rotation of Pop. III stars and it currently ranges from ~ 100 per year for the most optimistic models (Lazar & Bromm 2022) or less than one per year for the pessimistic ones (Toma et al. 2016).

A powerful indirect probe of Pop. III stars is the 21cm signal introduced in Section 1.4.2. Pop. III stars provide the first Lyman-α and X-ray photons which heat the neutral hydrogen and couple its spin temperature to its kinetic temperature. I will not further discuss this probe here as Chapter 5 is entirely devoted to this topic.

Low-z Universe

All the observational signatures discussed so far are restricted only down to the end of the EoR. However, information on the IMF of the first stars can be obtained through *stellar archaeology* (or *near-field cosmology*) which consists in looking at the chemical composition of the atmospheres of extremely metal poor (EMP) stars and matching their abundance pattern to SN explosions to infer the properties of their Pop. III progenitors (see Frebel & Norris 2015 for a review on this topic). An interesting class of objects are the CEMP-no stars (Carbon enhanced EMP stars with no enhancement in neutron-capture elements, Keller et al. 2014; Nordlander et al. 2019). This chemical composition can be explained with Pop. III progenitors having masses between 20 and 40 solar masses for which relatively low explosion energies with significant fallback on the compact remnant is expected. Also studies on the density of Pop. III intermediate-mass black holes in the Milky Way (Mapelli et al. 2006) support this mass range for Pop. III stars with no enrichment from PISN ($M \sim 140 - 260\ M_\odot$). The only exception has been reported by Xing et al. (2023) for LAMOST J1010+2358 whose abundance pattern is well fit by a PISN imprint from a 260 $M_\odot$ progenitor (although this analysis has been later refused by Jeena & Banerjee 2024; Skúladóttir et al. 2024). More constraints might be available in the future looking at relative abundances of Damped Lyman-α systems (DLAs). These can be detected using quasar absorption spectra and they allow to measure detailed chemical

compositions at much higher-z (up to $z \sim 6$ with the recent ESO Large Programme XQR-30 D'Odorico et al. 2023). A recent work by Sodini et al. (2024) based on this sample showed a potential retention of Pop. III signatures in DLAs at $z \gtrsim 5.4$.

Finally, Pop. III stars are expected to retain more mass throughout their evolution, producing massive black holes that can form binary systems (binary black holes, BBHs). Since the discovery of gravitational waves (GW, Abbott et al. 2016) several GW events were detected by LIGO, Virgo and KAGRA featuring BBHs with component masses peaking at 30 $M_\odot$ and extending beyond ~ 65 $M_\odot$ (Abbott et al. 2021). While this might point towards a more top-heavy IMF of the progenitor stars, most of the detected mergers are expected to occur from Pop. II binaries rather than metal-free binaries, because of their higher number. Statistical features such as the mass distribution, spin alignment, and redshift evolution of merger rates, may help to distinguish a Pop. III contribution which is expected to dominate at $z \gtrsim 6$ (e.g. Santoliquido et al., 2023; Liu et al., 2024). Although current detectors are limited to much lower redshifts, future observatories like LISA and the Einstein Telescope will access the high-z GW Universe, offering a direct probe of the earliest stellar remnants and their role in cosmic history.

CHAPTER 3

Semi-analytic modelling of Pop. III star formation and metallicity evolution – I. Impact on the UV luminosity functions at z = 9–16

Fuori di me, exuvia, spiego le ali, au revoir
Un'altra chance escludila, gioco alla pari con l'età
Passati appassiti, appassiti come quadranti di Dalí
Passati parassiti, parassiti, fame di me, cannibali

Caparezza - Exuvia (2021)

This chapter is based on

E. M. Ventura, Y. Qin, S. Balu, J. S. B. Wyithe (2024),

Monthly Notices of the Royal Astronomical Society: 529, 628

Reformatted with the following changes only:

- **The text is styled and restructured to match the rest of this thesis.**
- **Where necessary, bibliographic records are updated.**

We implemented Population III (Pop. III) star formation in mini-halos within the MERAXES semi-analytic galaxy formation and reionisation model, run on top of a N-body simulation with $L = 10h^{-1}$ cMpc with 2048^3 particles resolving all dark matter halos down to the mini-halos ($\sim 10^5 M_\odot$). Our modelling includes the chemical evolution of the IGM, with metals released through supernova-driven bubbles that expand according to the Sedov-Taylor model. We found that SN-driven metal bubbles are generally small, with radii typically of 150 ckpc at $z = 6$. Hence, the majority of the first galaxies are likely enriched by their own star formation. However, as reionization progresses, the feedback effects from the UV background become more pronounced, leading to a halt in star formation in low-mass galaxies, after which external chemical enrichment becomes more relevant. We explore the sensitivity of the star formation rate density and stellar mass functions on the unknown values of free parameters. We also discuss the observability of Pop. III dominated systems with JWST, finding that the inclusion of Pop. III galaxies can have a significant effect on the total UV luminosity function at $z = 12-16$. Our results support the idea that the excess of bright galaxies detected with JWST might be explained by the presence of bright top-heavy Pop. III dominated galaxies without requiring an increased star formation efficiency.

3.1. Introduction

Chapter 2 of this thesis provides an in-depth discussion of the standard Population III star formation scenario in mini-halos (Section 2.1, the numerical methods used to simulate this process (Section 2.2), and the observational challenges associated with detecting these early stars (Section 2.3).

To address the issues of simulating Pop. III star formation in mini-halos and to identify potential observational signatures, we chose to use the semi-analytical model of galaxy formation Meraxes (Mutch et al. 2016, M16 hereafter) within a simulation that allows us to resolve all the mini-halos down to a few $10^5 M_\odot$ in a simulation of L = 10 Mpc h^{-1}. The size of this simulation is not large enough to be representative of the Universe (we will miss the most massive galaxies). However, the scales are large enough to investigate the impact of the main physical processes on the Pop. III star forma-

tion. We incorporated a number of new physical processes that are relevant to Pop. III star formation in mini-halos including: *(i)* molecular hydrogen cooling functions for mini-halos, *(ii)* baryon-dark matter streaming velocities, *(iii)* photo-dissociation of H_2 molecules from the Lyman-Werner background and *(iv)* the chemical evolution of the intergalactic medium. This latter effect has been implemented assuming that metals are released through supernova explosions and within a bubble that expands accordingly to the Sedov-Taylor model (the approach is very similar to the analytical calculation shown in Furlanetto & Loeb 2003). We found that these bubbles are generally small and that they roughly agree with the previous estimate by Trenti et al. (2009), with typical radii of 150 ckpc at $z = 6$. The implementation of both internal and external metal enrichment allows us to understand whether a galaxy will form Pop. III or Pop. II stars and thus quantify the impact of Pop. III galaxies on the total luminosity function at $z \geq 5$. This chapter is structured as follows:

In Section 3.2, we present the new physics implemented in MERAXES. In Section 3.3, we show the main global properties of the Pop. III star formation across cosmic history discussing which parameters have a stronger impact on the global star formation history and on the metallicity of the IGM. In Section 3.4 we discuss the SED evolution of Pop. III galaxies and the UV luminosity functions at $z = 9 - 16$ for different Pop. III IMFs. Finally, we discuss our main results and conclusions in Section 3.5.

3.2. Pop. III star formation in meraxes

In the previous version of the SAM MERAXES (Mutch et al. 2016, Qin et al. 2017; Qiu et al. 2019 and Section 1.5.3) the galaxies are assumed to form in a previously chemically enriched Universe and inside atomic cooling halos. Such an approximation does not allow us to study the first episodes of star formation that mostly occurred in mini-halos when the Universe did not have any metals. The version of MERAXES presented in this work allows us to compute the physics of the first episodes of star formation from the initial molecular cooling of the gas to the external metal enrichment from the supernova feedback. As in the previous work, MERAXES is coupled to the reionization so that all the radiative backgrounds are computed in a self-consistent way from the galaxy properties.

This has been done by implementing a modified version of 21cmFAST (Mesinger et al. 2011) that includes the local ionizing UV background from Sobacchi & Mesinger (2014) and the X-ray heating (Balu et al. 2023a). In this version, we also included the Lyman-Werner background.

3.2.1. *High-Resolution N-body simulation*

The updates to MERAXES for Pop. III necessitate high mass and spatial resolution. For this purpose, we introduce L10_N2048 (hereafter L10) from the *Genesis* suite of dark matter only N-body simulations. L10 is a periodic cubical simulation of side 10 h^{-1} Mpc and consists of 2048^3 dark matter particles of mass $m_p = 9.935 \times 10^3 h^{-1} M_\odot$ resulting in a halo mass resolution of $\sim 3.18 \times 10^5 h^{-1} M_\odot$ (based on a minimum of 32 particles per halo). The simulation, run using the SWIFT (Schaller et al., 2018) cosmological code, evolves these dark matter particles from $z = 99$ down to $z = 5$. The halos were identified using the friends-of-friends phase space halo-finder VELOCIRAPTOR (Elahi et al., 2019a) and the merger trees were constructed using TREEFROG (Elahi et al., 2019b). We note that the mass resolution achieved in this simulation allows us to resolve all the mini-halos below $z \sim 30$ and is the highest resolution on which MERAXES has been run. The output trees of the N-body simulation used in this work are available on Zenodo at Balu et al. (2024).

3.2.2. *Molecular cooling*

The first process in order to enable star formation is the cooling of the gas. For dark matter halos with $T_{\rm vir} \geq 10^4$ K, the main coolant is the atomic hydrogen, while in mini-halos (10^3 K $\leq T_{\rm vir} < 10^4$ K), the cooling occurs via roto-vibrational transitions of molecular hydrogen (e.g. Tegmark et al., 1997). For the details on how the cooling of the gas is implemented in MERAXES, we refer the reader to M16; in this section, we only highlight the main differences between the atomic and the molecular cooling.

As in M16, we compute the ratio of the specific thermal energy to the cooling rate per unit volume:

$$t_{\rm cool}(r) = \frac{1.5 \bar{\mu} m_p k T}{\rho_{\rm hot}(r) \Lambda(T, f_{H_2})} \tag{3.1}$$

where $\rho_{\rm hot}(r)$ is the gas density profile (we assume a singular isothermal sphere), k is the Boltzmann constant, and T is the temperature of the gas (which we set to be the virial temperature of the halo). M16 included only atomic cooling halos. Thus they set the mean molecular weight $\bar{\mu} = 0.59$ assuming a fully ionized gas and the cooling function $\Lambda(T)$ in units of erg cm^{-3} s^{-1} from Sutherland & Dopita (1993). For mini-halos we instead set $\bar{\mu} = 1.22$ (fully neutral gas) and implement the molecular hydrogen cooling functions $\Lambda(n_{\rm H}, T)$ from Galli & Palla (1998). This choice is valid as long as we assume that the cooling inside mini-halos occurs only due to H_2. This may not be valid as, if a mini-halo is chemically enriched with metals by a nearby halo, metals are much more effective in the cooling of the gas (e.g. Nebrin et al., 2023). However, as we will show in section 3.3, this enrichment is almost ineffective at $z > 10$. The molecular cooling function Λ depends on the gas density of the halo (which can be directly computed for each galaxy assuming an isothermal sphere) and on the molecular hydrogen fraction f_{H_2}. For the latter we assumed a fixed value of 0.1%, which is consistent with results from Nebrin et al. (2023) for halos of $T_{\rm vir} \simeq 5 \times 10^3$K at $z = 15 - 20$*. As in M16, the cooling time is used to find a cooling radius that determines the amount of gas that is cooled down.

3.2.3. *Streaming velocities*

As a first approximation, gas in a mini-halo can start to cool down the gas once it reaches the virial temperature of $\simeq 10^3$ K. From Barkana & Loeb (2001), adopting $\mu = 1.22$ for a fully neutral gas, this requirement would correspond to a minimum virial mass of (Visbal et al. 2015):

$$M_{\rm min,H_2} = 2.5 \times 10^5 \left(\frac{26}{1+z} \right) M_\odot. \tag{3.2}$$

However, there are a number of effects that can decrease the amount of molecular hydrogen present in the halo, reducing the cooling efficiency and ultimately increasing the minimum virial mass of a halo capable of cooling (see Nebrin et al. 2023 for an extensive discussion and comparison between results found in different simulations.)

*The exact value of $f_{\rm H_2}$ depends on the virial mass of the halo, redshift and the time available for H_2 formation in the minihalo (which is likely to be a multiple of the free fall time). To compute the exact value of $f_{\rm H_2}$ is beyond the aim of this work, hence we chose an average value.

A non-radiative process that can delay the gas cooling in very low-mass halos is the streaming velocity between baryons and dark matter (Tseliakhovich & Hirata 2010). This effect is a consequence of the different decoupling of baryons and dark matter particles from photons that results in a velocity difference between the two species of v_{bc} that can be expressed as a constant multiple of the root-mean-square (rms) streaming velocity $\sigma_{bc} = 30 \times (1+z)/1000$ km s^{-1}. The presence of a relative motion between baryons and dark matter particles will make it harder for baryons to fall into the potential wells of dark matter halos, delaying the accretion and, hence, the cooling of the gas in mini-halos. The main outcome of this physical process is to delay the very first episodes of star formation around $z \sim 40$. Throughout this work, we implemented the effect of the streaming velocities as per other semi-analytical models based on a fitting function found by Fialkov et al. (2012), which is calibrated to reproduce the results of the hydrodynamical simulations of Greif et al. (2011a) and Stacy et al. (2011):

$$V_{\mathrm{cool,H_2}} = (a^2 + (bv_{bc})^2)^{0.5}, \tag{3.3}$$

where a = 3.714 km s^{-1} and b = 4.015 km s^{-1}. Equation 3.3 provides the minimum circular velocity that a halo needs to have in order to have enough H_2 to cool down the gas. $V_{\mathrm{cool,H_2}}$ can be easily converted into a virial mass $M_{\mathrm{cool,H_2}}$ using the formula in Barkana & Loeb (2001). In this work we fixed $v_{bc}(z) = \sigma_{bc}(z)$ and we assumed this value for the entire box.[†]

3.2.4. *LW background*

A self-consistent model of star formation in mini-halos must consider the photo-dissociation of H_2 from UV photons in the Lyman-Werner (LW) band ([11.2 - 13.6] eV). LW photons destroy H_2 and thus prevent mini-halos gas from cooling (Haiman & Bryan 2006). We implement this effect by changing the minimum mass for molecular cooling using the

[†]This assumption is not entirely accurate as the streaming velocities are roughly constant up to a scale of a few Mpc while our box is larger than 10 Mpc. However, the effect of streaming velocities is dominant only at $z \geq 30$ before the first stars form, and the Lyman-Werner background is built up.

fitting from Visbal et al. (2015):

$$M_{\rm crit,MC} = M_{\rm cool,H_2}[1 + 22.87 \times J_{\rm LW}^{0.47}]. \tag{3.4}$$

This critical mass only applies to minihalos which are below the atomic cooling halo mass threshold. In the absence of an LW background, this equation simply gives $M_{\rm crit,MC}$ as defined in Section 3.2.3. $J_{\rm LW}$ is the LW flux in units of 10^{-21} erg s^{-1} cm^{-2} Hz^{-1} sr^{-2} that reaches the minihalo. LW photons have a mean free path of ~ 100Mpc, so each minihalo will be affected even by distant galaxies that formed at higher redshift. Thus, we modelled the LW background by integrating contributions across the cosmic history (see a similar approach in Qin et al. 2020 which is briefly summarized below.)

As for all the radiative backgrounds in MERAXES, we follow an excursion-set formalism (Furlanetto et al. 2004) which counts the number of photons in a certain band in spheres of radius R centred at location and redshift (x,z). We decrease the radius down to the size of the cell $R_{\rm cell}$. At each of these locations, we compute the LW emissivity $\epsilon_{\rm LW}(\mathbf{x}, z')$ using the spectral energy distributions from Barkana & Loeb (2005). These give $\frac{dn}{d\nu}$: the number of photons per solar mass per unit frequency for both Pop III and Pop II stars. We assume that LW photons are absorbed only at resonant frequencies (thus we are neglecting any absorption from H_2 in the IGM) where $\nu_{\rm n} = \nu_{\rm LL}(1 - n^{-2})$ and $\nu_{\rm LL} = 3.29 \times 10^6$ GHz is the Lyman limit frequency. Under these approximations, we can compute the LW emissivity smoothed over R at redshift z and location x for sources emitted at redshift z' as:

$$\epsilon_{\rm LW}(\mathbf{x}, z'|z, R) = \sum_{\rm i=III,II} {\rm SFRD}^i \sum_{n=2}^{n_{\rm max}(z)} \int_{\max(\nu'_{\rm n}, \nu_{\rm LW})}^{\nu_n+1} \frac{dn^i}{d\nu''} h d\nu'' \tag{3.5}$$

In the equation above, we directly link the star formation rate density (SFRD) for both Pop. III and Pop. II stars (which we can compute from MERAXES) to the LW emissivity summed over the Lyman series. This sum accounts for the resonances in the Lyman series (Lyman-n photons will be absorbed and re-emitted as a Lyman$-\alpha$ photon). Given the large mean free path of LW photons, we must also account for distant galaxies at higher redshift $z' > z$ with the redshifted spectrum $\nu' = \nu \frac{1+z'}{1+z}$. The sum of these two

effects causes the peculiar shape of the LW spectrum (see Fig. 2 in Qin et al. 2020). Following Barkana & Loeb (2005) we account for all the Lyman resonances with $n \leq 23$. Under these approximations we can find the maximum redshift $z_{\rm max}$ from which a LW photon can reach z:

$$z_{\rm max} + 1 = (z+1)\frac{1-(n+1)^{-2}}{1-n^{-2}}. \tag{3.6}$$

Finally, we need to convert the emissivity into a flux following (Qin et al. 2020):

$$J_{\rm LW}(\mathbf{x}, z|R) = \frac{(z+1)^3}{4\pi}\int_z^\infty dz' \frac{cdt}{dz'}\epsilon_{\rm LW}. \tag{3.7}$$

The approach described above differs from the one in 21cmFAST only for the computation of the SFRD. In Qin et al. (2020), the SFRD is estimated from the density field and the collapsed fraction, while in this work, it is computed directly from MERAXES, which tracks the formation of each galaxy and its entire star formation history.[‡].

Together with the LW background, the main radiative feedback that suppresses star formation is the UV photo-ionization (the ionizing UV background inhibits gas accretion in low-mass halos Sobacchi & Mesinger 2013). We used the same prescriptions as in M16, which consists of reducing the baryon content through a baryon fraction modifier $f_{\rm mod}$ (that depends on the local ionizing rate and the time when the nearby IGM becomes ionized) that stops the gas infall. In difference from the LW feedback, the UV photo-ionization is relevant only during reionization ($z \leq 10$), and it also affects atomic cooling halos as massive as $\sim 10^{9.5} M_\odot$.

3.2.5. *Metal Evolution*

Once stars start to form in the Universe, they also explode as supernovae, releasing metals. Most of these will stay inside the same galaxy, contributing to the chemical enrichment of the galaxy itself. This process is commonly known as "genetic" enrichment

[‡]In this work, we are not accounting for the self-shielding of H_2, which acts against the H_2 photo-dissociation and thus might enhance the molecular cooling in mini-halos (Hartwig et al. 2015b; Schauer et al. 2021; Chiaki & Wise 2023) increasing the Pop. III SFRD (Feathers et al. 2023). Kulkarni et al. (2021) provided a fitting formula for $M_{\rm crit,MC}$ accounting for the H_2 self-shielding. Since this affects only the LW feedback, the combined effect of the LW background and the streaming velocities in Kulkarni et al. (2021) is not multiplicative as assumed in Eq. 3.4

and is likely to be the main mechanism of chemical enrichment of the Universe. However, some of the metals escape their parent galaxy. In this case, they will pollute the nearby IGM, and if later a galaxy forms in a region where the IGM was enriched, the new galaxy will be pre-enriched with metals. This latter mechanism is referred to as "external" metal enrichment (e.g. Pallottini et al., 2014; Smith et al., 2015; Hartwig et al., 2018a; Visbal et al., 2020; Yamaguchi et al., 2023). Keeping track of the metallicity evolution of the Universe is crucial in order to put constraints on when the Pop. III/II transition occurred.

We account for both processes, and we are able to follow the metallicity evolution of the IGM. Firstly, we choose a critical metallicity $Z_{\rm crit} = 10^{-4} Z_{\odot}$ as the threshold value below which a galaxy will form Pop. III stars. All new galaxies, unless externally polluted, will accrete pristine gas (without any metals) onto the hot gas reservoir. This gas, once it cools, will provide the reservoir for the star formation. Hence, a galaxy that is not externally polluted will always form Pop. III stars for the first time. At each snapshot, we compute the metallicity of the cold gas reservoir from the amount of metals released by earlier supernovae and if this is higher than $Z_{\rm crit}$, the galaxy will form Pop. II stars, otherwise it will form Pop. III.

While internal enrichment is the main mechanism that drives the Pop.III/II transition, some galaxies can be externally enriched through supernova winds originating in a nearby galaxy. Once several supernovae in a galaxy go off, they will form a "superbubble" that will expand outside the galaxy escaping the binding energy of the dark matter halo. We followed the expansion in time of this "metal bubble" using the analytic approximation in Dijkstra et al. (2014):

$$r_{\rm bubble}(t) = \left(\frac{\Delta E_{\rm SN}}{m_{\rm p} n_{\rm gas}} \right)^{0.2} t^{0.4}. \tag{3.8}$$

All quantities that appear in this equation are computed in MERAXES. $\Delta E_{\rm SN}$ is the total supernova energy released at a certain snapshot, and it is computed using the stellar mass that goes supernova in that snapshot multiplied by the supernova explosion energy (see Eq. 11 in M16). $n_{\rm gas}$ is the number density of the gas to which the bubble has expanded (while the bubble is smaller than the virial radius, this is the gas density of the galaxy; otherwise, the density of the IGM), and t is the time since the explosion occurred.

We assume that all the supernova events will occur in the middle of the snapshot[§]. Note that since MERAXES accounts for both contemporaneous and delayed supernova feedback (see more in M16), each galaxy has several bubbles associated with the same star formation episode. However, we consider only the largest of these bubbles so that each galaxy has only one associated bubble. Having calculated the bubble size, we can predict if a nearby galaxy will accrete pristine or enriched gas. In order to reduce the computational cost, we avoid computing the distance between all the pairs of galaxies and instead use the grid-based approach outlined below:

- Build a high-resolution grid with $N_{\rm grid}^3$ cells smoothing the matter density grid from the N-body simulation. The size of the cell is chosen so that the volume of the cell is similar to the volume of the typical bubble at the end of the simulation ($R_{\rm ave,bubble} \simeq 100$ckpc, see Fig. 3.2). For our box, this requirement is satisfied when $N_{\rm grid} = 128$. This ensures that the metal bubble will not overflow outside the pixel where it originates.

- For each cell i, we compute the average metallicity $Z_{\rm IGM,i}$ as the ratio between the sum of the metals ejected by all galaxies inside the cell and the total gas in the cell:

$$Z_{\rm IGM,i} = \sum_{j}^{N} \frac{M_{\rm MetalsEj,j}}{M_{\rm IGM,i} + M_{\rm EjGas,j} - M_{\rm gas,j}}. \tag{3.9}$$

  Here $M_{\rm IGM,i} = \rho_{\rm crit}\Omega_m(1+\delta_i)f_b d^3$ is the total baryonic mass inside each cell which depends on the average matter overdensity of the cell δ_i and the cell size d. $M_{\rm EjGas}$ and $M_{\rm gas}$ are respectively the total mass of the ejected gas and the bounded gas of each galaxy. We only let the galaxies with $r_{\rm bubble} \geq 3 \times R_{\rm vir}$ contribute to $M_{\rm MetalsEj,j}$ and $M_{\rm EjGas,j}$. For the computation of the metals ejected from Pop. II galaxies, we refer the reader to M16 and Qiu et al. (2019) and for Pop. III galaxies to Section 3.2.6.

- For each cell i, we compute the volume fraction filled with metals (the metal filling fraction), summing the volume of the largest bubble surrounding each galaxy

[§]This assumption is not self-consistent with the luminosity computation of Pop. III galaxies, which assumes stochastic Pop. III star formation (see section 3.2.7).

within the pixel and dividing by the cell volume. As above, we account only for those galaxies with $r_{\rm bubble} \geq 3 \times R_{\rm vir}$. This choice reflects the fact that a central galaxy needs to be surrounded by a bubble at least as large as its virial radius in order to pollute a nearby galaxy. The factor of 3 has been chosen given that the distance between two central galaxies in our simulation is always larger than three times the virial radius of the biggest galaxy. Hence, the metal filling factor for the cell i is $Q_{\rm metal,i} = \frac{\sum_j^N V_{\rm bubble,j}}{V_i}$.

- At the beginning of each snapshot, we assign the probability p for external metal enrichment to each galaxy inside the cell i. This probability will be given by the metal filling factor Q_i. This choice assumes that the galaxies are randomly distributed within each pixel. This assumption holds only if we use a high-resolution grid where the pixel size is small enough such that clustering effects are negligible.

- We assign a random number m between 0 and 1 to each newly formed galaxy, and at each snapshot, we compare this random number to p. When the condition $m \leq p$ is satisfied, we label that galaxy as externally enriched, and it accretes enriched gas with a metallicity equal to the average metallicity of the cell that belongs to ($Z_{\rm IGM,i}$). Furthermore, when a galaxy experiences a star formation episode, we enforce $p = 1$ (in this latter case, we know that this galaxy will be inside its own metal bubble and thus cannot accrete pristine gas). With this latter condition and internal enrichment, we effectively stop Pop. III star formation inside a galaxy after the first supernova episode.

We illustrate an example in Fig. 3.1, where we selected a 2D slice of our L10 box at z = 10 with a thickness of $0.078h^{-1}$cMpc. The red (blue) dots are the galaxies with $M_{\rm vir} \geq 10^6 M_\odot$ (not) externally metal-enriched, while the green dots are previously formed galaxies with $\rm r_{bubble} \geq 0.05h^{-1}$ cMpc. For a better visualization, we zoomed into a slice with $0.24h^{-1}$ cMpc on a side showing the actual size of the metal bubble (right plot). Inside this region, all the 7 galaxies that formed inside the bubble are actually marked as externally enriched. At the same time, the 5 galaxies that are marked as not enriched lie outside the bubble, showing that the adopted approximation works quite well (see the end of this section for a more detailed discussion). This demonstrates

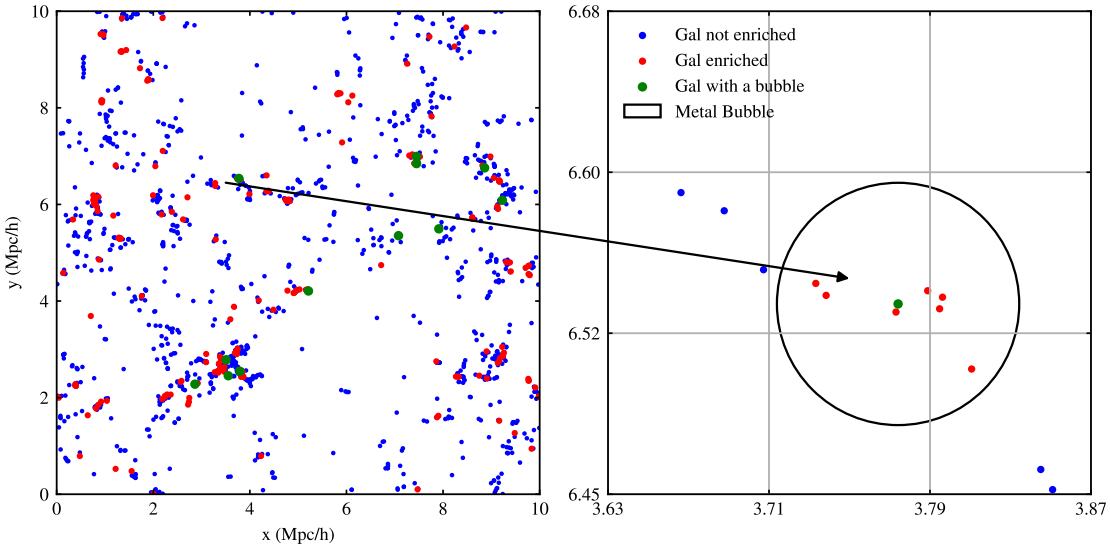

Figure 3.1: **left:** 2D slice of the L10 box at $z = 10$ with the position of all the galaxies with $M_{\rm vir} \geq 10^6 M_\odot$ (blue dots) highlighting the ones that are externally metal enriched (red dots). The green dots are galaxies with an associated metal bubble larger than 0.05 h^{-1} cMpc. The slice is 10 h^{-1} Mpc on a side and $\sim 0.078 h^{-1}$Mpc thick. **right:** zoom-in of a single pixel (0.24 h^{-1} Mpc on a side). The circle represents the actual size of the bubble around the green dot.

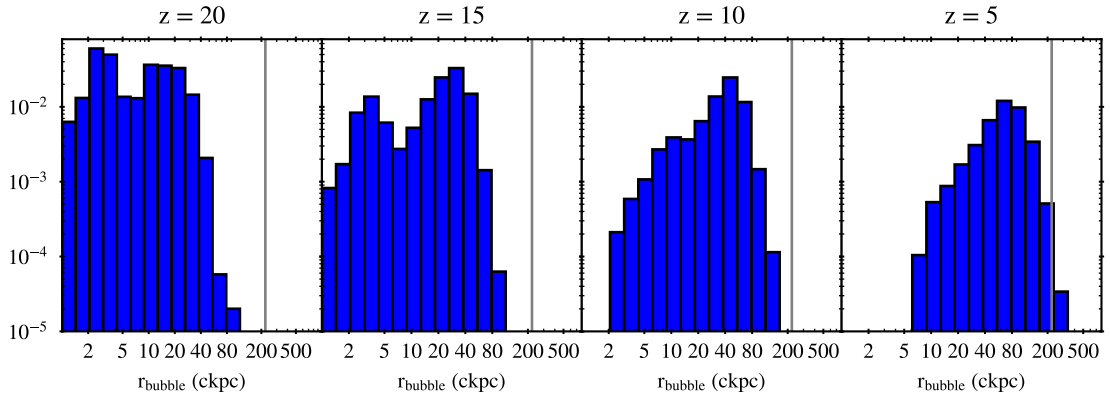

Figure 3.2: Distribution function of the metal bubble size computed according to Eq. 3.8 at 4 different redshifts. The grey column indicates the predicted value for the maximum bubble size at z = 6 from Trenti et al. (2009).

that this method can reproduce the statistical properties of inhomogeneous metal enrichment. The main limitation of this technique is that we are not accounting for the overlap of the bubbles and thus are overestimating the metal-filling factor and underestimating the metallicity of those galaxies that are polluted from more than one galaxy. However, given the small size of the bubbles (see discussion in Section 3.3 and Fig. 3.2), this is not a major factor, especially prior to reionization. We note that the methodology shown here is similar to Sassano et al. (2021) with the main differences being that we divided the volume of our simulation in cells allowing a more precise computation of the metallicity of the enriched regions.

Fig. 3.2 shows the bubble size distribution function (r_{bubble} in ckpc) at redshift 20, 15, 10 and 5. From this plot, we see the bubble growth over time from a typical radius of ~ 30 ckpc at $z = 20$ to ~ 150 ckpc at $z = 5$. These values are consistent with the results shown in Trenti et al. (2009) ($r_{bubble} \leq 150h^{-1}$ ckpc at $z = 6$) with only a few bubbles at $z = 5$ larger than this value.

Fig. 3.3 shows the IGM metallicity (top row), metal filling factor (middle row) and density (bottom row) maps at four different snapshots. The red (blue) cells in the top row have $Z_{IGM} \geq (<) Z_{crit}$ indicating that galaxies that will be externally polluted in those cells will accrete enriched (pristine) gas and will form Pop. II (III) stars. Comparing the maps at the same snapshot, we see that the more overdense regions have a larger filling factor and a higher metallicity as these hosts more galaxies, hence more metal bubbles. Fig. 3.3 also shows the progressive enrichment of the IGM over the cosmic history since, as we move to lower redshift (from left to right panels) we have more enriched cells and with larger filling factors.

Testing the external metal enrichment

Here we discuss the extent to which our approximation on the external metal enrichment based on the filling factor is appropriate and when it fails.

Since we are avoiding computing all the pairs of distance, there might be some galaxies for which we are not getting a correct enrichment. For this reason, we computed in post-processing the distance between all the pairs of galaxies throughout the entire simulation and we counted how many galaxies in MERAXES are marked as externally metal

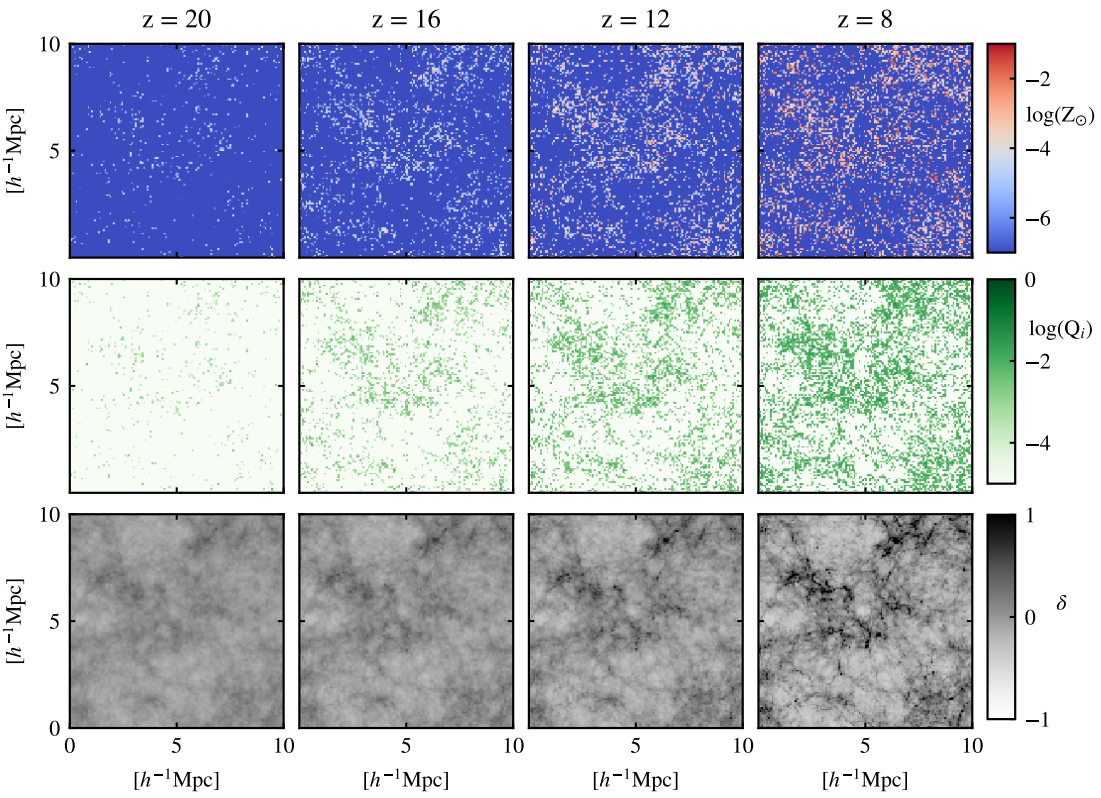

Figure 3.3: 2D projections of the IGM metallicity $\log(Z_{\rm IGM})$ in solar units (top row), the metal filling factor $\log(Q)$ (middle row) and the overdensity δ (bottom row). From left to right, the columns correspond to the same redshift: $z = 20, 16, 12, 8$. Each slice is 10 h^{-1} Mpc on a side and considers the average contribution over the entire thickness of the box. In the top row, red (blue) represents enriched (pristine) pixels: $Z_{\rm IGM} \geq (<) Z_{\rm crit}$. Green pixels have a larger filling factor Q, indicating a larger probability of a galaxy accreting enriched gas. Dark cells in the bottom row have larger mean overdensity δ.

enriched (pristine) even if they are outside (inside) a metal bubble. We repeated this computation for several grid resolutions: N = 16, 32, 64, 128 and 256. Hereafter, we will call "false pristine galaxies" those galaxies that lie inside a metal bubble (and so should be enriched) but in MERAXES are labelled as pristine and "false enriched galaxies" those galaxies that are not reached by any bubble but in MERAXES are labelled as enriched.
In the left panel of Fig. 3.4 we computed the mass fraction of the false pristine (solid line) and false enriched galaxies (dashed line) using different metal grid resolutions. At lower resolution, the percentage of the false pristine galaxies increases from 4% at N = 128 (black line) to 7% at N = 16 (blue line). This happens since, as the pixel becomes bigger, the assumption of the galaxies randomly distributed inside each pixel is no longer valid as the clustering becomes much more important. However, when we use a very fine grid (N = 256, grey line), the mass fraction of false enriched galaxies dramatically increases at $z \leq 10$. This happens because by $z = 10$, the typical bubble size becomes larger than the pixel volume ($r_{\rm bubble} \simeq 40-80$ ckpc, see Fig. 3.2), and so we lose all the contribution that overflows outside the pixel. The mass percentage of false enriched galaxies instead is only mildly affected by different resolutions (always below 2%). We then compute the absolute value of the difference between the mass percentage of the false pristine and the false enriched galaxies (middle panel). This quantity tells us if, statistically, we are reproducing the correct global enrichment of the Universe, and it tells us whether or not we can apply this model to study the global properties of the Universe. We can see that having a high-resolution grid significantly improves the quality of our results. For N = 128, this difference is always below 2%, and at z < 12 is approximately 0%. This tells us that for a high-resolution grid, globally, we are getting the correct enrichment of the Universe as the mass percentage of false pristine and false enriched galaxies cancels out. This agreement is almost perfect during the EoR, while during the Cosmic Dawn is still very good, but we are underestimating the metal enrichment of $\sim$ 1-2%. Finally, we are also showing the sum between the false enriched and pristine galaxies (right panel). This quantity instead tells us what is the mass percentage of galaxies for which we are getting a wrong estimation of the enrichment and it is particularly important if we want to apply this model to study analogues. Increasing the resolution improves our result, which, for N = 128, peaks at $\sim$ 4% during the Cosmic Dawn. In conclusion, our model

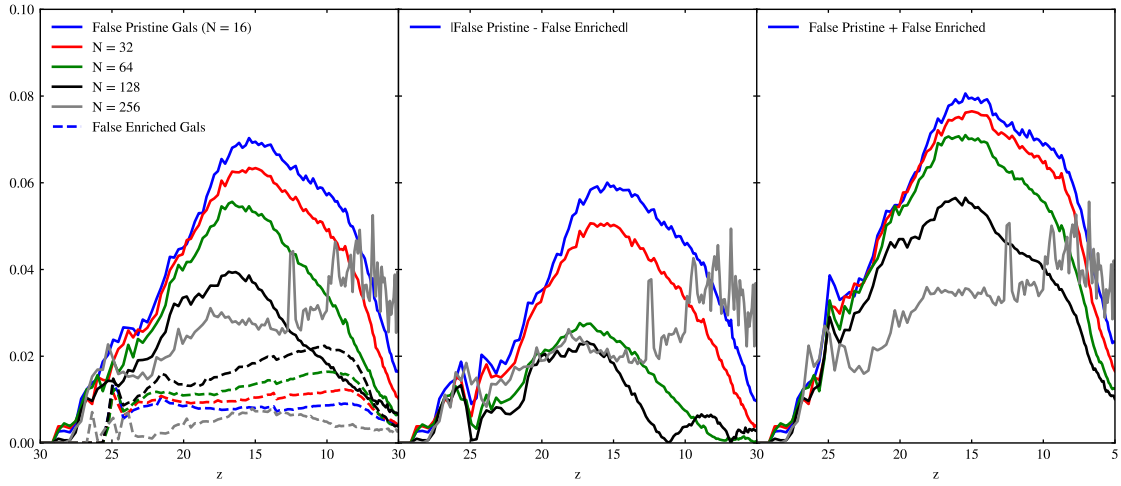

Figure 3.4: **left:** mass fraction of false pristine (solid line) and false enriched (dashed line) galaxies (see text for details). Blue, red, green, black and grey lines refer to different grid resolutions (N = 16, 32, 64, 128, 256 respectively). **center:** absolute value of the difference between the mass fraction of false pristine and false enriched galaxies. The same colour coding is adopted. **right:** sum of the mass fraction of false pristine and false enriched galaxies. The same colour coding is adopted.

for N = 128, while reducing the computational cost, still gives an excellent agreement on global enrichment and a very good agreement on the enrichment of single galaxies.

3.2.6. Pop. III star formation

In this work we modify Pop. II description in M16 to allow star formation in Pop. III galaxies (see Section 2.4 in M16). In particular, once a galaxy reaches a mass of cold gas larger than a critical value $m_{\rm crit}$, this galaxy will convert the cold gas into stars according to the star formation efficiency $\alpha_{\rm SF}$. The value of $m_{\rm crit}$ is computed as in M16 and is determined by a critical surface density $\Sigma_{\rm norm}$ of the gas in the cold disk. Since we are now considering two different stellar populations, we adopted two different free parameters, both for the star formation efficiency $\alpha_{\rm SF,III}$ and for the critical surface density $\Sigma_{\rm crit,III}$. Recent full hydrodynamical simulations that follow the collapse of a pristine gas cloud until a Pop. III star is formed (e.g. Hirano et al., 2014; Stacy et al., 2016; Chon et al., 2021), suggest that the Pop. III IMF is shifted to larger masses as a result of less fragmentation due to inefficient cooling. Within this work, we adopted the IMFs from Raiter et al. (2010) (see Table 3.2), while for Pop. II stars, we assumed a Kroupa (2001) IMF. For the

fiducial model, we chose a Salpeter IMF with a mass between 1 and 500 $M_\odot$. The choice of the IMF is crucial as it determines many properties of the stellar population, including what fraction of stars will explode as supernovae and, hence, the amount of energy and metals injected into the IGM. In this work, we explore the impact of the 4 free parameters discussed above (see also Table 3.1) since these have the strongest impact on the Pop. III star formation history. MERAXES includes more free parameters describing the energy coupling efficiency of the supernova explosion (see M16 and Qiu et al. 2019) that will not be explored in this work (we will take the same fiducial values as for Pop. II). Since the focus of this work is on the first galaxies formed during the Cosmic Dawn, we do not explore parameters describing the UV ionizing and X-ray radiation (e.g. escape fraction), and we will take the same fiducial values as in the previous works (see Balu et al. 2023a). Those will be discussed in a future work focused on the EoR using a larger box.

The fate of a zero-metallicity star is quite uncertain due to the many poorly constrained physical mechanisms. Here, we adopt a simplified picture of the final fate of a Pop. III star depends only on its initial mass (Heger & Woosley 2002). For masses below 8 $M_\odot$, there will be no SN event. If $M_\star \in [8, 40] M_\odot$ it will explode as a core-collapse SN (CCSN) leaving a remnant, if $M_\star \in [140, 260] M_\odot$ there will be a pair-instability SN (PISN) leaving no remnant and if $M_\star \in [40, 140] M_\odot$ or $M_\star > 260 M_\odot$ stars collapse directly into a black hole (BH) with negligible feedback. Given the different endings of a Pop. III star life, the choice of the IMF is crucial to compute the timing of delayed supernova feedback. While we use the technique of Qiu et al. (2019) for Pop. II stars with precomputed tables assuming a Kroupa IMF (Kroupa 2001), for Pop. III supernova feedback we estimated the amount of SN energy and metal yields with an analytic calculation as in M16. The total energy provided by Pop. III supernovae explosions at the snapshot j is:

$$\begin{aligned} \Delta E_{\mathrm{total,III,j}} &= \sum_{i=j-17}^{i=j} \left(\Delta E_{\mathrm{CCSN,III,j}} + \Delta E_{\mathrm{PISN,III,j}} \right) \\ &= \epsilon_{\mathrm{energy}} \Bigg(\sum_{i=j-17}^{i=j} \left(\Delta m^{\mathrm{i}}_{\star,\mathrm{III}} \eta^{\mathrm{i}}_{\mathrm{III,CCSN,j}} E_{\mathrm{CC}} \right) \\ &\quad + \Delta m^{\mathrm{j}}_{\star,\mathrm{III}} \eta_{\mathrm{III,PISN}} E_{\mathrm{PISN}} \Bigg), \end{aligned} \tag{3.10}$$

where $\Delta m^{\rm i}_{\star}$ is the new stellar mass formed at an earlier snapshot i, $\epsilon_{\rm energy}$ is the energy coupling efficiency (Qiu et al. 2019), $E_{\rm CC} = 10^{51}$ erg and $E_{\rm PISN} = 10^{53}$ erg are the typical energy for a core collapse and a pair-instability supernova respectively and

$$\eta^{\rm i}_{\rm III,CCSN,j} = \int_{m^i_{\rm min,j}}^{m^i_{\rm max,j}} \phi(M) dM \tag{3.11}$$

$$\eta_{\rm III,PISN} = \int_{140M_\odot}^{260M_\odot} \phi(M) dM \tag{3.12}$$

are respectively the fraction of stars formed during snapshot i that go core collapse and pair-instability supernova in snapshot j. These are computed by integrating the chosen IMF over the correct mass limits. Assuming that all-star formation occurred in the middle of the snapshot, $m^i_{\rm min,j}$ and $m^i_{\rm max,j}$ for CCSN are computed from the lifetimes for Pop. III stars using Schaerer (2002) assuming no mass loss and zero metallicity. We highlight that a zero metallicity star with $M \in [140, 260]$ has a lifetime smaller than the time separation between two consecutive snapshots in MERAXES; hence, it will explode as a PISN in the same snapshot in which it forms. For this reason, in Eq. 3.12, the mass limit for $\eta_{\rm PISN}$ is the entire mass range of the PISN and when computing the total energy from PISN injected at snapshot j in Eq. 3.10 we consider only the stars that are formed at snapshot j. For CCSN, instead, we keep track of the star formation history over the last 17 snapshots, which correspond to $\gtrsim 40$ Myr, after which all stars with $M \geq 8M_\odot$ will already be exploded. To compute the amount of gas that is reheated and ejected from the halo, we adopted the same prescription as Qiu et al. (2019).

We also update the amount of ejected gas and metals from Pop. III stars. These are taken from Heger & Woosley (2010) assuming non-mixing (no rotation) and a supernova explosion of 1.2 $\times 10^{51}$ erg. As in M16, when a star goes core-collapse supernova at snapshot j, it will release an amount $\Delta m_{\rm CCSN,Z,j}$ of metals and $\Delta m_{\rm CCSN,X,j}$ of gas into the interstellar medium:

$$\Delta m_{\rm CCSN,Z,j} = \sum_{i=j-17}^{i=j} \frac{\Delta m^i_{\rm CCSN,Z,j}}{m_{\rm CCSN}} \Delta m_{\star}, \tag{3.13}$$

where $m_{\rm CCSN}$ is the total fraction of stars that ends as a CCSN:

$$m_{\rm CCSN} = \int_{8M_\odot}^{40M_\odot} M\phi(M)dM \tag{3.14}$$

and $\Delta m_{\rm CCSN,Z;i,j}$ is the amount of metals released by a star formed at snapshot i and going supernova at snapshot j:

$$\Delta m^i_{\rm CCSN,Z,j} = \int_{m^i_{\rm min,j}}^{m^i_{\rm max,j}} M\phi(M)ZdM. \tag{3.15}$$

In the above equation, Z is the metal mass fraction released into the ISM from supernovae, and it is incorporated inside the integral because it is not fixed over the mass range (i.e in stars with $M_\star \geq 25M_\odot$ most of the metals will fall onto the remnant due to the massive fallback). With an entirely analogous calculation, it is possible to find $\Delta m_{\rm CCSN,X,j}$ (we just need to replace Z with the gas mass fraction X). Once again, we are doing delayed SN recycling only for CCSN because, in the case of pair instability, all the feedback is contemporaneous. For PISN, we considered the gas and metal yields from Heger & Woosley (2002).

In all the previous MERAXES works, all the stellar mass locked up in remnants (neutron stars and BHs) was neglected as it was recycled into the gas mass budget of the galaxy. We decided to drop this approximation for Pop III stars as they are likely to leave more massive remnants (some might be massive enough to be the first "light" seeds of supermassive BHs). Firstly, we need to consider the BHs that formed after a "failed SN scenario" typical of a star with an initial mass $M_\star \in [40, 140]M_\odot$ and $M_\star > 260M_\odot$. The BH mass arising from this scenario will be:

$$m_{\rm BH} = \Delta m_\star \left(\int_{40M_\odot}^{140M_\odot} M\phi(M)dM + \int_{260M_\odot}^{M_{\rm max}} M\phi(M)dM \right). \tag{3.16}$$

Finally, we need to account for the BH remnants that are left after a CCSN. In this case, we use equations 3.13 and 3.15 substituting the metal mass fraction with the BH mass fraction $B = (1 - X - Z)$ (since all the remaining material that has not been ejected is locked onto the stellar remnant). MERAXES, does not evolve the remnants (via accretion),

Table 3.1: Free parameters of Pop. III star formation.

Parameter	Description	Fiducial value (Pop II)
α_{SF}	Star formation efficiency	0.008 (0.08)
Z_{crit}	Critical metallicity for Pop III star formation	$10^{-4} Z_{\odot}$
Σ_{norm}	Critical surface gas density for Pop III star formation	0.37 (0.37) $M_{\odot}$ pc^{-2}
IMF type*	Shape of the Initial Mass Function	Sal (Kroupa)

*see Table 3.2

Table 3.2: IMF model parameters.

Label	Type	M_{low}	M_{up}	α	M_c	σ
Sal	Salpeter	1	500	-2.35		
logA	log-Normal	1	500		10	1.0
logE	log-Normal	1	500		60	1.0

as the main focus of this work is Pop. III stars. However, the impact of the first accreting BHs on the formation of the supermassive black holes and radiative backgrounds might be important even at high-redshift (Ventura et al. 2023).

3.2.7. *Pop. III luminosity*

In order to investigate the observability of the first Pop. III galaxies we implement spectral energy distributions (SED) for Pop. III stars. We use SEDs from Raiter et al. (2010) that have been computed for the IMFs listed in Table 3.2 assuming that star formation occurs in an instantaneous burst (see *instantaneous burst* in Raiter et al. 2010). These SEDs also include the nebular continuum emission and the UV ionizing properties. We used the latter to compute the number of UV ionizing photons per baryon n_b^{γ} for each IMF provided. To compute the luminosity of galaxies at a specific wavelength λ, we used the model introduced by Qiu et al. (2019) (see also Mutch et al. 2023), and we extended it to Pop. III galaxies. Having the Pop. III SEDs, we can compute the luminosity of a Pop. III galaxy at time t as:

$$L_{\lambda}(t) = \int_0^t \psi(t-\tau) S_{\lambda}(\tau) T_{\lambda}(\tau) d\tau. \tag{3.17}$$

Here τ is the stellar age, $\psi(t-\tau)$ the stellar mass formed at $t-\tau$ with age between τ and $\tau + d\tau$, $S_{\lambda}(\tau)$ is the luminosity of a stellar population per unit mass and $T_{\lambda}(\tau)$ is

the transmission function of the interstellar medium. For the latter term, we refer the reader to Qiu et al. (2019) while S_λ for each Pop. III IMF has been taken from Raiter et al. (2010) as discussed above. This calculation is nearly identical to Qiu et al. (2019), with the difference being that we do not have the metallicity dependence because Pop. III stars SEDs are defined with a zero metallicity. In this framework, we assume that the star formation occurs continuously throughout the snapshot. To compute $\psi(t-\tau)$, we take the stellar mass formed in that snapshot and average it over the entire duration of the snapshot. While this is a good approximation for Pop. II stars, Pop. III star formation is expected to occur in a single burst because of the feedback from Pop. III stars are likely to prevent continuous star formation. For this reason, we expanded the calculation of the luminosity of Pop. III galaxies assuming that new stars $\Delta m_\star$ form instantaneously at the time $t-\tau = t_0$. Hence, we can write $\psi(t-\tau) = \Delta m_\star \delta(t_0)$ and Eq. 3.17 simplifies to:

$$\begin{aligned} L_\lambda(t) &= \Delta m_\star \int_0^t d\tau \delta(t-t_0) S_\lambda(\tau) T_\lambda(\tau) \\ &= \Delta m_\star S_\lambda(t-t_0) T_\lambda(t-t_0). \end{aligned} \tag{3.18}$$

As we will discuss in Section 3.4, instantaneous (instead of continuous) Pop. III star formation has an impact on the estimated luminosity function of galaxies hosting Pop. III stars. This is because Pop. III stars have lifetimes that can be shorter than the duration of the snapshot (at $z = 10$ the snapshot will last 10 Myr, see Fig. 3.5). Hence, when we consider continuous star formation, we average the star formation over the entire snapshot, leading to lower luminosity with a higher duty cycle.

In order to account for instantaneous star formation, we assumed that a Pop. III star formation episode in a galaxy can occur at random $\Delta t \in [0, t_{\rm snap}]$ prior to the end of the snapshot.

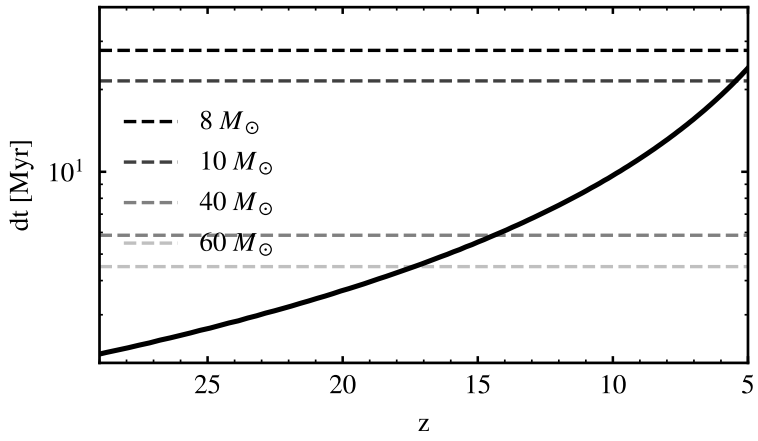

Figure 3.5: Duration of the snapshot dt in Myr as a function of redshift. Dashed lines correspond to the lifetime of a zero metallicity star of $8M_\odot$, $10M_\odot$, $40M_\odot$ and $60M_\odot$.

Instantaneous Pop. III star formation

Here we discuss how to evaluate the UV luminosity function of Pop. III galaxies assuming instantaneous star formation. Due to the stochasticity involved in the process of star formation, the burst might occur at any time within a snapshot (with a time duration of $t_{\rm snap}$) for a galaxy, resulting in different luminosities when observed. We refer to Δt as the time delay of the star formation burst happening relative to the end of our snapshot and draw its value from a random uniform distribution between zero and $t_{\rm snap}$. One can then evaluate the luminosity of this galaxy, repeat the exercise for all targets after assigning them different Δt, and calculate their probability distribution as a function of UV magnitude (i.e. the UV luminosity function, $\Phi(M_{\rm UV}, z)$). To achieve a more efficient computation, we instead sample Δt in fine steps of $\Delta t_i = [0.01, 0.5, 1.0, 1.5, ..., \Delta t_N]$ Myr with the last sample bracketing the snapshot length as $\Delta t_N \leq t_{\rm snap} < \Delta t_N + 0.5$Myr. Then we calculate the UV magnitudes of each galaxy for given Δt_i and evaluate the corresponding luminosity function at the condition of fixed Δt, $\Phi((M_{\rm UV}, z)|\Delta t_i)$. Finally, the luminosity function is obtained by summing all conditional probability distributions as

$$\Phi(M_{\rm UV}, z) = \sum_{\Delta t_i = 0.01}^{\Delta t_N} \Phi((M_{\rm UV}, z)|\Delta t_i) \times P(\Delta t_i). \tag{3.19}$$

Note that the probability of each conditional luminosity function is simply

$$P(\Delta t_i) = \begin{cases} \Delta t_i / t_{\rm snap} \text{ when i = 1,} \\ (\Delta t_i - \Delta t_{i-1})/t_{\rm snap} \text{ when 1 < i < N,} \\ (\Delta t_i - t_{\rm snap})/t_{\rm snap} \text{ when i = N.} \end{cases} \tag{3.20}$$

3.3. Global evolution of Pop. III stars

To explore the Pop. III contributions to the cosmic star formation history, we ran two simulations on the L10 box, one with all the updates described in Section 3.2 adopting the fiducial parameters (see Table 3.1 and one without the new physics that we labelled as "NoMini"). Given that there are no observational constraints on Pop. III, the choice of a fiducial model is arbitrary. The one adopted in this work has both a low star formation efficiency and a Salpeter-like IMF, which will result in a relatively small global impact of Pop. III star formation compared to Pop. II.

In Figure 3.6 we show the stellar mass function (SMF) at different redshifts accounting for all (black), only Pop. III dominated (cyan), and only Pop. II dominated (red) galaxies. We classified a galaxy as Pop. III or Pop. II dominated based on which population is brighter in the UV band. Thin (thick) lines are computed from the fiducial (NoMini) model. The total SMF has two components, separated by their stellar types. In this fiducial model, as Pop. III SFE is 10 times lower than Pop. II, we see a resulting bimodality (which we will further expand discussion in Sec 3.2.1). As shown in the upper panels, the new updates on meraxes mostly affect the lower end of the SMF with a larger impact at high-z. This reflects the star formation in mini-halos (we are now considering molecular cooling), which is dominant at $z \geq 15$ before the Lyman-Werner background becomes strong enough to photodissociate all the molecular hydrogen.

The low mass of Pop. III systems is mainly a consequence of both the shorter lifetimes of Pop. III stars (given their larger mass) and the lower SF efficiency, but also suggests that most of the Pop. III star formation must occur in mini-halos. In order to investigate this, we checked which halos form Pop. III and Pop. II stars. In Fig. 3.7, we show the halo mass function for Pop. III (cyan line) and Pop. II (red line) star-forming halos at $z = 20, 15, 10$

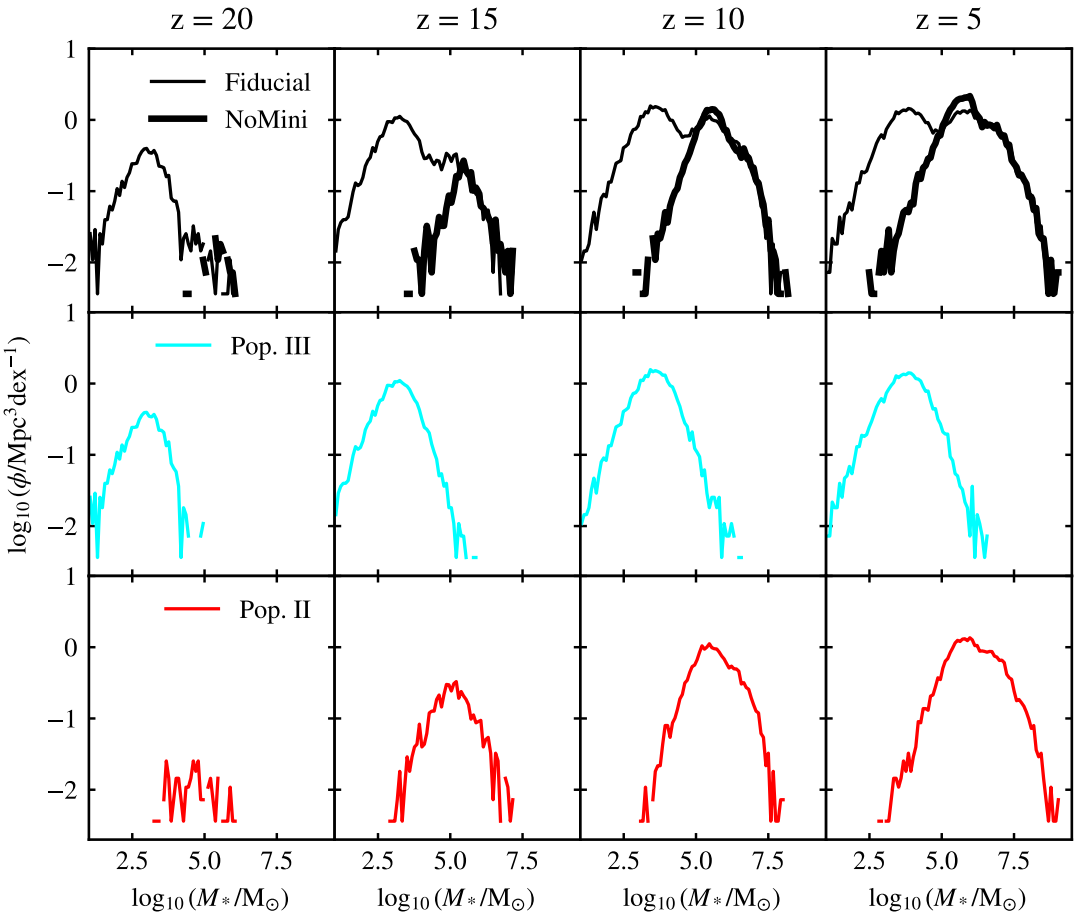

Figure 3.6: SMF at z = 20, 15, 10 and 5 for all stars (upper row), Pop. III stars (middle row) and Pop. II (lower row) using the fiducial model (Table 3.1) and the NoMini model (thick line).

and 5. The dashed line corresponds to the limit of atomic cooling ($T_{\rm vir} = 10^4$K). Given the small size of the box, we have only a few atomic cooling halos at $z \sim 20$, so all star-forming systems are mini-halos (and are mostly Pop. III). At lower redshift, the peak of the distribution shifts to higher masses (by $z = 10$ most of the stars form in atomic cooling halos except for some low mass halos that are undergoing a merger event) and the impact of Pop. II increases. Finally, Fig. 3.7 shows that Pop. III stars mostly form in mini-halos (except at $z = 5$ when the radiative feedback has suppressed both the gas infall and cooling in mini-halos). This is because the more massive halos are more likely to have already experienced star formation and so will be internally chemically enriched.

In Figure 3.8 we show the total star formation rate density (SFRD) as a function of

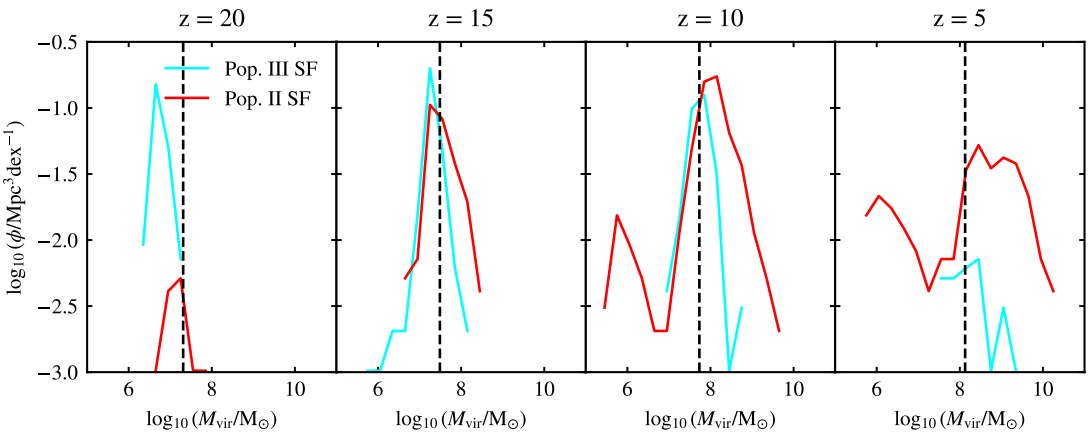

Figure 3.7: Halo mass function at z = 20, 15, 10 and 5 of Pop. III and Pop. II hosting systems. The dashed line corresponds to the $T_{\rm vir} = 10^4$ K that defines the atomic cooling limit.

redshift for both the fiducial and the NoMini model. In the case of the fiducial model, we also show the Pop. III (Pop. II) contribution in the upper (lower) panel. Mini-halos have an appreciable impact on the SFRD only up to $z \geq 20$, while at lower redshift, most star formation occurs in atomic cooling halos (at $z < 15$, the total SFRD in the fiducial and NoMini model are superimposed). We see that accounting for Pop. III star formation in mini-halos is crucial during the Cosmic Dawn because Pop. III stars dominate the global star formation history at $z \geq 20$ and are still relevant up to $z = 18$. As we can see in the lower panel, the Pop. III SFRD flattens at $z \sim 18$ and starts to decrease at $z \sim 10$. The early flattening occurs due to the build-up of the Lyman-Werner background that affects Pop. III star formation in minihalos. The sharp drop at $z \leq 10$ is mostly caused by the photoionizing feedback from reionization that also affects the atomic cooling halos. The feedback from reionization also mildly affects Pop. II as can be seen from the flattening of the red line at $z \sim 8$ in the upper panel¶

¶Given the small size of the box, the feedback from reionization it is slightly overestimated as we *(i)* are missing the most massive systems that would not be affected by the photo-ionizing feedback and *(ii)* the box gets completely ionized at $z \sim 6.9$ which is much earlier than what suggested by the latest Lyman-α forest measurements (e.g. Qin et al., 2021a; Bosman et al., 2022).

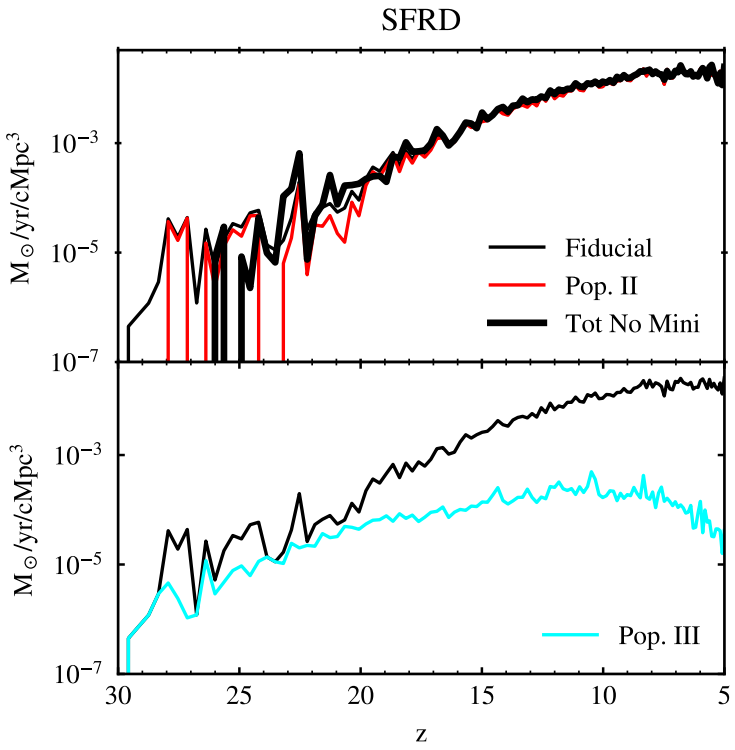

Figure 3.8: SFRD vs redshift for all stars (black line), Pop. III (cyan) and Pop. II (red) using the fiducial model (thin line) and the NoMini model (thick line).

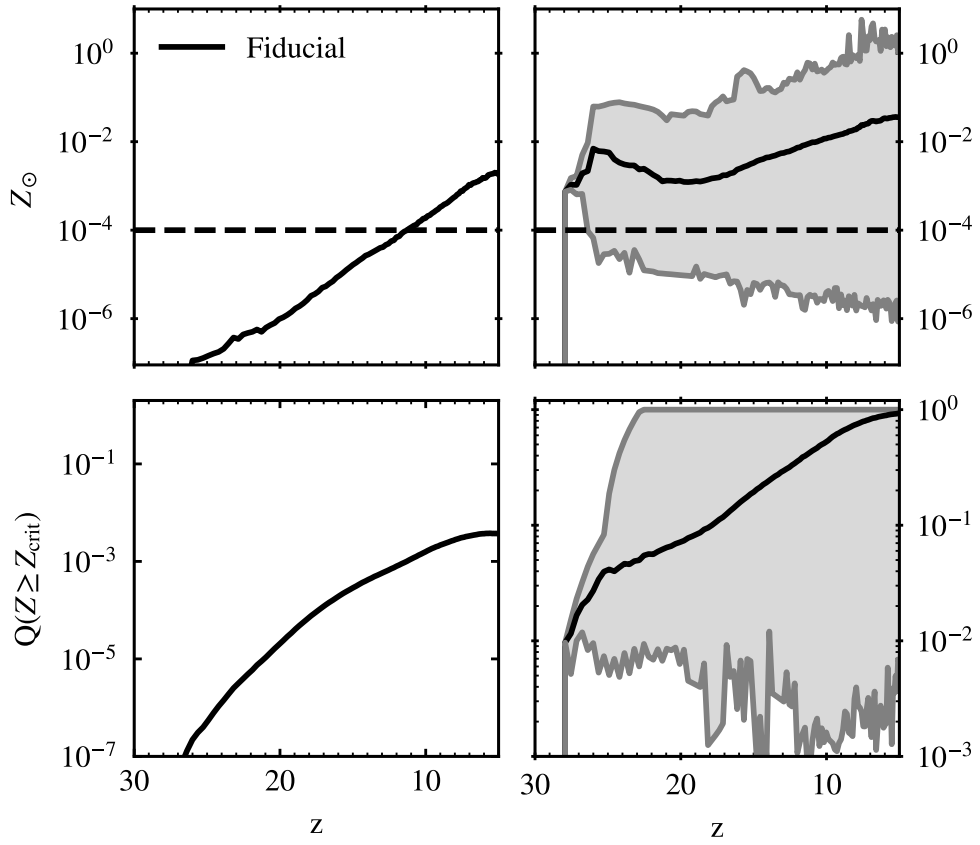

Figure 3.9: **top:** Average metallicity of the IGM (in solar units) vs redshift highlighting $Z_{\rm crit}$ for the Pop. III/II transition. **bottom:** fraction of the volume with a metallicity $Z \geq Z_{\rm crit}$ vs redshift. The left panels show these quantities averaged through the entire box, while the right panels consider only those cells with at least one metal bubble in them. Shaded regions in the right panels highlight the minimum and the maximum value (see text).

3.3.1. Chemical enrichment of the IGM

Compared to reionization, the chemical enrichment of the IGM is a much slower process due to the lower velocity of the expansion of the metal bubbles. As already found in previous works (e.g. Visbal et al., 2020; Yamaguchi et al., 2023), the impact of external metal enrichment is subdominant compared to internal metal enrichment. However, external enrichment might still be important for low-mass halos that do not form stars until $z \sim 10$.

The top left panel of Fig. 3.9 shows the redshift evolution of the average metallicity of the box (in solar units) computed using Eq. 3.9 and averaging through all 128^3 pix-

els. As expected, the average metallicity increases monotonically. It crosses the critical value at $z \sim 11$ and at the end of the simulation is $\sim 5 \times 10^{-3} Z_{\odot}$. The redshift evolution of $Z_{\rm IGM}$ is in very good agreement with Yamaguchi et al. (2023), especially for their "bursty" models, which is the one that most closely resembles the star formation in MERAXES. However, the average metallicity of the IGM does not completely inform us of the average metallicity of the galaxies since, when averaging through the entire box, we are considering voids that have no galaxies and hence zero IGM metallicity. For this reason, in the top right panel, we computed the black solid line, averaging only through cells that have at least one metal bubble (meaning that there must be at least one galaxy that formed stars). The shaded region shows the scatter in the metallicity of these cells from the highest to the lowest metallicity. The average metallicity, in this case, is much higher, and it is always above the critical value. This suggests that once the first galaxies form, the ejection of metals from Pop. III is quite effective in the nearby regions, allowing a fast Pop. III/II transition in those cells where star formation already occurred (and the galaxies are internally enriched). The lower panels instead show the fraction of the IGM that reached the critical metallicity (or equivalently, the metal filling factor $Q(Z \geq Z_{\rm crit})$). Considering the entire box (left panel), less than 1% of the volume gets enriched above $Z_{\rm crit}$ by $z \sim 5$. This result is fairly consistent with Visbal et al. (2020) and Yamaguchi et al. (2023) ($\sim 1\%$ by $z = 6$). These small differences are likely due to differences in the star formation models and in the choice of parameters, such as the star formation efficiency. If we focus only on the regions with at least one galaxy that formed stars, we find larger filling factors, and by the end of the simulation, those pixels are all completely enriched. This final result reflects our choice of pixel size that is designed to be similar to the average volume of the metal bubble at $z \sim 5$.

Finally, in Fig. 3.10, we show the halo mass function for the externally (black line) and internally (grey line) metal enriched halos at $z = 20, 15, 10$ and 5[‖]. While most halos get internally enriched by their own star formation, at $z = 5$ halos with virial masses $M_{\rm vir} \leq 10^{7.5} M_{\odot}$ get their metals mostly from a nearby supernova bubble. This picture reflects the fact that low-mass halos during reionization are not able to form stars

[‖]While physically a halo could be both internally and externally enriched, here we are simplifying assuming that a halo is either internally or externally enriched.

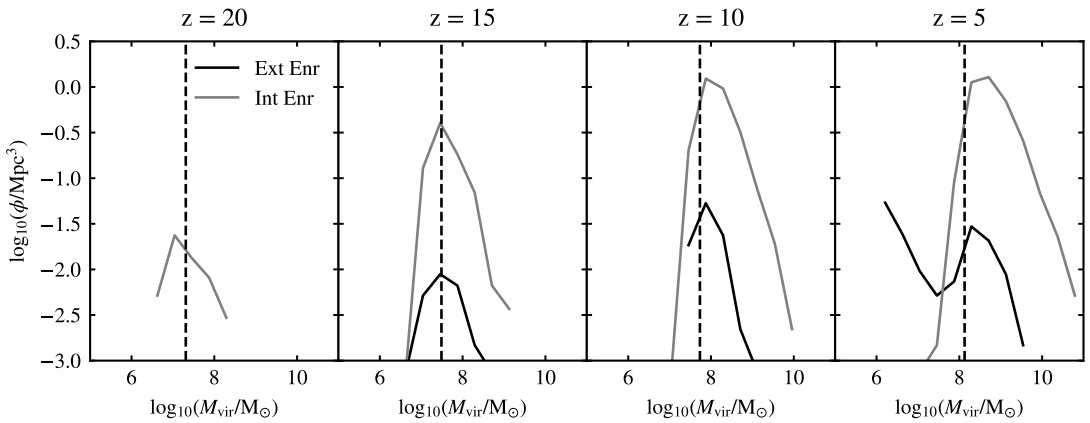

Figure 3.10: Halo mass function at z = 20, 15, 10 and 5 of Pop external (black) and internal (grey) metal enriched halos. The dashed line corresponds to the $T_{\rm vir} = 10^4$ K that defines the atomic cooling limit.

because of the LW and photo-ionizing feedback. Hence, those objects can be chemically enriched only from an external source.

In conclusion, when looking at the global evolution of star formation, the effect of the external metal enrichment is quite negligible as it is important only for low-mass halos at low redshift that will hardly form stars due to the radiative feedback effects. We verified this by running a simulation without external metal enrichment (a halo can only get enriched by its own star formation). We plot in Fig. 3.11 the total, Pop. III and Pop. II SFRD (dashed lines) compared to the fiducial model (solid lines). There are no appreciable differences between the two models except at $z \leq 8$ when the dashed line is slightly larger (about 0.1 dex difference).

3.3.2. Pop. III star formation parameters

The results in previous sections were obtained adopting quite conservative assumptions for Pop. III stars given the very low SF efficiency and the Salpeter-like IMF (although with $M_{\rm min} = 1 M_\odot$). In the following sections, we explore the four main free parameters that regulate Pop. III star formation in MERAXES listed in Table 3.1: the Pop. III star formation efficient $\alpha_{\rm SF,III}$, the critical metallicity for Pop.III/II transition $Z_{\rm crit}$, the critical surface density of cold gas for Pop. III star formation to occur $\Sigma_{\rm norm,III}$ and the IMF.

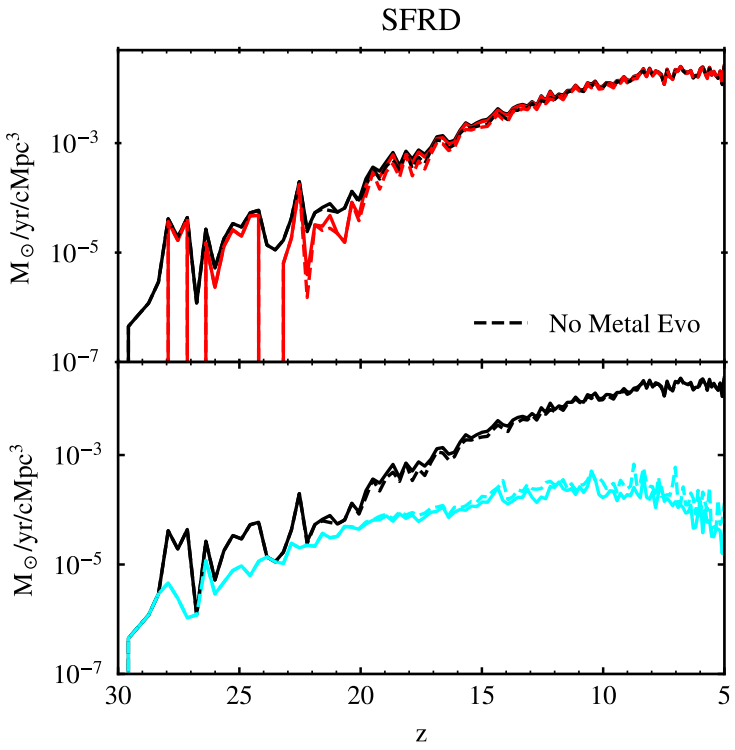

Figure 3.11: As Fig. 3.8 for the fiducial model (solid lines) and turning off the external metal enrichment (dashed lines).

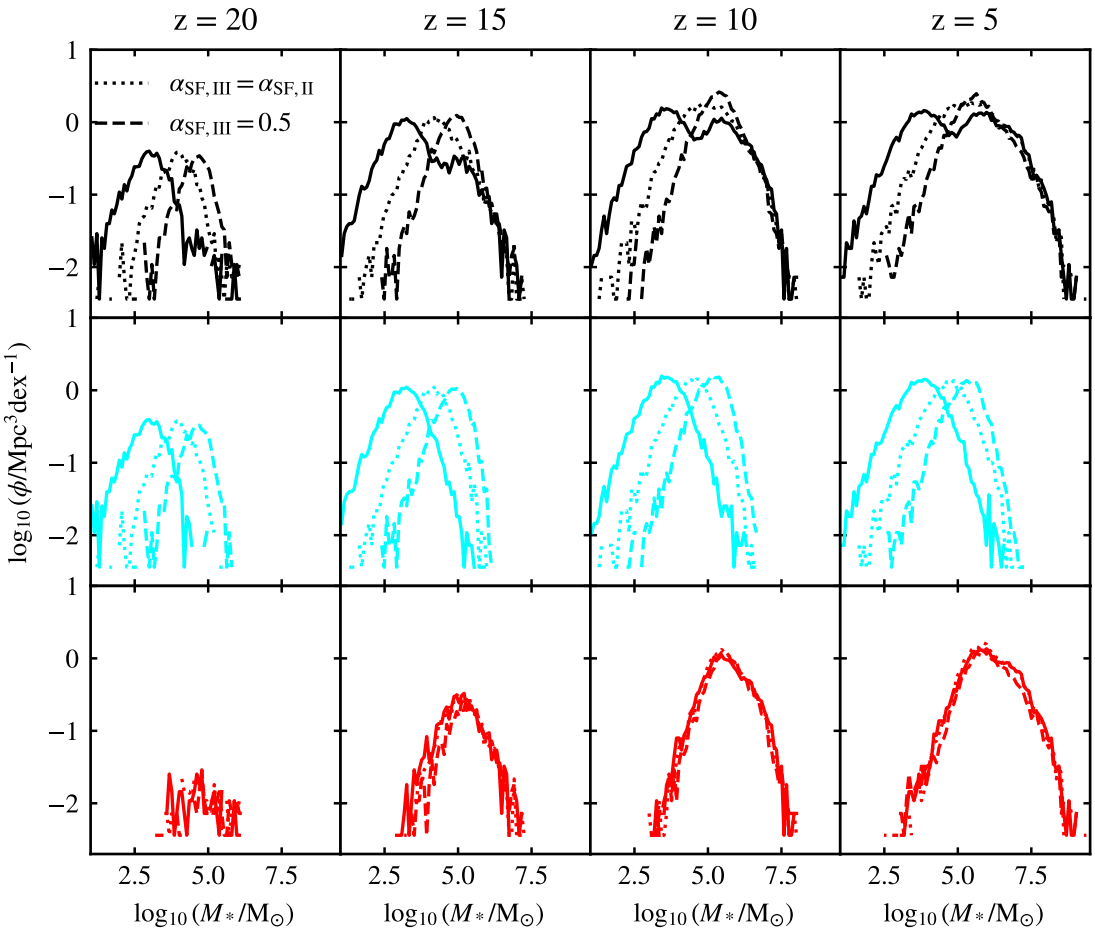

Figure 3.12: As Fig. 3.6 using the fiducial model (solid), $\alpha_{SF,III} = \alpha_{SF,II}$ (dotted) and $\alpha_{SF,III} = 0.5$ (dashed).

Pop. III SF efficiency

The star formation efficiency determines the conversion of the cold gas into stars and is the free parameter with the largest impact on the Pop. III global SFRD and SMF. This parameter is largely unconstrained, with some simulations supporting very low values (10^{-4}–10^{-3} Skinner & Wise 2020) and others suggesting higher values (Fukushima et al. 2020). We ran two simulations keeping all the Pop. III free parameters unchanged except for $\alpha_{SF,III}$, which we boosted by one order of magnitude (to the same value we use for Pop. II $\alpha_{SF} = 0.08$) and to a very high value ($\alpha_{SF} = 0.5$).

As shown in Fig. 3.12, Pop. III galaxies become more massive as α_{SF} increases, erasing the "double peak" feature in the total SMF. For the model with $\alpha_{SF,III} = \alpha_{SF,II}$, the peak

of the Pop. III SMF is still shifted to the left by half dex compared to the Pop. II. This is because, despite having the same star formation efficiency, Pop. III galaxies mostly form in mini-halos. For $\alpha_{\rm SF,III} = 0.5$, the peak of the Pop. III and Pop. II SMF is at the same mass value ($10^5 - 10^6 M_\odot$ at $z \sim 15 - 5$) with the only difference being the larger variance for Pop. II galaxies. Increasing the Pop. III SF efficiency does not affect the Pop. II SMF (except for small variations at $z = 5$) meaning that the mechanical feedback does not change significantly.

The star formation efficiency also regulates the Pop. III/II transition as it directly correlates with the SFRD. Looking at the SFRD in the three different models (Fig. 3.13) we see that for $\alpha_{\rm SF,III} = 0.5$, the SFRD is dominated by Pop. III up to $z \sim 15$ compared to the fiducial model where Pop. II SF becomes larger than Pop. III at $z > 20$. The Pop. II SFRD does not significantly change between the three models, and so the change in the Pop. III SFRD also affects the total SFRD (the dashed line is almost one order of magnitude higher than the solid one). All the models converge at $z \sim 13$ when even with the highest $\alpha_{\rm SF,III}$ the total SFRD is entirely dominated by the Pop. II contributions.

Critical metallicity

The critical metallicity defines the metallicity at which there is a change in the IMF (metal-free gas clouds have inefficient cooling that leads to less fragmentation and higher masses Chiaki & Yoshida 2022). There is currently no consensus on the value of $Z_{\rm crit}$, with two competing models that assume the fragmentation driven by either the carbon and oxygen line (e.g. Chon et al., 2021) or the dust cooling (e.g. Schneider et al., 2012; Chiaki & Yoshida, 2022). The first class of models determine a $Z_{\rm crit} \sim 10^{-2} - 10^{-3} Z_\odot$ while the seconds give a lower value ($\sim 10^{-6} Z_\odot$). Some studies also argue that the value of $Z_{\rm crit}$ evolves with redshift due to the effect of the CMB (Chon et al. 2022). Following simulations in the literature (Schneider et al. 2006; Visbal et al. 2020), in this work we adopted an intermediate value $Z_{\rm crit} = 10^{-4} Z_\odot$ as the fiducial value, hereafter we will also show results for the two extreme values of $10^{-2} Z_\odot$ and $10^{-6} Z_\odot$.

The SMF between the fiducial model and $\rm Z_{crit} = 10^{-6}\ Z_\odot$ does not change. This is because, as we saw in the top right panel of Fig. 3.9, in the overdense regions where

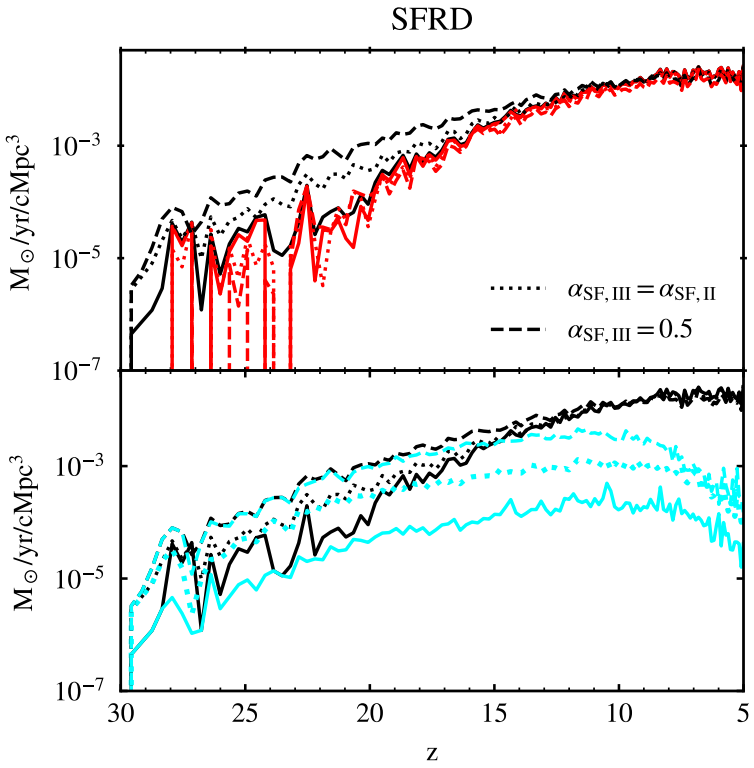

Figure 3.13: As Fig. 3.8 using the fiducial model (solid), $\alpha_{\rm SF,III} = \alpha_{\rm SF,II}$ (dotted) and $\alpha_{\rm SF,III} = 0.5$ (dashed).

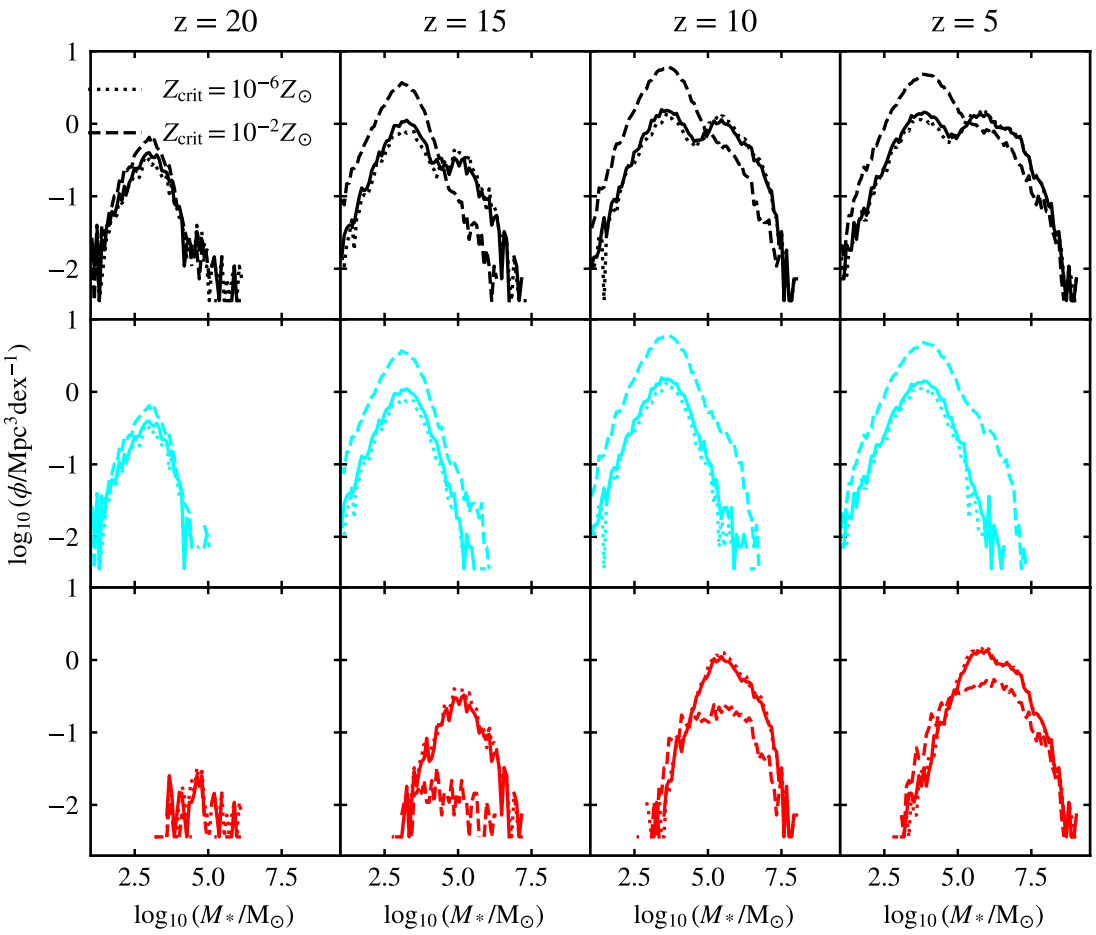

Figure 3.14: As Fig. 3.6 using the fiducial model (solid), $Z_{\rm crit} = 10^{-6} Z_\odot$ (dotted) and $10^{-2} Z_\odot$ (dashed).

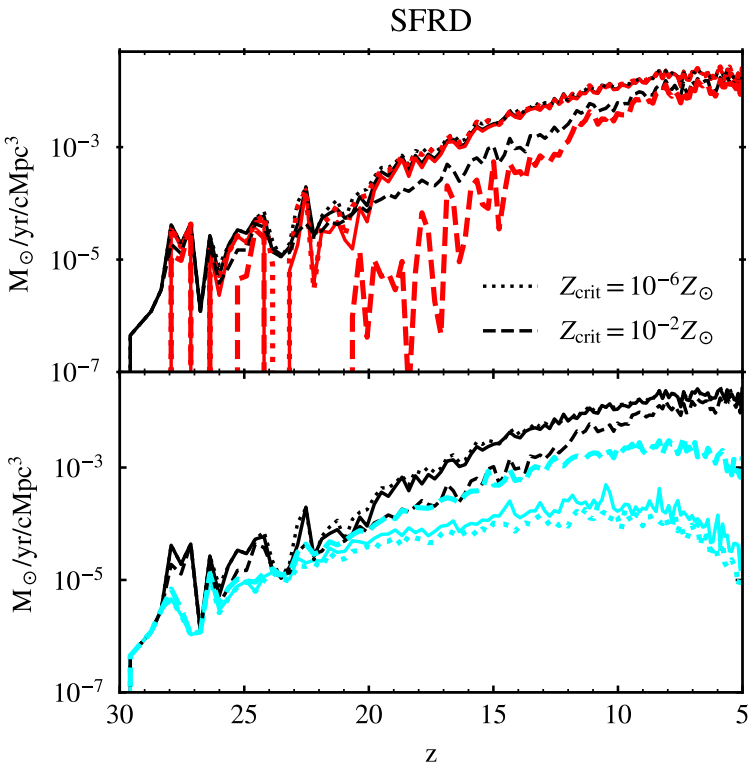

Figure 3.15: As Fig. 3.8 using the fiducial model (solid), $Z_{\rm crit} = 10^{-6} Z_\odot$ (dotted) and $10^{-2} Z_\odot$ (dashed).

there is star formation, the metallicity becomes larger than $10^{-4} Z_\odot$ very quickly so that changing $Z_{\rm crit}$ to $10^{-6} Z_\odot$ does not further accelerate the Pop. III/II transition. However, considering a higher value changes the total SMF as we end up with many more Pop. III stars. As shown in Fig. 3.14, in the Pop. III SMF in this case, many of the previously identified as Pop. II galaxies are now Pop. III galaxies across the entire mass range. The high-mass tail of Pop. III SMF extends up to $10^{7.5} M_\odot$ at $z = 5$ when $Z_{\rm crit} = 10^{-2} Z_\odot$, while the Pop. II systems are less massive as they start to form later and so have less time to build up their mass. The combined effect of Pop. III and Pop. II makes the total SMF computed from the simulation with $Z_{\rm crit} = 10^{-2} Z_\odot$ single peaked as the high-mass peak coming from Pop. II stars are washed out even at $z = 5$ so that the total SMF peaks at $M_\star \sim 10^4 M_\odot$ at $z = 10 - 5$ with a high-mass tail that extends up to $10^9 M_\odot$.

The critical metallicity also has a strong impact on the evolution of the SFRD (see Fig. 3.15) as it affects both the internal and external enrichment. While decreasing the value of $Z_{\rm crit}$ from the fiducial value only mildly decreases the Pop. III SFRD without altering

the total result, choosing $Z_{crit} = 10^{-2} Z_{\odot}$ strongly changes the SFRD history at $z \leq 18$. The Pop. III SFRD increases by 1-2 orders of magnitude while the Pop. II decreases by the same amount. It also starts to increase steadily only from $z \sim 18$. Increasing the Pop. III star formation and simultaneously decreasing the Pop. II impacts on the total SFRD. Since Pop. III stars form less efficiently ($\alpha_{SF,III} = 0.1 \times \alpha_{SF,II}$) we predict a lower total SFRD compared to the fiducial model (and in this case, the two models do not converge until the very end of the simulation). Overall the critical metallicity heavily impacts both the SFRD and SMF during the Cosmic Dawn and the Epoch of Reionization and affects when the universe transitions from being Pop. III dominated Pop. II.

Critical surface density

In order to trigger the star formation in a galaxy, our model requires the gas density in the disk to be above a certain threshold. This result has been obtained in the observational results of Kennicutt (1998); Kennicutt & De Los Reyes (2021) and theoretically motivated by Kauffmann (1996); however, the value of this parameter is highly uncertain, especially at high-z as it depends on the structure of the disk (e.g. thickness, turbulence etc.). We decided to duplicate this free parameter so that we have one for Pop. III and one for Pop. II. While keeping the Pop. II parameter fixed, we explore the extreme case of $\Sigma_{norm,III} = 0$, which is equivalent to assuming that Pop. III stars start to form as soon as the cooling of the gas begins, and all cold gas is available to form Pop. III stars (in proportion to the star formation efficiency). This choice results in a larger abundance of low-mass Pop. III systems at high-z (the largest difference between the cyan dashed and solid line in Fig. 3.16 are at $z = 20$ and 15).

However, since the main changes in the Pop. III SF are in low-mass halos, setting $\Sigma_{norm,III} = 0$ does not significantly change the SFRD history (see Fig. 3.17 where the cyan dashed line is only slightly lower than the fiducial model).

Overall, this free parameter is the one with the smallest impact on the star formation history, as it only impacts the low-end of the stellar mass function at high-z for which there are no observational constraints.

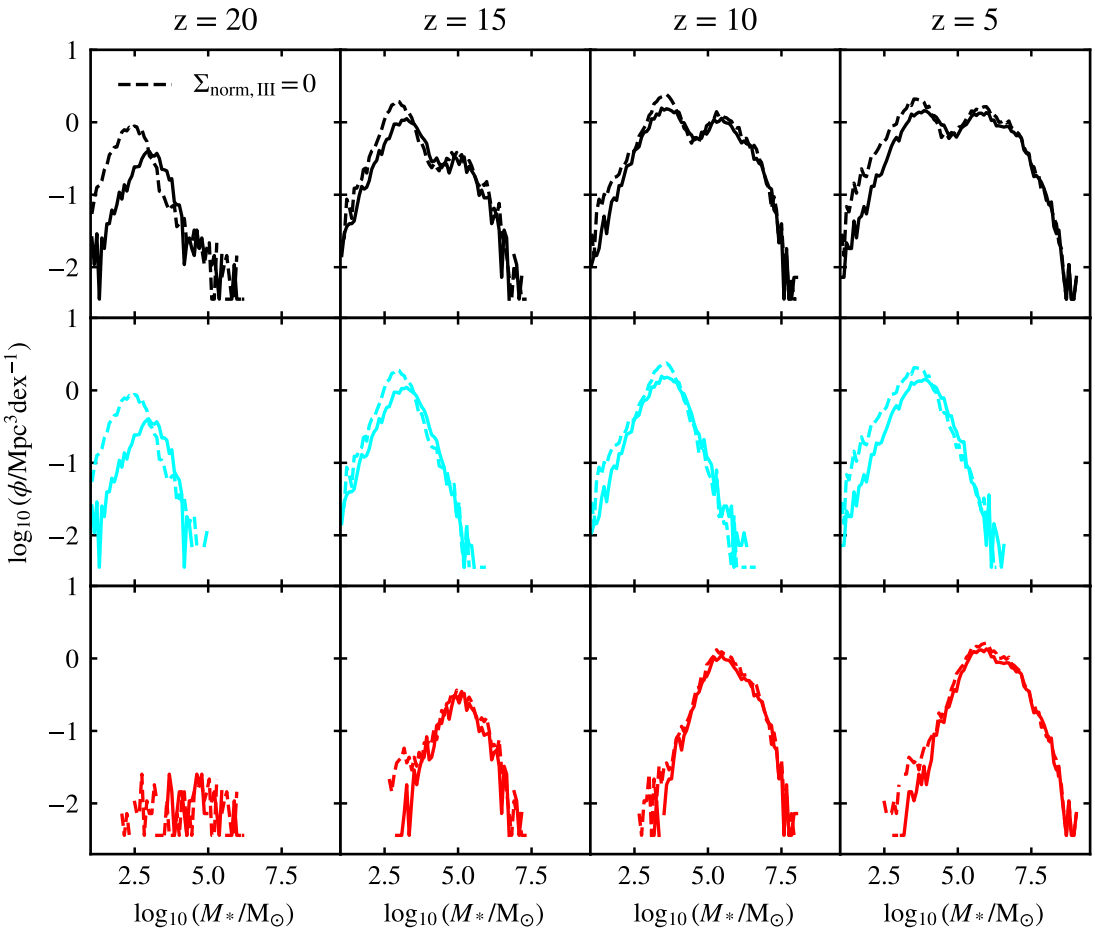

Figure 3.16: As Fig. 3.6 using the fiducial model (solid) and $\Sigma_{\mathrm{norm,III}} = 0$ (dashed).

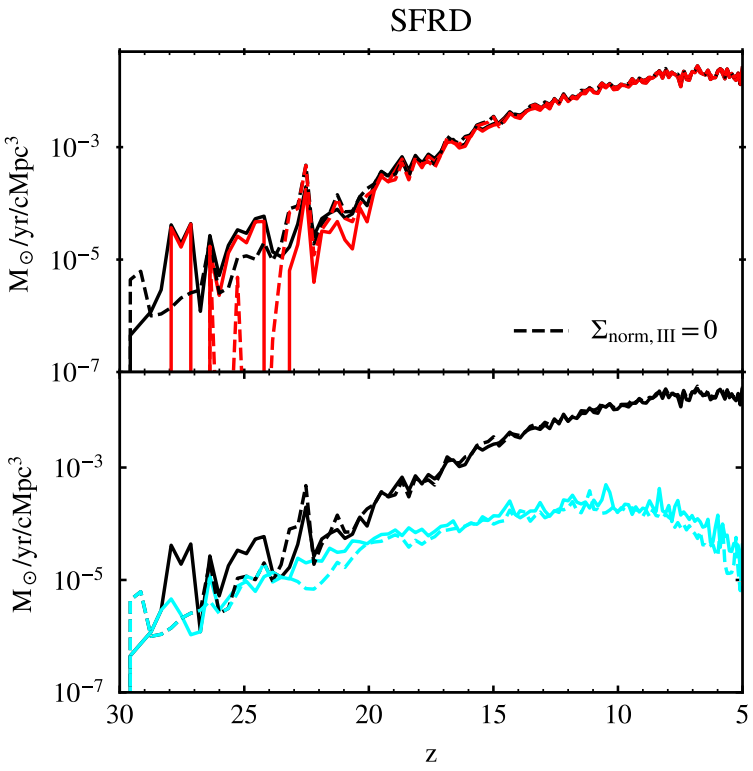

Figure 3.17: As Fig. 3.8 using the fiducial model (solid) and $\Sigma_{\rm norm,III} = 0$ (dashed).

IMF

The last parameter we explore is the IMF of Pop. III stars. Our fiducial model is quite similar to the Pop. II IMF as we assume a Salpeter IMF that favours the formation of low-mass stars. The only difference is that we take larger lower and upper limits (1 $M_\odot$ and 500 $M_\odot$). We consider two log-normal IMFs labelled logA and logE as in Tumlinson (2006) with the parameters summarized in Table 3.2. For these IMFs we have spectral energy distributions (from Raiter et al. 2010) which will be used in Section 3.4). The IMF logA is centred at $M = 10M_\odot$, which enhances the probability of a Pop. III stars ending its life as a core-collapse SN. logE is centred at even a higher mass ($M = 60M_\odot$), so we expect most of the stars with very short lifetimes to end their lives by collapsing into a black hole without any supernova explosion. Compared to the Salpeter IMF, both log-normal IMFs do not have many low mass stars ($M < 8M_\odot$).

Decreasing the lifetime of Pop. III stars make the Pop. III SMF in Fig. 3.18 shift to lower masses, increasing the separation between the two peaks of the total SMF (the

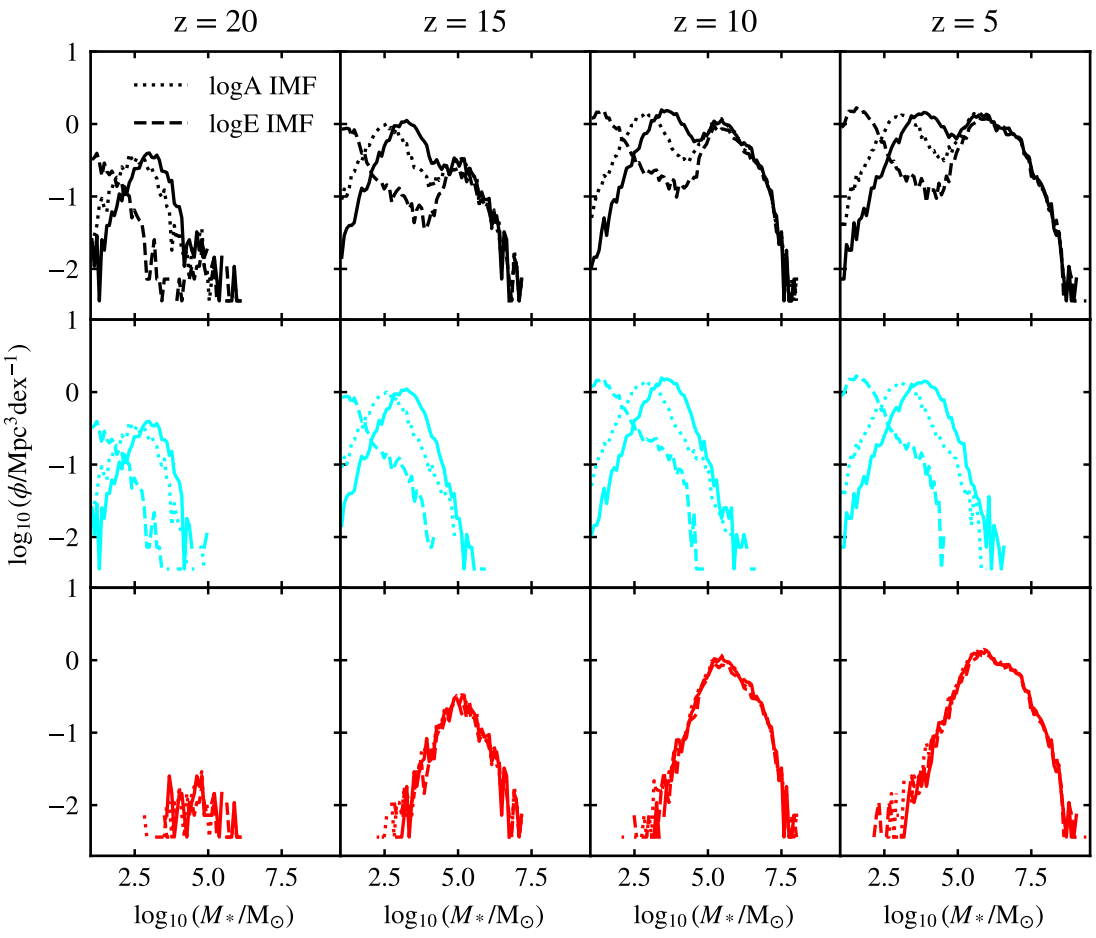

Figure 3.18: As Fig. 3.6 using the fiducial model (solid), the logA IMF (dotted) and the logE IMF (dashed).

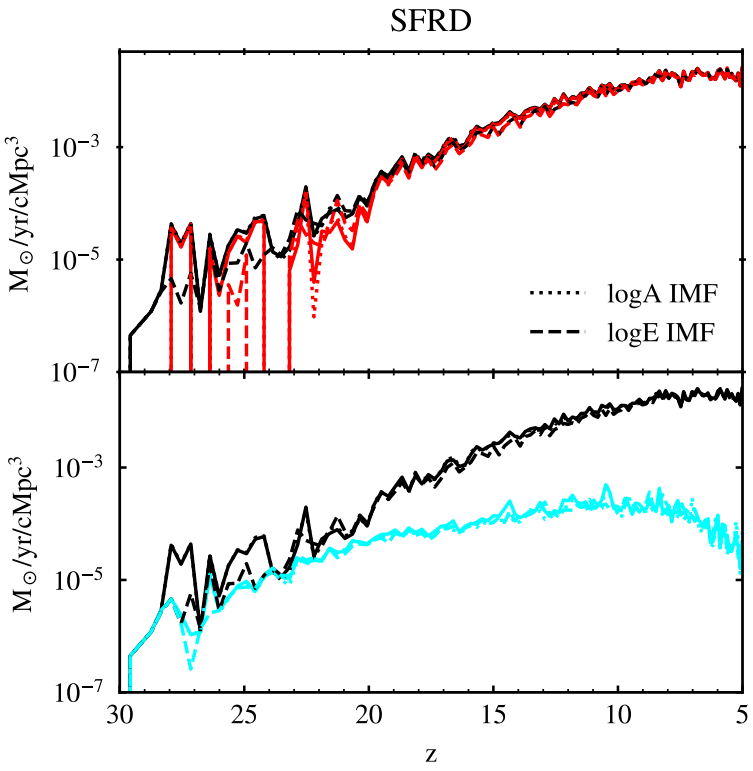

Figure 3.19: As Fig. 3.8 using the fiducial model (solid), the logA IMF (dotted) and the logE IMF (dashed).

effect of changing the IMF towards higher masses is the opposite of increasing the SF efficiency). The difference between the fiducial model and one adopting the logA IMF is less than one dex. However, in the logE IMF model, most of the stars die in the same snapshot in which they form (the lifetime of a $60M_\odot$ star is ~ 4.5 Myr, which at $z < 15$ is less than the time separation between two consecutive snapshots in MERAXES, see also Fig. 3.5). This effect strongly prevents the build-up of Pop. III systems, and in Fig. 3.18, we can see that the most massive Pop. III galaxies at $z = 5$ have $M \sim 10^5 M_\odot$. There are no differences in the Pop. II SMF with different IMFs.

In difference from the SF efficiency, the IMF mostly affects the stellar mass function. This is because the main change is with respect to the lifetime of Pop. III stars. In Fig. 3.19 we see that there are no significant differences in the SFRD from adopting different IMFs, except for the first few snapshots of our simulation where the star formation is mildly reduced in the logE model. This result comes from the stronger feedback typical of the more top-heavy IMF (a larger number of massive stars implies more supernovae),

and it has a stronger impact at $z \geq 24$ when Pop. III star formation is dominating.

In conclusion, the global evolution of Pop. III stars are strongly dependent on the star formation efficiency because high $\epsilon_{\rm SF,III}$ increases both the SMF and the SFRD. The evolution is also dependent on the IMF adopted (although the IMF affects only the SMF). The critical metallicity has an impact only if we consider a high value, and it mostly affects the self-enrichment as most of the galaxies in our simulation get their metals from their own star formation rather than from an external metal bubble. The critical surface density instead has only a small impact on the Pop. III star formation history and it is restricted to small mass halos and high-z.

3.4. Pop. III observability with JWST

Unconstrained Pop. III free parameters in our model have an impact on the redshift evolution of the SMF and SFRD. However, our model predicts a consistent number density of Pop. III dominated systems with stellar masses between $10^3 - 10^5$ $M_\odot$. Here we will explore the UV luminosity of these systems using the model described in Section 3.2.7 focusing on the luminosity functions at very high-z.

Given the same total stellar mass, Pop. III systems have larger luminosities compared to Pop. II galaxies, but shine for shorter times. This is demonstrated in figure 3.20 where we show the evolution in the first 10Myr of the SED of a Pop. III galaxy that forms $10^5 M_\odot$ Pop. III stars at z = 8 (top panels) and the absolute UV magnitude (bottom panels) at different times Δt since the star formation burst. Left, mid and right panels assume a Pop. III Salpeter, logA and logE IMF respectively. The black horizontal line corresponds to the magnitude computed assuming a continuous star formation throughout the snapshot. For reference, we also show the magnitude of a Pop. II galaxy forming the same amount of Pop. II stars (red dashed line). Firstly, we notice that Pop. III galaxies with continuous star formation and a log-normal IMF are one magnitude brighter than Pop. II galaxies with the same SFR (while there is no significant difference if Pop. III stars follow a Salpeter IMF). Once we focus on the instantaneous star formation model for Pop.

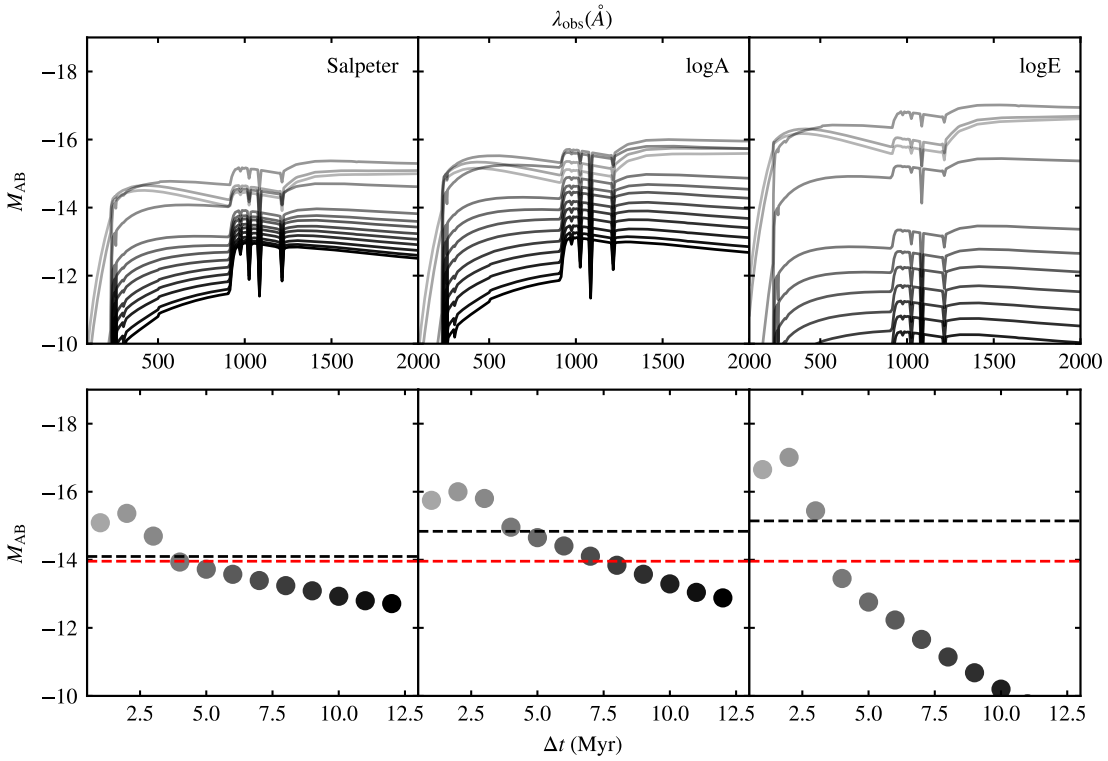

Figure 3.20: **top:** time evolution of the SED of the brightest Pop. III galaxy at $z = 8$ assuming a Salpeter (left), logA (mid), logE (right) IMF. Lighter lines assume a smaller Δt since the star formation burst. **bottom:** Absolute UV magnitude of the same galaxy as a function of Δt in Myr. The black (red) horizontal line shows the magnitude value of the galaxy assuming a Pop. III (Pop. II) continuous star formation.

III stars, the brightness of the galaxy can be boosted (or reduced) by several magnitudes depending on the time Δt following the burst at which we are observing the system (see also Trussler et al. 2023). Even when we consider a Salpeter IMF, the brightness of a Pop. III galaxy changes ~ 2 mags in ~ 10Myr. This change is more dramatic for the log-normal IMFs (especially for the logE IMF where in 10 Myr $\Delta M_{\rm AB} \simeq 7$ mags). The large difference between the instantaneous and continuous star formation models shown in Fig. 3.20 for a single Pop. III galaxy will reflect in the entire population and potentially lead to a higher number density of extremely bright Pop. III galaxies.
Fig. 3.21 shows the luminosity function (computed as described in 3.2.7). As a result of instantaneous Pop. III star formation, there are chances to observe these galaxies at a time when their luminosities are higher than what is given by the continuous scenario. This is reflected in Fig. 3.21 where we see the bright end of the solid cyan line shifting to higher luminosities. When looking at the total luminosity function we see a much significant Pop. III contribution to the number density of galaxies around $\rm M_{AB} \sim -16$ when assuming a LogE IMF for their SF.

Given their larger brightness, a population of Pop. III galaxies with a top-heavy IMF has been suggested as a possible explanation for the abundance of bright galaxies at $z > 10$ (see, e.g. Trinca et al. 2023; Yung et al. 2023 and Harikane et al. 2023). Without invoking any exotic physics or a revision of the standard ΛCDM model of cosmology, other possible explanations are a combination of increased star formation efficiencies at high-z and reduced feedback (Qin et al. 2023), bursty star formation (Sun et al. 2023), cosmic variance (Shen et al. 2023) and a modified ΛCDM power spectrum (Parashari & Laha 2023; Padmanabhan & Loeb 2023). Here, we show the predicted UV luminosity functions at $z = 16, 12, 11, 10, 9$ (we chose these values as the ones for which there are more JWST observations available). Results for different IMFs and different star formation efficiencies are summarized in Fig. 3.22 where all the other Pop. III parameters are taken as in the fiducial model. For all the models considered below, our total luminosity function agrees with early JWST observations at $z \leq 12$ (except for the points at $M_{\rm AB} < -19$ where we do not have galaxies in MERAXES).

With our fiducial parameters (dashed lines), both with the Salpeter and with the logA

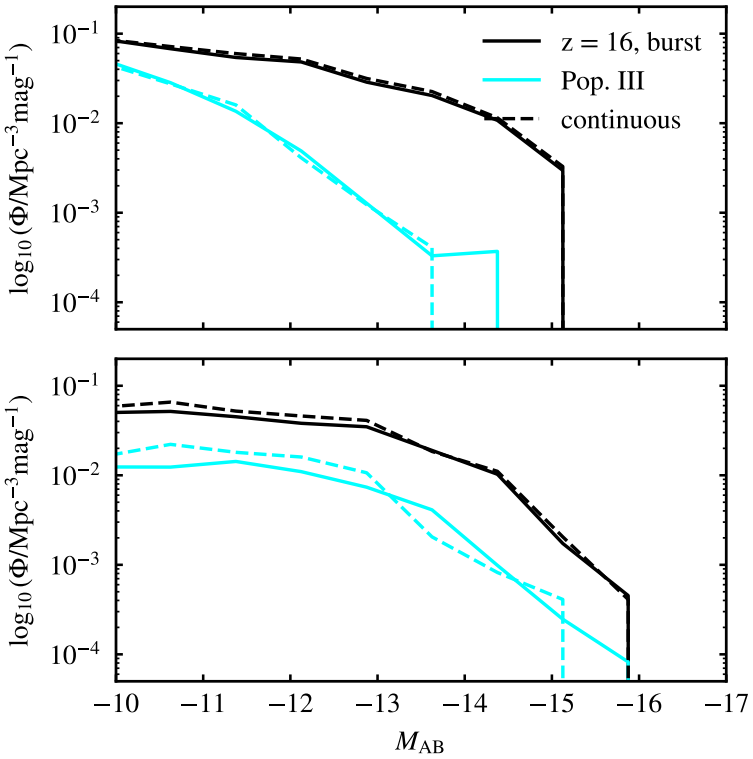

Figure 3.21: Total (black) and Pop.III (cyan) UV luminosity function at $z = 16$ assuming the Salpeter (top) and the logE (bottom) IMF. Solid lines are computed assuming that Pop. III stars form in a single burst, dashed lines take a continuous star formation model.

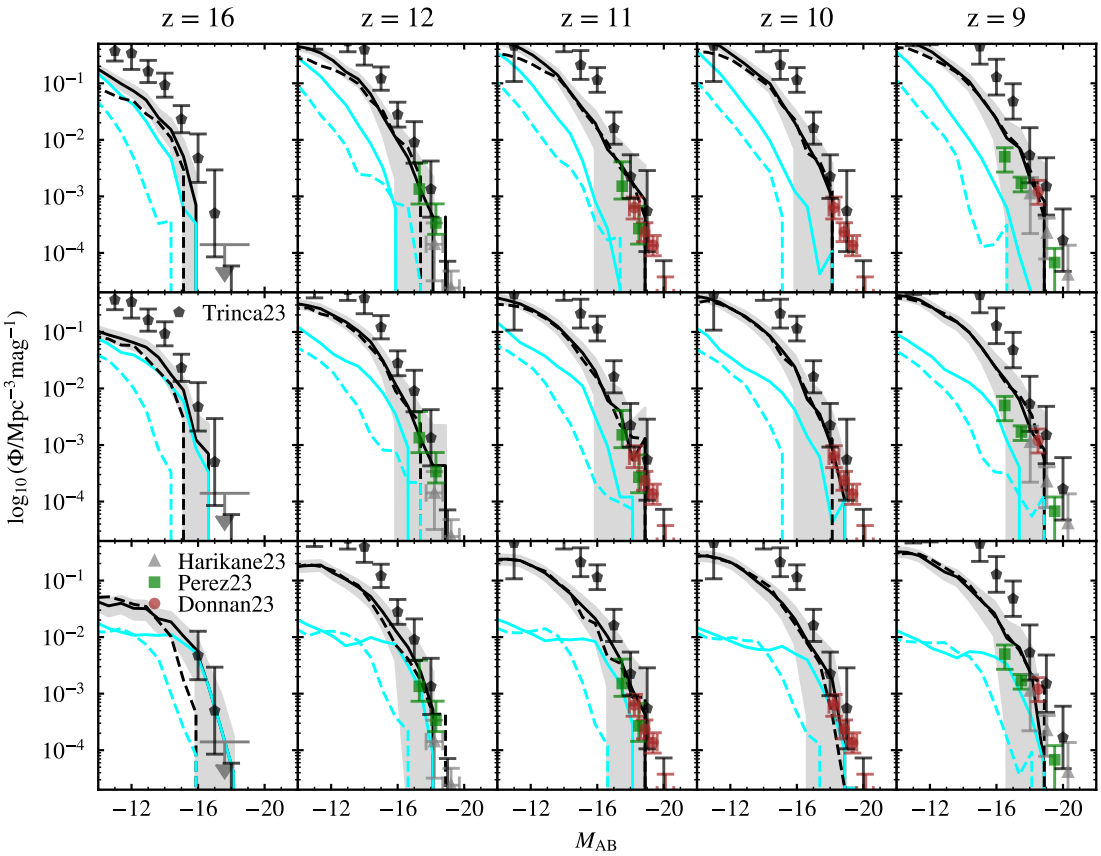

Figure 3.22: Total (black) and Pop. III dominated galaxies (cyan) UV LF at $z = 16, 12, 11, 10, 9$ (from left to right) for the Salpeter, logA and logE IMF (from top to bottom) and $\alpha_{\mathrm{SF,III}} = 0.08$ (solid), 0.008 (dashed). Uncertainties for the black solid line are shown with shaded regions (computed using the Poisson error). Data points highlight recent JWST results from Donnan et al. (2023); Harikane et al. (2023); Pérez-González et al. (2023) and the results from the simulation of Trinca et al. (2023).

IMF (upper and middle row), we find that Pop. III systems are not the brightest galaxies at the redshift considered ($M_{AB} \geq -14$). However, when we consider a log-normal IMF with a characteristic mass of $60M_{\odot}$ (lower row), Pop. III galaxies become significantly brighter (the cyan line approaches the black line) and at $z = 12$ and 16 when some of the brightest systems ($M_{AB} \sim -16$) are Pop. III dominated. Even though most of the Pop. III galaxies are still very faint (well below the sensitivity of JWST). This result may indicate that Pop. III dominated galaxies are present at $z > 12$.

This result becomes more robust when considering $\alpha_{SF,III} = \alpha_{SF,II}$ (solid lines). The bright end of the total and Pop. III dominated galaxy UVLF shifts of $1 - 2$ magnitudes (depending on the IMF) at $z = 16$ and 12. At $z \leq 11$, there is no or little difference in the total UVLF with different star formation efficiency even though Pop. III dominated galaxies are still ~ 1 mag brighter. Models with a Salpeter or a log-normal IMF centered at $10M_{\odot}$ predict that the bright end of the UVLF at $z = 16$ is impacted by Pop. III dominated systems while at $z \leq 12$ none or very few of the brightest galaxies are Pop. III dominated. Overall, the abundance of bright galaxies at $z \geq 12$ is better explained by the model with the logE Pop. III IMF and $\alpha_{SF,III} = \alpha_{SF,II} = 0.08$. For this model at $z \geq 12$ we find Pop. III dominated galaxies with $M_{AB} \simeq -18$ and at $z = 16$ all the brightest galaxies ($M_{AB} \leq -16$) are Pop. III dominated.

The results discussed above considered a star formation efficiency $\alpha_{SF,III} \geq 0.008$ which allows the formation of Pop. III stellar systems in MERAXES with masses up to $\sim 10^5 M_{\odot}$. These values are substantially higher than what predicted by some hydro-dynamical simulations (e.g. Xu et al., 2016; Sarmento & Scannapieco, 2022). This may suggest lower star formation efficiencies than what considered in this work making Pop. III galaxies much fainter and very unlikely to be observed. We compared our results with Trinca et al. (2023) (black pentagons in Fig. 3.22), and found a good agreement at $z \leq 12$ and $M_{AB} \lesssim -16.5$ for all the models considered. The main differences are that at $z = 9$, we do not have any galaxy with $M_{AB} \sim -20$, and their model has a steeper evolution predicting many more faint galaxies. At $z = 16$ only models with $\alpha_{SF,III} = 0.08$ and a log-normal IMF reproduce their results at $-14 \leq M_{AB} \leq -18$. Even though the total UVLF are similar, their Pop. III contribution is significantly lower, especially when compared to the models with $\alpha_{SF,III} = 0.08$ (their results predict that less than 10% of bright galaxies

at $z = 15 - 16$ host an active Pop. III stellar population). Given that the choice of Pop. III free parameters are similar (they also take $\alpha_{\rm SF,III} \sim 0.1$ and account for a critical surface density of the cold gas before forming Pop. III stars). The main differences in the model that can explain the different results are *(i)* the homogeneous feedback and *(ii)* the Pop. III luminosity calculation. In their model, both the radiative feedback and the chemical enrichment are homogeneous; this might overestimate the suppression of Pop. III systems at $z \sim 10 - 20$ (when the LW background is effective). Regarding the second point, our model accounts for the fact that a Pop. III galaxies might be observed immediately after they formed stars. As shown in Fig. 3.21, this enables us to boost the luminosity of some Pop. III dominated galaxies by several magnitudes. Without accounting for this effect, our Pop. III galaxies would have similar luminosity to those predicted by Trinca et al. (2023).

The main limitation of our results is that, given the small size of the simulation, we intrinsically miss the brightest galaxies (at $z \geq 9$ we do not get galaxies brighter than $M_{\rm AB} \simeq -19$). Larger simulation volumes will allow us to be conclusive, but this result suggests that if Pop. III stars are still forming at $z \geq 10 - 12$, and they have a top-heavy IMF, they do not require increased star formation efficiencies to outshine the Pop. II systems. As Pop. III dominated galaxies become much more rare at $z \lesssim 10$, this scenario allows us to increase the abundance of bright galaxies only at $z > 10$ without boosting the bright end of the UV luminosity function at lower redshift hence we achieve a good agreement with early JWST observations from Donnan et al. (2023); Harikane et al. (2023) and Pérez-González et al. (2023).

3.5. Conclusions

In this chapter, we studied Pop. III star formation in mini-halos with an updated version of the meraxes semi-analytic model of galaxy formation that includes Lyman-Werner background and the streaming velocities. We also implemented external metal enrichment following the growth of the supernova bubbles according to the Sedov-Taylor model. We computed the bubble size distribution function and found that our results agree with Trenti et al. (2009) (most bubbles are smaller than $150h^{-1}$ ckpc at $z = 6$ and

have a typical size of $100-200$ ckpc at $z=5$) hence most halos get self-enriched rather than externally polluted. Only low-mass halos ($M_{vir} \leq 10^{7.5} M_{\odot}$) at $z<10$ are more likely to get their metals from the IGM. This is a consequence of the small size of the supernova bubbles that results in a small filling factor (0.1% at $z=12$ and less than 1% at $z=5$.)

The free parameters allow us to explore the global properties of Pop. III dominated galaxies. We ran this model on top of a dark matter-only N-body simulation able to resolve all the mini-halos down to $\sim 3\times10^{5} M_{\odot}$ at $z \leq 30$. We explored the impact on the SMF and SFRD of the main free parameters of our model. All models converge at $z \lesssim 10$. However, Pop. III star formation efficiency and IMF lead to differences at high-z.

Finally, we investigated the SED evolution of a Pop. III dominated galaxy for different IMFs. The shorter lifetime of a Pop. III galaxy motivated us to use an instantaneous star formation model when computing the luminosity function. We computed the total and the Pop. III galaxy UV luminosity functions and compared these to the early JWST results in order to study whether the excess of bright galaxies at high-z could be explained by a population of Pop. III dominated galaxies. Having explored different IMFs and star formation efficiencies, our model predicts, for a log-normal IMF with a characteristic mass of 60 $M_{\odot}$ and a Pop. III star formation efficiency comparable to the Pop. II, most of the brightest galaxies at $z \geq 12$ and all at $z=16$ ($M_{AB}=-18$) are Pop. III dominated. Even with a smaller mass or a Salpeter IMF, Pop. III dominated systems still have an impact on the bright end of the UVLF at $z=16$. In conclusion, this work supports the scenario for which top-heavy Pop. III dominated galaxies might explain the abundance of bright JWST galaxies at $z \geq 12$ without requiring very high star formation efficiencies or extremely weak feedback at high-z.

CHAPTER 4

HeII emission from Pop. III star formation during the Epoch of Reionization.

Alice come te la passi?
Com'è la vita nei palazzi?
Ma ti ricordi quei ragazzi al tea party, teiera maxi
Esagerati com'era Gatsby

Caparezza - Il mondo dopo Lewis Carroll (2021)

This chapter is based on a preliminary draft in preparation of

E. M. Ventura, A. Venditti, R. Schneider, V. Bromm, J. B. Muñoz, J. S. B. Wyithe

to be submitted to Monthly Notices of the Royal Astronomical Society

Reformatted with the following change only:

- **The text is styled and restructured to match the rest of this thesis.**

4.1. Introduction

In the previous chapter we focused on the first episodes of star formation mostly occurring in metal-free mini-halos ($\lesssim 10^7$ $M_\odot$) or in strongly LW irradiated atomic cooling

halos ($\sim 10^8$ $M_\odot$) at $z \gtrsim 15-20$. Under such conditions, a direct detection is extremely challenging with JWST even under optimistic assumptions on the IMF and lensing magnification (e.g. Schauer et al. 2020; Trussler et al. 2023) and one can only hope to see an impact on the UVLF. However, the metal enrichment of the IGM and ISM is not an instantaneous process (see Section 3.2.5), and a number of cosmological simulations and semi-analytical models have shown that Pop. III star formation can persist down to $z \sim 5$. This late Pop. III star formation is expected in metal-free pockets in more massive halos (10^{9-10} $M_\odot$, e.g. Venditti et al. 2023; Zier et al. 2025) or in halos strongly irradiated by a Lyman Werner (LW) background that halts H_2 cooling delaying the star formation until the halo is able to cool down the gas via atomic hydrogen (as seen in Chapter 3).

At the present day, only four Pop. III candidates have been detected with JWST (Vanzella et al. 2023; Maiolino et al. 2024; Wang et al. 2024; Fujimoto et al. 2025b). These candidates lack of spectroscopy except for the HeII emitter candidate in GN-z11 observed by Maiolino et al. (2024). Despite the lack of spectroscopic confirmation, the candidate found in Fujimoto et al. (2025b) at $z \sim 6.5$ within the GLIMPSE* field (Atek et al. 2023; Kokorev et al. 2025) shows key Pop. III features such as strong Hα lines and Balmer jump, undetectable metal line and no dust. As shown by Venditti et al. 2025, this observation points toward a late Pop. III star formation either more massive or burstier than what it is usually assumed.

Motivated by these observations we further updated MERAXES in order to investigate the late Pop. III star formation in more massive halos down to the Epoch of Reionization (EoR). In Chapter 3, MERAXES was updated with mini-halo physics and Pop. III star formation. That model assumes a perfect chemical mixing in the disk gas so that all stars forming in a snapshot will be either Pop. III or Pop. II. This is a typical feature of all SAMs at high-z. In this work instead we distinguish two gas phases in the disk with different metallicity assuming an inside-out chemical enrichment in the ISM. This ultimately allows the formation of two distinct stellar populations based on the metallicity of the two gas phases in the galactic disk. Within this new framework, Pop. III stars can form in the peripheric regions of the disk of atomic cooling galaxies during the EoR. With this new model we aim to predict the occurrence and the environment of this late

*http://www.jwst-glimpse.com/

Pop. III star formation and estimate their associated HeII luminosity in order to inform future JWST surveys looking for Pop. III star clusters. Recently, Hegde & Furlanetto (2025) developed a similar framework that accounts for Pop. III star formation towards the end of the EoR.

In Section 4.2 we will present the updated version of MERAXES including a new calculation of the disk size based on conservation of angular momentum (similar to what done in Marshall et al. 2019) and the calculation of the HeII luminosity based on Venditti et al. (2024). We then present the key results on the statistics of Pop. III star forming systems for various simulations in Section 4.3. Finally, in 4.4 we will briefly discuss the future work that will be done in order to predict the HeII emission of these late Pop. III clusters during the EoR in context of upcoming JWST surveys.

Our simulations use the best-fitting parameters from Planck Collaboration et al. (2016): $h = 0.6751$, $\Omega_m = 0.3121$, $\Omega_b = 0.0490$, $\Omega_\Lambda = 0.6879$, $\sigma_8 = 0.8150$, and $n_s = 0.9653$.

4.2. HeII luminosity of Pop. III galaxies in meraxes

Our starting point is the SAM Meraxes with the updates presented in Chapter 3.

The gas reservoirs of a galaxy in MERAXES (cold, hot and ejected) were so far assumed to be chemically homogeneous. Under this approximation, Pop. III stars can form only in low mass halos that have not experienced star formation because of the very efficient enrichment from Pop. III supernovae. We now relax this approximation by assuming that the enrichment proceeds inside-out and so we split the disk reservoir in two components: an inner and more chemically enriched part and an outer, less enriched part which in principle might host Pop. III star formation at later times. This is schematised in Fig. 4.1 and the details of this implementation are discussed in 4.2.2.

Since this new model relies on using accurate disk morphology we also update the calculation of disk size following Marshall et al. (2019) as described below.

4.2.1. *Angular momentum transfer model*

In previous versions of MERAXES, the scale radius of the disk $R_{\rm disk}$ is computed from the spin parameter of the host halo $\lambda = |\vec{j}_H|/(\sqrt{2}R_{\rm vir}V_{\rm vir})$ as $R_{\rm disk} = R_{\rm vir}\lambda/\sqrt{2}$ where

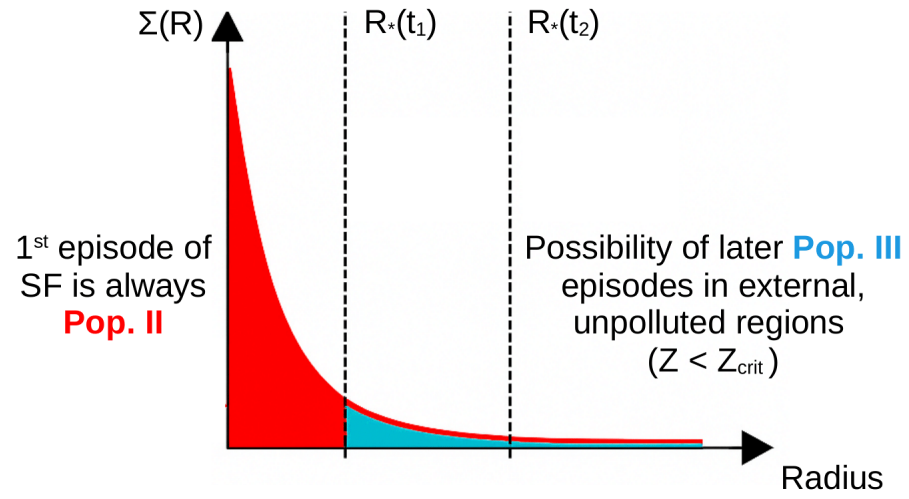

Figure 4.1: Inside-out disk scheme.

R_{vir} and V_{vir} are the virial radius and velocity of the halo and $\bar{j}_H$ is the specific angular momentum (Mo et al. 2010). The rotational velocity of the gas disk V_{disk} is equal to the maximal circular velocity of the halo. While the properties of dark matter halos provide a good approximation for these disk quantities, they can also jump significantly between adjacent snapshots due to imperfection of the halo finder algorithms. These have been highlighted by a recent work of Chandro-Gómez et al. (2025) and include the *small halo problem* and the *central-satellite swap*. Ultimately, this results in an unphysical evolution of disk radius and velocity.

We therefore implement a physically motivated prescription already introduced in Marshall et al. (2019) to compute the scale radius and velocity of galactic disks which assumes the conservation of angular momentum throughout all processes that increment or remove gas from the disk. Note that, differently from Marshall et al. (2019), we do not split the galaxy into a bulge and a disk component, but we assume that galaxy are pure disks. We refer the interested reader to Marshall et al. (2019) as here we only summarise the key assumptions and features.

As in the previous versions, the disk profile is assumed to be of an exponential thin disk $\Sigma(r) = (M_{\rm disk}/2\pi R_{\rm disk}^2)e^{-r/R_{\rm disk}}$ with a flat rotation curve $V(r) = V_{\rm disk}$. Any change of mass in the disk is treated as a vectorial summation of the existing disk (1) and a pseudo-disk of the added (or removed) material (2). By assuming energy and angular momentum conservation the properties of the new disk after the material has been added or removed

can be computed as:

$$V_{\rm new} = \sqrt{\frac{M_1 V_1^2 + M_2 V_2^2}{M_1 + M_2}} \tag{4.1}$$

$$R_{\rm new} = \frac{|\bar{J}_{\rm new}|}{2 V_{\rm new}(M_1 + M_2)} \tag{4.2}$$

where $\bar{J}_{\rm new} = \bar{J}_1 + \bar{J}_2$ is the total angular momentum of the new disk.

This process is applied throughout the entire evolution of the disk from the gas cooling, until the star formation and the associated supernova feedback. We highlight that this update concerns only the disk. The hot gas which resides in the halo is still assumed to have the same angular momentum as the dark matter halo $\bar{j}_H$. Additionally, since we do not have bulges, we do not consider gravitational instabilities of the disk that transfer stellar mass from the disk to the bulge as in Marshall et al. (2019).

4.2.2. 2-phase gas model

After having improved the calculation of the disk properties we now introduce the 2-phase disk model which provides the backbone of this work to study late Pop. III star formation. We apply this formalism in a large box ($L = 210h^{-1}$ cMpc) resolving all the atomic cooling halos at $z \leq 20$ ($M_{\rm res} \simeq 3 \times 10^7 M_\odot$) already introduced in Balu et al. (2023a).

Under the assumption of an inside-out enrichment we can split the gas disk into an inner and outer reservoir with different metallicities. To determine the radius at which this splitting occurs we follow the approach outlined below:

1. Before a galaxy formed any stars, the disk gas is assumed to be at the same metallicity above the critical value to form Pop. III stars. We adopt this conservative assumption since we do not follow the evolution of the galaxy when it was a mini-halo and likely already formed stars providing some metals in the cold gas reservoir. Under this approximation, the first episode of star formation of a galaxy in MERAXES is always Pop. II.

2. When a galaxy form stars for the first time, we define the new variable $R_\star$ which indicates the radius up to which the galaxy is forming stars. Following Croton et al. (2016), this can be computed from the disk scale radius and is given by $3 \times R_{\rm disk}$. This radius defines the separation between the inner and the outer region of the galaxy, the inner region ($R \leq R_\star$) will be polluted with metals ejected from the supernovae, while the outer region ($R > R_\star$) is not directly polluted by metals. This external region can get metals only from the hot gas when it cools down as we assume that the hot gas will accrete uniformly onto the disk. So we will have two different metallicities inside (Z_1) and outside (Z_2) $R_\star$ with $Z_1 > Z_2$.

3. At each following snapshot, the galaxy will increase its mass (and consequently $R_{\rm disk}$) while $R_\star$ stays fixed. We compute how much metals and gas from the hot reservoir will accrete onto the two different regions under the assumption of an exponential thin disk profile $\Sigma_{\rm disk}(r)$. The total mass cooled at the snapshot i $M_{\rm cooling,i}$ is splitted into the internal ($M_{\rm cooling,1}$) and external ($M_{\rm cooling,2}$) component by integrating the disk profile so that $M_{\rm cooling,1} = \int_0^{R_\star} 2\pi\Sigma(r) r dr$ and $M_{\rm cooling,2} = \int_{R_\star}^{\infty} 2\pi\Sigma(r) r dr$. The same is done for the metals.

4. At a later time, when the same galaxy will undergo a second episode of star formation, the galaxy can form two different stellar population: at $R \leq R_\star$ the star will form with metallicity Z_1 while outside with metallicity Z_2. This opens up a scenario for which we can form Pop. III stars in the outer disk if Z_2 is below the critical metallicity defining the Pop. III/II transition. $R_\star$ will then be updated according to the new value of $R_{\rm disk}$.

5. In case of major merger that triggers star formation, we will assume a perfect mixing between the gas reservoirs of the two galaxies (disks are assumed to be destroyed by a major merger), hence we will compute the metallicity of the disk of the newly formed galaxy summing the metals of the two merging galaxies over the total cold gas. In case of a minor merger instead, the small galaxy is accreted

onto the big one without any disk disruption and the new $R_\star$ will be inherited from the larger galaxy.

Despite this framework assumes an exponential thin disk profile which does not necessarily represent the morphology of high-z galaxies, we highlight that the amount of gas accreted in the two distinct reservoirs depends only on the integrated quantity making the result less sensitive to the specific morphological model. Finally, while this model represents a significant advancement to spatially resolve different galactic regions at high-z within a semi-analytical model, with this framework we can differentiate only between two different regions purely based on the galactocentric distance without resolving finer spatial structures.

4.2.3. Simulation runs

With this framework in place, we ran six simulations varying different Pop. III parameters (see Table 4.1). As discussed in Section 3.3, the main Pop. III parameters are the IMF, the critical metallicity Z_{crit} and the star formation efficiency (SFE) $\alpha_{SF,III}$. All the simulations use the new two-phase disk model with the updated computation of disk size and include self-consistent reionization.

We chose the same fiducial model as in 3.3. This simulation is quite conservative as it assumes a bottom-heavy IMF (Salpeter between 1 and 500 $M_\odot$) and a low SFE (10% of the value adopted for the Pop. II one, where $\alpha_{SF,II} = 0.06$). We then explore more optimistic - but still reasonable - assumptions on the star formation efficiency and IMF. All the runs except for the last one include the external metal enrichment introduced in Section 3.2.5 that allows galaxies to accrete chemical enriched gas when a galaxy is found inside a metal bubble.

4.2.4. HeII model

In order to compute the luminosity of the HeII line associated with a Pop. III cluster, we adopted the same formalism presented in Venditti et al. (2024) where

$$L_{HeII} = E_{HeII}\bar{\epsilon}_{HeII}M_{\star,III} \tag{4.3}$$

is the intrinsic HeII luminosity emitted by a Pop. III star cluster with mass $M_{\star,III}$, $E_{HeII} \simeq 10^{-11}$ erg is the energy of a HeII photon ($\lambda = 1640$Å) and $\bar{\epsilon}_{HeII}$ is the average HeII emissivity per unit of stellar mass. This latter quantity is obtained by integrating the time-averaged HeII photon production rate of individual Pop. III stars $\epsilon_{HeII}(M)$ over the adopted IMF $\phi(M)$ as:

$$\bar{\epsilon}_{HeII} = \frac{\int \phi(M)\epsilon_{HeII}(M)dM}{\int \phi(M)dM}. \tag{4.4}$$

We took the tabulated values of $\epsilon_{HeII}(M)$ for the chosen IMFs from Schaerer (2002) assuming no mass loss. We highlight that the value of $\bar{\epsilon}_{HeII}$ changes significantly depending on which IMF is chosen and for more top-heavy IMFs (e.g. Salpeter between 50 and 500 $M_\odot$) can be up to two order of magnitudes higher than for a bottom-heavy IMF. This model assumes no dust attenuation.

4.3. Results

4.3.1. Pop. III statistics

We start by analyzing the statistics of Pop. III systems in the fiducial simulation. In particular we will be focusing at $z \lesssim 10$ in order to compare with the JWST Pop. III candidates detected so far.

Fig. 4.2 shows the total (black line) and Pop. III (cyan line) stellar mass function (SMF) at $z = 6 - 10$. This is computed using all the active stars in the galaxy (solid line) and the ones formed at that snapshot (dashed lines). The high-mass tail ($M_\star \gtrsim 10^6$ $M_\odot$) is entirely populated by Pop. II stellar systems as expected. The peak of the Pop. III stellar mss is at $\sim 10^4$ $M_\odot$ with a tail extending up to 10^6 $M_\odot$. Given the choice of the Salpeter IMF for Pop. III stars, if a galaxy experiences more than one episode of Pop. III star formation, it can build up more Pop. III stellar mass as shown by the difference between the dashed and solid cyan lines. While this leads to more massive Pop. III systems ($\sim 10^6$ $M_\odot$ at $z = 6$), most of these stars would have low masses (< 8 $M_\odot$) hence they would likely be undetectable). If we look instead at the masses formed in that snapshot, the most massive Pop. III cluster at $z = 6$ has a Pop. III mass of $\sim 6 \times 10^5$ $M_\odot$.

In Fig. 4.3 we then look at the galaxy main sequence (i.e SFR vs stellar mass) at $z = 6.5$.

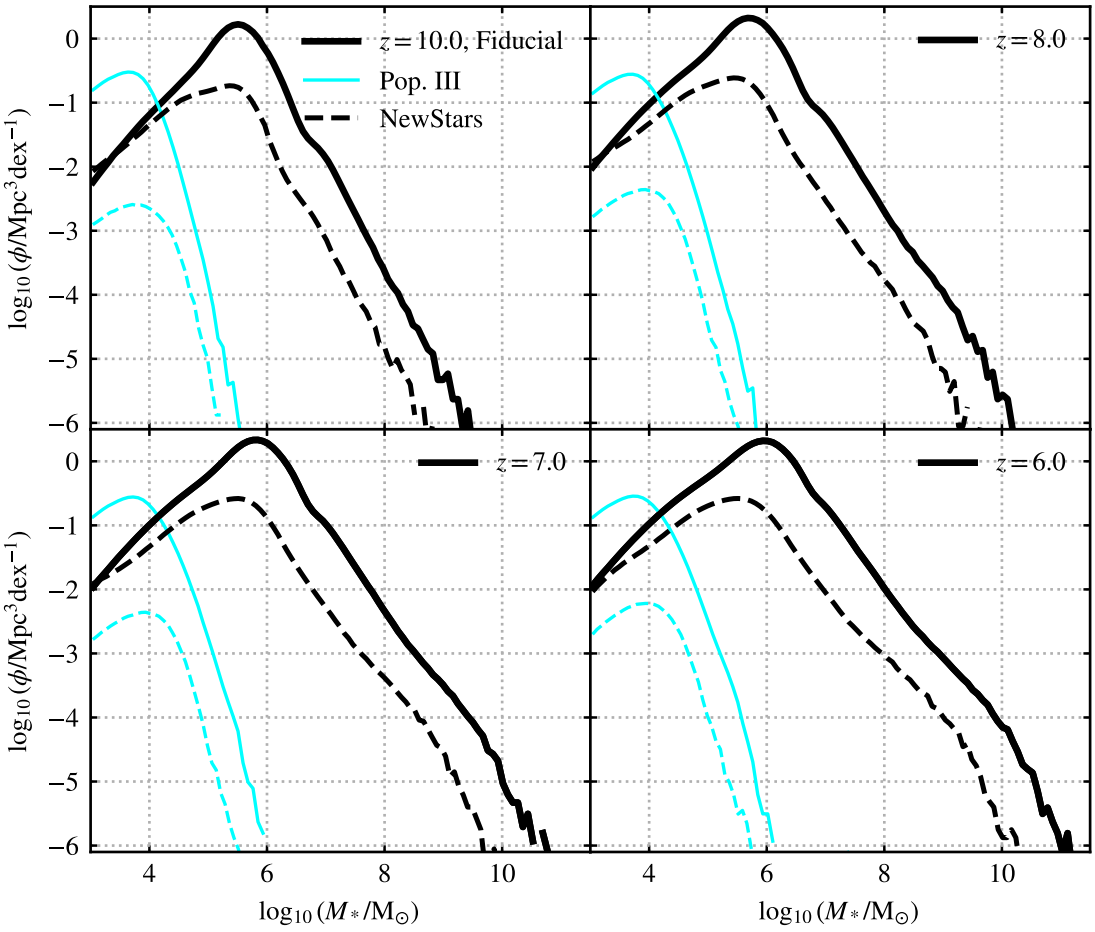

Figure 4.2: SMF at z = 10, 8, 7, and 6 for all stars (black) and Pop. III (cyan) using the fiducial model. Dashed line show the masses of the stars formed in that snapshot.

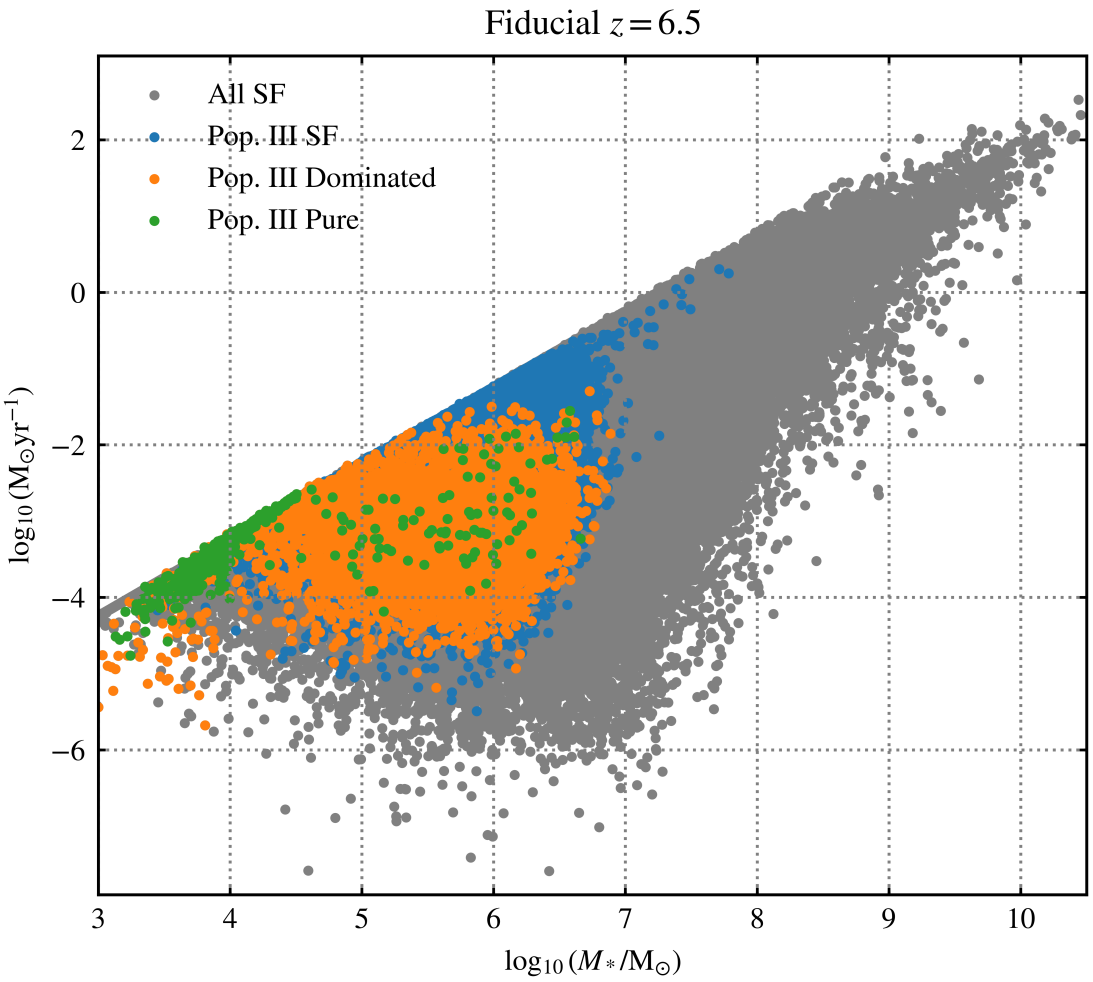

Figure 4.3: MS of star forming galaxies in MERAXES at $z = 6.5$. Pop. III star forming, dominated and pure galaxies are highlighted with blue, orange and green dots respectively.

Here we highlight the galaxies that are forming Pop. III stars. Specifically, blue, orange and green dots represents galaxies in which the Pop. III star formation is subdominant ($< 50\%$), dominant ($\geq 50\%$) or pure ($\geq 99\%$). Most of systems hosting Pop. III stars have total stellar masses below $\sim 5 \times 10^6$ $M_\odot$ with a few galaxies of $\sim 10^7$ $M_\odot$ with subdominant Pop. III star formation. Both Figures 4.2 and 4.3 indicate that during the EoR, Pop. III star formation survives only in the low-mass end of the atomic cooling halos and the average Pop. III masses can be up to few 10^5 $M_\odot$.

4.3.2. Impact of the external metal enrichment

The results from the previous section show that, in more massive galaxies during the EoR, metal enrichment is sufficient to raise the gas metallicity above the critical threshold, effectively halting Pop. III star formation. In the fiducial run, metals originate either from in-situ star formation and subsequent supernova (SN) enrichment or are accreted into the hot halo from nearby SN-driven bubbles. As discussed in Section 3.2.5, this external enrichment can significantly impact low-mass halos during the EoR. We now adopt a more optimistic assumption for which galaxies always accrete pristine gas in the hot halo unless they are reincorporating gas from the ejected reservoir.

In Fig. 4.4 we compare the SMF at $z = 6.5$ obtained with the fiducial (black and cyan) and the No External Enrichment (grey and blue) simulations. While the high mass end of the total SMF is almost unchanged, the Pop. III contribution are significantly affected. In the No External Enrichment run (blue lines), Pop. III cluster are significantly more common and the high-mass tail extends to higher masses (the most massive Pop. III cluster has $M \sim 10^6$ $M_\odot$. Despite this high-mass tail, the distribution still peaks at mass of $\sim 10^4$ $M_\odot$.

Turning off the external metal enrichment affects also the galaxy MS as shwon in Fig. 4.5. While the global distribution is almost identical, there are significantly more Pop. III systems in the $10^5 - 10^7 M_\star$ range. Specifically, a large number of galaxies with $\sim 10^6 M_\star$ are Pop. III dominated or pure. As for the SMF, the high-mass tail of the MS is entirely populated by galaxies that are forming only Pop. II stars showing that the external enrichment affects only low-mass galaxies.

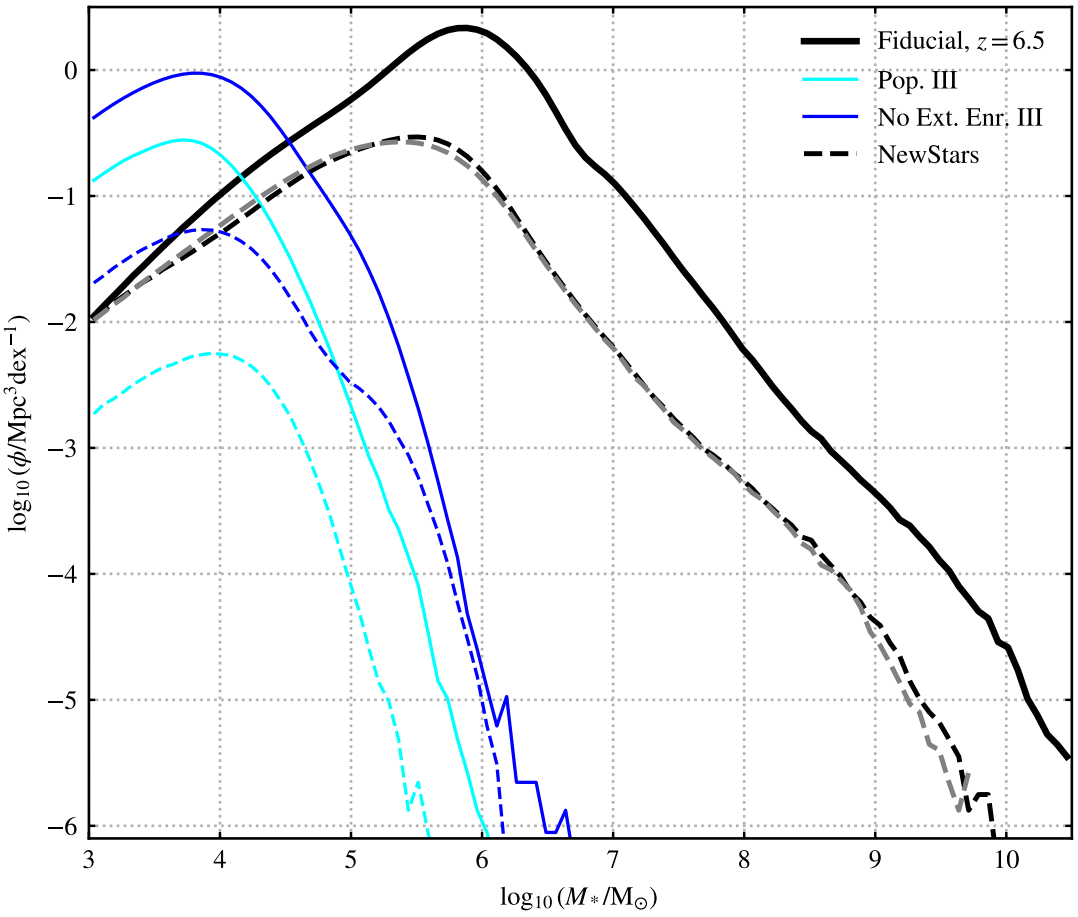

Figure 4.4: Same as Fig. 4.2 focusing at $z = 6.5$ and including also the run with no external metal enrichment (grey and blue lines).

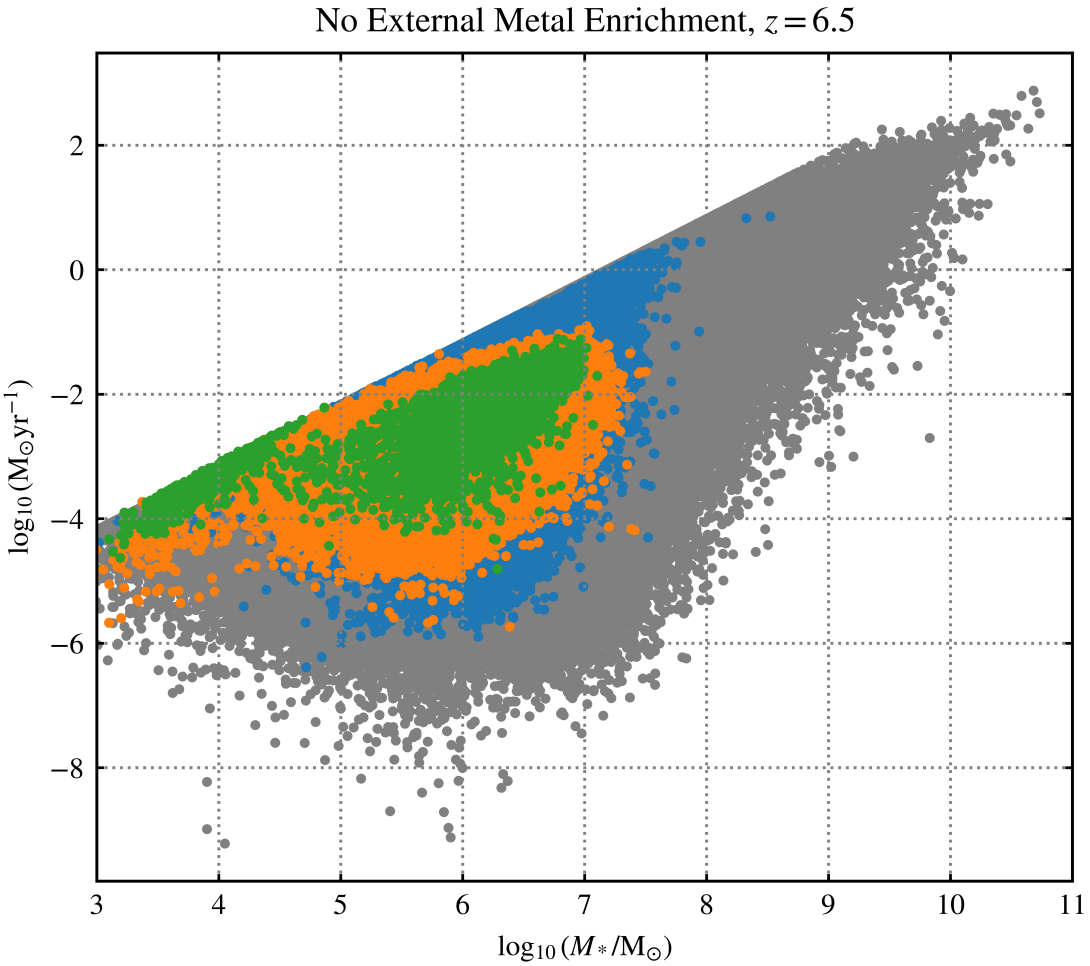

Figure 4.5: As Fig. 4.3 for the No External Enrichment run.

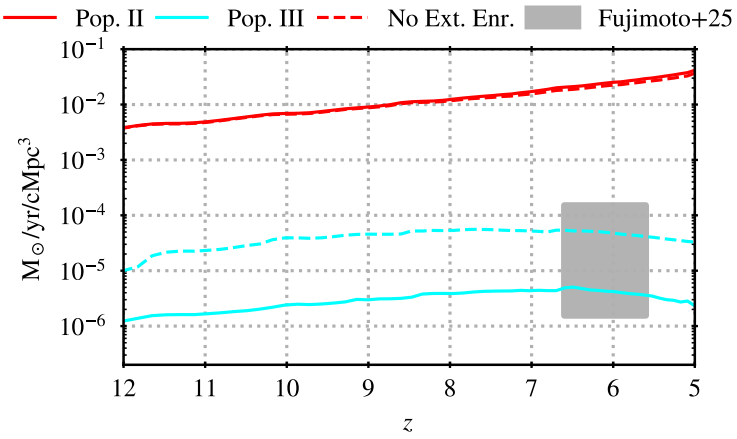

Figure 4.6: Pop. II (red) and Pop. III (cyan) SFRD vs z for the fiducial (solid) and No External Enrichment (dashed) simulation together with the constraint from Fujimoto et al. (2025b).

4.4. Discussion and future work

These preliminary results indicate that Pop. III star formation persists down to the EoR in peripheral regions of low-mass atomic cooling halos even under conservative assumptions of low star formation efficiency and efficient chemical enrichment. The next step is to assess whether or not these Pop. III clusters are observable in order to inform future JWST surveys hunting for Pop. III stars. While we have not estimated the HeII luminosity associated with the Pop. III star forming systems yet, we can compare the global star formation rate density (SFRD) with the first constraints from Fujimoto et al. (2025b) based on the GLIMPSE Pop. III candidate at $z \sim 6.5$. As shown in Fig. 4.6, turning off the external metal enrichment increases the global Pop. III SFRD in atomic cooling halos by an order of magnitude during the EoR. This leaves almost unchanged the Pop. II contribution since the cyan line is several orders of magnitude below the red one. Both simulations fall within the constraint from Fujimoto et al. (2025b) at $z \sim 6.5$ showing that at this stage, having only one Pop. III candidate, is probably too early to differentiate between optimistic and conservative Pop. III models.

As a future step that will not be discussed in this thesis, we will investigate various Pop. III models (see Table 4.1), compute the HeII luminosity distribution and compare it with the candidate identified by Fujimoto et al. (2025b).

Name	$\alpha_{SF,III}$	Z_{crit}	Pop. III IMF	External Metal enrichment
Fiducial	$0.1 \times \alpha_{SF,II}$	$10^{-4} Z_\odot$	Salpeter [1,500]$M_\odot$	On
High SFE	$\alpha_{SF,II}$	$10^{-4} Z_\odot$	Salpeter [1,500]$M_\odot$	On
Low Z_{crit}	$0.1 \times \alpha_{SF,II}$	$10^{-6} Z_\odot$	Salpeter [1,500]$M_\odot$	On
LogA IMF	$0.1 \times \alpha_{SF,II}$	$10^{-4} Z_\odot$	Log-Normal centered at $10 M_\odot$	On
Extreme IMF	$0.1 \times \alpha_{SF,II}$	$10^{-4} Z_\odot$	Salpeter [50,500]$M_\odot$	On
No External Enrichment	$0.1 \times \alpha_{SF,II}$	$10^{-4} Z_\odot$	Salpeter [1,500]$M_\odot$	Off

Table 4.1: Simulation parameters.

CHAPTER 5

Semi-analytic modelling of Pop. III star formation and metallicity evolution - II. Impact on 21cm power spectrum.

Mi chiamo Marco, sento il gelo dei riflettori
Vorrei rimanerne fuori, ma il mondo vuole che vada in tour
Entro in classifica perché la fama è cieca
Così cieca che in fondo non mi riguarda più

Caparezza - La Scelta (2021)

This chapter is based on

E. M. Ventura, Y. Qin, S. Balu, J. S. B. Wyithe (2025),

Monthly Notices of the Royal Astronomical Society: 540, 483

Reformatted with the following changes only:

- **The text is styled and restructured to match the rest of this thesis.**
- **Where necessary, bibliographic records are updated.**

Simulating Population (Pop.) III star formation in mini-halos in a large cosmological simulation is an extremely challenging task but it is crucial to estimate its impact on the 21cm power spectrum. In this work, we develop a framework within the semi-analytical code MERAXES to estimate the radiative backgrounds from Pop. III stars needed for the computation of the 21cm signal. We computed the 21cm global signal and power spectrum for different Pop. III models varying star formation efficiency, initial mass function (IMF) and specific X-ray luminosity per unit of star formation (L_X/SFR). In all the models considered, we find Pop. III stars have little to no impact on the reionization history but significantly affect the thermal state of the intergalactic medium (IGM) due to the strong injection of X-ray photons from their remnants that heat the neutral IGM at $z \geq 15$. This is reflected not only on the 21cm sky-averaged global signal during the Cosmic Dawn but also on the 21cm power spectrum at $z \leq 10$ where models with strong Pop. III X-ray emission have larger power than models with no or mild Pop. III X-ray emission. We estimate observational uncertainties on the power spectrum using 21CMSENSE and find that models where Pop. III stars have a stronger X-ray emission than Pop. II are distinguishable from models with no or mild Pop. III X-ray emission with 1000 hours observations of the upcoming SKA1-low.

5.1. Introduction

Observations and models of the EoR are converging on a scenario where the Universe was completely ionized by $z \sim 5.3$ (e.g. Fan et al., 2006; Ouchi et al., 2010; McGreer et al., 2015; Chardin et al., 2015; Planck Collaboration et al., 2020; Qin et al., 2021a; Bosman et al., 2022; Jin et al., 2023; Qin et al., 2024) with reionization likely driven by low-mass halos (e.g. Kuhlen & Faucher-Giguère 2012; Finkelstein et al. 2012; Robertson et al. 2015; Qin et al. 2021b; Saxena et al. 2024; Mutch et al. 2024, although see Muñoz et al. 2024 and Witstok et al. 2025). However, the impact of Pop. III stars and mini-halos on the EoR is unclear. Pop. III stars are likely to be the dominant contribution to the total star formation rate density (SFRD) at $z > 15-20$ and, if their IMF is more top-heavy than the present day one, Pop. III could significantly contribute to the heating and the ionization of the IGM which determines the evolution and shape of the 21cm signal (e.g. Qin et al.,

2020; Gessey-Jones et al., 2022; Sartorio et al., 2023).

The 21cm signal (introduced in section 1.4.2) represents our most promising tool to put constraints on the thermal state of the IGM during the Cosmic Dawn and EoR. Even though no confirmed detection has been reported so far, the first upper limits on the 21cm power spectrum obtained with HERA phase I strongly disfavour cold reionization scenarios (HERA Collaboration et al. 2023).

Assessing the role of Pop. III stars during the EoR and on the 21cm signal is particularly challenging from a computational point of view. The variety and complexity of the processes involved in Pop. III star formation and the resolution required to keep track of the evolution of the gas particles, limits the size of hydrodynamical simulations to ~ 100 kpc (see 2.2). At the same time, to study the EoR volumes of at least ~ 200 Mpc are required (Iliev et al. 2014; Kaur et al. 2020; Balu et al. 2023a and section 1.5.2). Even SAMs that include Pop. III star formation in mini-halos arrive only up to scales of ~ 10 Mpc.

In the last few years, the impact of Pop. III stars on the 21cm signal has been studied using both analytical and semi-analytical models (e.g. Cohen et al., 2017; Chatterjee et al., 2020; Mebane et al., 2020; Qin et al., 2020; Magg et al., 2022; Gessey-Jones et al., 2022; Muñoz et al., 2022; Hegde & Furlanetto, 2023; Ventura et al., 2023; Sartorio et al., 2023; Cruz et al., 2024a). However these models either did not compute reionization (e.g. Magg et al. 2022; Hegde & Furlanetto 2023; Cruz et al. 2024a), focusing only on the absorption trough of the 21cm signal occurring at $z \sim 13 - 20$, or used a very simple analytical approach to compute reionization (e.g.Ventura et al. 2023). On the other hand, Cohen et al. (2017), Qin et al. (2021a) and Muñoz et al. (2022) used a simple analytical model for modeling Pop. III star formation but computed the reionization self-consistently.

In this work, we overcome these challenges using a realistic Pop. III star formation and mini-halo model (see Chapter 3) developed within the semi-analytical model MERAXES designed to self-consistently couple galaxy formation and reionization. While in Chapter 3 we ran this model on a small (L $\sim$ 10 Mpc) and high-resolution box, here we extend it to a significantly larger volume simulation (L $\sim$ 310 cMpc) enabling the study of cosmic reionization. Since at such large volumes we cannot directly resolve mini-halos, we implemented scaling relations between the SFRD and the dark matter

density field calibrated on the results from the small and high-resolution box discussed in Chapter 3. With this new model we are able to accurately follow the evolution of the radiative backgrounds relevant to the EoR and 21cm signal (X-rays, Lyman-α, ionizing UV, Lyman-Werner) and to disentangle the contribution of Pop. III star formation to the 21cm global signal and power spectrum. Pop. III stars are expected to have a stronger impact at $z \geq 15$ where they dominate star formation and ionization. In this work we focus our attention on the residual signature of Pop. III on the 21cm power spectrum at $z \leq 10$ where the sensitivity of SKA is expected to be significantly better and a detection is more plausible. This study allows us to assess under which conditions an early heating of the IGM from Pop. III stars leaves a detectable imprint on the 21cm power spectrum at $z \leq 10$.

This chapter is structured as follows. In Section 5.2 we give a brief overview of Pop. III star formation in MERAXES. In Section 5.3 we present the scaling relation between the SFRD in mini-halos and the density field calibrated from the small and high-resolution box which is implemented in the large $(310\ \mathrm{cMpc})^3$ box. In Section 5.4 we discuss the impact of different Pop. III star formation models on the 21cm power spectrum and in Section 5.5 we make forecasts on the observability of these power spectra with SKA. Finally, we summarize our main results and conclusions in Section 5.6. Our simulations use the best-fit parameters from the Planck Collaboration et al. (2016): $h = 0.6751$, $\Omega_m = 0.3121$, $\Omega_b = 0.0490$, $\Omega_\Lambda = 0.6879$, $\sigma_8 = 0.8150$, and $n_s = 0.9653$.

5.2. Pop. III galaxies in Meraxes

This chapter relies on the latest version of the SAM MERAXES* introduced in Chapter 3 that includes Pop. III star formation and mini-halo physics. Here we only summarise the free parameters calibrated against observations (see Tables 5.1 and 5.2). Values in Table 5.1 are calibrated against observed luminosity functions and stellar mass functions at $z \sim 5-8$ while those in Table 5.2 are calibrated against constraints on the neutral hydrogen fraction, ionizing emissivity and the Thomson scattering optical depth τ_e from Planck Collaboration et al. (2020). As shown in 3.3, the Pop. III parameters with the

*https://github.com/meraxes-devs/meraxes

Table 5.1: Main free parameters for galaxy formation.

Parameter	Description	Fiducial value
$\alpha_{\rm SF,II}$	Pop. II Star formation efficiency	0.1
$\alpha_{\rm SF,III}$	Pop. III Star formation efficiency	see Table 5.4
η_0	Mass loading normalization	7.0
ϵ_0	Supernova energy coupling normalization	1.5
$Z_{\rm crit}$	Critical metallicity for Pop III star formation	$10^{-4} Z_\odot$
$\Sigma_{\rm norm}$	Critical surface density of cold gas for star formation	0.37 $M_\odot$ pc^{-2}
Pop. III IMF	Shape of Pop. III IMF	Sal [1, 500] $M_\odot$
$E_{\rm PISN}$	Energy from Pair Instability SN	10^{52} erg
$E_{\rm CCSN}$	Energy from Core Collapse SN	10^{51} erg

largest impact are the star formation efficiency $\alpha_{\rm SF,III}$ and the shape of the IMF. The latter has a large impact on galaxy evolution as it determines the strength of the feedback and the emission properties of the Pop. III stellar population. In the following sections we quickly summarize the main features of MERAXES relevant for this work.

5.2.1. *Galaxy formation*

The galaxy formation part of MERAXES used in this chapter is almost identical to the one presented in Chapter 3. The only update is the addition of the effect of H_2 self-shielding which counteracts the H_2 photo-dissociation, increasing the Pop. III SFRD by up to one order of magnitude at $z \sim 10$ (see e.g. Feathers et al. 2024). We discuss the details of the implementation and impact of H_2 self-shielding in MERAXES at the end of this section.

The main free parameters that regulate the galaxy formation in MERAXES are summarized in Table 5.1. The Pop. II related ones are taken from Balu et al. (2023a) where MERAXES was run on a cosmological volume of L = 210 h^{-1} cMpc resolving all atomic cooling halos and calibrated in order to match the observed UV luminosity functions at $z \sim 4-7$ (the agreement holds up to $z \sim 13$ as shown in Qin et al. 2023) and the stellar mass functions at $z \sim 5-8$. Given the lack of observations of Pop. III stars, the Pop. III parameters are largely unconstrained. The fiducial values adopted in this work are taken from 3.3 and their values are suggested from hydrodynamical simulations (e.g. Chon et al., 2021).

Table 5.2: Main free parameters for reionization.

Parameter	Description	Fiducial value
$f^0_{\rm esc,III}$	Pop. III escape fraction normalisation	0.14
$f^0_{\rm esc,II}$	as above for Pop. II	0.14
$\alpha_{\rm esc,III}$	Pop. III escape fraction redshift scaling	0.2
$\alpha_{\rm esc,II}$	as above for Pop. II	0.2
$L_{\rm X<2keV,III}$/SFR	specific Pop. III X-ray luminosity per unit star formation	see Table 5.4
$L_{\rm X<2keV,II}$/SFR	as above for Pop. II (erg s^{-1} M$_\odot^{-1}$yr)	3.16×10^{40}

Including the H_2 self-shielding in MERAXES

Many recent simulations (e.g. Nebrin et al., 2023; Hegde & Furlanetto, 2023) have assessed the importance of incorporating H_2 self-shielding in mini-halos as it significantly changes the minimum mass of mini-halos capable of cooling down the gas via molecular cooling ($M_{\rm crit,MC}$). While this was not implemented in Section 3.2, for this work we now included it by updating $M_{\rm crit,MC}$ (Eq. 3.4) taking the fitting function found in Kulkarni et al. (2021):

$$M_{\rm crit,MC} = M_{z=20}(J_{\rm LW}, v_{\rm bc})\left(\frac{1+z}{21}\right)^{-\alpha(J_{\rm LW}, v_{\rm bc})} \tag{5.1}$$

where

$$\begin{aligned} M_{z=20}(J_{\rm LW}, v_{\rm bc}) = (M_{z=20})_0 (1 + J_{\rm LW}/J_0)^{\beta_1} \\ \times (1 + v_{\rm bc}/v_0)^{\beta_2} (1 + J_{\rm LW} v_{\rm bc}/J v_0)^{\beta_3} \end{aligned} \tag{5.2}$$

and

$$\begin{aligned} \alpha(J_{\rm LW}, v_{\rm bc}) = \alpha_0 (1 + J_{\rm LW}/J_0)^{\gamma_1} (1 + v_{\rm bc}/v_0)^{\gamma_2} \\ \times (1 + J_{\rm LW} v_{\rm bc}/J_0 v_0)^{\gamma_3}. \end{aligned} \tag{5.3}$$

$M_{\rm crit,MC}$ is a function of the Lyman-Werner flux ($J_{\rm LW}$) in 10^{-21} erg s^{-1} cm^{-2} and the rms streaming velocity at recombination ($v_{\rm bc}$) in km s^{-1}. This result is normalized to the minimum halo mass at $z = 20$ in absence of LW background and streaming velocity ($M_{z=20})_0$ and to typical values for LW background and streaming velocity ($J_0 = 1, v_0 = 30$). α_n and β_n are free parameters calibrated to fit results of hydrodynamical simulations in Kulkarni et al. (2021). This fit accounts for the H_2 self-shielding, so it makes the effect

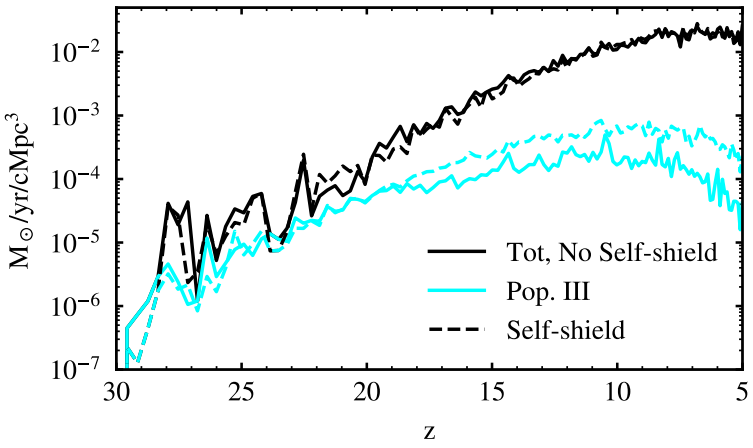

Figure 5.1: Total (black) and Pop. III (cyan) SFRD vs redshift without (solid) and with (dashed) accounting for H_2 self-shielding.

of the LW background on $M_{crit,MC}$ less strong compared to what was previously assumed in 3.2 (Visbal et al. 2015). As shown in Fig. 5.1, accounting for self-shielding increases the Pop. III SFRD, especially when the Lyman-Werner background starts to build up. At $z \leq 15$ the Pop. III SFRD when the H_2 self-shield is considered (cyan dashed line) is ~ 1 order of magnitude higher than the no self-shield scenario (cyan solid). Similar results have been found by Feathers et al. (2024).

5.2.2. Reionization and radiative backgrounds

Together with galaxy formation, MERAXES self-consistently computes the reionization and thermal evolution of the IGM using a modified version of the semi-numerical code 21cmFAST (Mesinger et al. 2011). In this work, we compute the backgrounds relevant for the computation of the 21cm signal: the UV ionizing, X-rays, Lyman-α and Lyman-Werner (LW). The first is crucial to study the evolution of the reionization, while the X-ray and the Lyman-α backgrounds determine the thermal state of the IGM. In particular the X-ray background is likely to be the dominant contribution to the heating of the IGM once the first galaxies form and the lyman-α background is responsible for the coupling between the kinetic and the spin temperature of the neutral hydrogen. The LW background does not directly affect the IGM temperature, but determines whether or not mini-halos have enough molecular hydrogen to cool the gas and form Pop. III

stars. Hereafter, we briefly summarize the key quantities that determine the evolution of these backgrounds. For a more detailed explanation on the implementations of these backgrounds, we refer the reader to Balu et al. (2023a) for the UV, Lyman-α and X-ray and to 3.2 for the LW.

The ionizing background is mostly dependent on the SFRD, the average number of ionizing photons per stellar baryon N_γ and the escape fraction of the UV photons f_{esc}. The second quantity is mostly determined by the IMF: for Pop. II stars we adopt a Kroupa IMF which leads to $N_\gamma \sim 6000$. Since the Pop. III IMF is a free parameter in our model, $N_{\gamma,\mathrm{III}}$ is computed from the IMF adopted using the Pop. III stellar spectra from (Raiter et al. 2010; $N_{\gamma,\mathrm{III}} \sim 20000 - 70000$). f_{esc} is tuned to reproduce the EoR histories in agreement with observations. As per Balu et al. (2023a), we adopt a redshift-dependent escape fraction defined as followed:

$$f_{\mathrm{esc}} = f_{\mathrm{esc}}^{0}\left(\frac{1+z}{6}\right)^{\alpha_{\mathrm{esc}}}. \tag{5.4}$$

X-ray emission is mostly associated with high mass X-ray binaries (HMXB) and its contribution is proportional to the SFRD. In this work we use the widely adopted approximation for the comoving X-ray specific emissivity (erg s^{-1} Mpc^{-3}) $\epsilon_x \propto L_X/\,\mathrm{SFR} \times \mathrm{SFRD}$. Finally, we need to account for the fact that only photons with an energy below 2 keV (soft X-rays) are able to heat the IGM. As a result the main free parameter that regulates X-ray emissivity is the soft X-ray luminosity per unit star formation $L_{X<2keV}$ / SFR. For Pop. II stars, this quantity is estimated from theoretical studies of emission spectra of HMXBs in low metallicity environments (e.g. Fragos et al., 2013; Madau & Fragos, 2017; Das et al., 2017; Qin et al., 2020; Kaur et al., 2022). For Pop. III stars there are no observational constraints as this quantity depends on the unknown Pop. III IMF. Recently, Sartorio et al. (2023) estimated the L_X / SFR for Pop. III stars and found that for more top-heavy IMFs this quantity can be up to two orders of magnitude higher than the Pop. II value.

We highlight that in this work we separately compute the backgrounds from Pop. III and Pop. II stars due to the different spectra, properties and star formation rate density of the two distinct populations.

5.2.3. *21cm physics*

Using the radiative backgrounds computed from the galaxy population in MERAXES, we can estimate the 21cm signal. We encourage the reader to see Furlanetto et al. (2006), Morales & Wyithe (2010), Pritchard & Loeb (2012) and Liu & Shaw (2020) for reviews on the topic. Hereafter we only summarize the key equations used in this work (see also Balu et al. 2023a).

We start with the 21cm brightness temperature field ($\delta T_{\rm b}$) which measures the deviation of the spin temperature of the neutral hydrogen ($\rm T_S$) from the cosmic background $\rm T_\gamma$ (i.e. the CMB). This is given by (Furlanetto et al., 2006):

$$\begin{aligned}\delta T_{\rm b} &= \frac{T_S - T_\gamma}{1+z}(1 - e^{-\tau_{\nu_0}}) \\ &\simeq 27 x_{\rm HI}(1+\delta_{\rm nl})\left(\frac{H}{dv_r/dr + H}\right)\left(1 - \frac{T_\gamma}{T_S}\right) \\ &\times \left(\frac{1+z}{10}\frac{0.15}{\Omega_m h^2}\right)\left(\frac{\Omega_b h^2}{0.023}\right)\rm mK,\end{aligned} \tag{5.5}$$

where τ_{ν_0} is the optical depth at the 21cm transition frequency ν_0, $\rm x_H$ is the neutral hydrogen fraction, $1 + \delta_{nl}$ is the density contrast in the dark matter field, $H(z)$ is the Hubble parameter at the redshift z, and dv_r/dr is the radial derivative of the line-of-sight component of the peculiar velocity. Once the cosmological model (Planck Collaboration et al. 2016) and the velocity and density field (from the N-body simulation) are fixed, $\delta T_{\rm b}$ is determined by the ionization and the spin temperature fields. The latter quantifies the population ratio of the two $\rm H_I$ hyperfine energy levels and is sensitive to the thermal state (i.e. the kinetic temperature $\rm T_K$) of the gas as follows:

$$T_S^{-1} = \frac{T_\gamma^{-1} + x_\alpha T_\alpha^{-1} + x_c T_{\rm K}^{-1}}{x_\alpha + x_{\rm c} + 1}, \tag{5.6}$$

where $\rm T_\alpha$ is the colour temperature which we take equal to $\rm T_K$ while $\rm x_\alpha$ and $\rm x_c$ are the Lyman-α and collisional coupling coefficients, respectively. These coefficients quantify the strength of the processes (resonant scattering of Lyman-α photons, Wouthuysen 1952, and collisions with free electrons) that drive the spin temperature towards the ki-

Table 5.3: Simulation parameters.

Label	Box side (cMpc)	Mass resolution ($M_\odot$)	Pixel side
L10	$10\ h^{-1}$	4.71×10^5	$0.2\ h^{-1}$
L210	$210\ h^{-1}$	3.16×10^7	$0.2\ h^{-1}$

netic temperature (when $x_\alpha + x_c >> 1$, $T_S \sim T_K$ otherwise $T_S \sim T_\gamma$). T_K is sensitive to the adiabatic cooling and to all the processes able to heat up (or cool) the IGM with the most dominant coming from the X-ray emission. Hence in this work we will consider only the X-ray heating neglecting the other source of heating such as primordial magnetic fields (Minoda et al. 2019; Bera et al. 2020; Cruz et al. 2024b), Lyman-α (Ciardi et al. 2010; Reis et al. 2021; Mittal & Kulkarni 2021), shocks (Furlanetto et al. 2004; Gnedin & Shaver 2004; Ma et al. 2021), cosmic rays (Bera et al. 2023), early accreting black holes (Mebane et al. 2020; Ventura et al. 2023) and decaying or annihilating dark matter (Liu & Slatyer 2018; Sun et al. 2023; Hou & Mack 2024; Facchinetti et al. 2024). Ultimately, the evolution of T_S during the Cosmic Dawn and the EoR is mostly determined by the Lyman-α (for the coupling between T_S and T_K) and X-ray flux.

Using Eq. 5.5 we can estimate both the all-sky averaged global signal and its fluctuations (i.e. the power spectrum). In this work we will often use the reduced power spectrum $\Delta^2_{21}(k) = k^3/2\pi^2 P_{21}(k)$ unless otherwise stated.

5.3. Putting Pop. III galaxies and mini-halos in a large-scale simulation

In this section, we present a novel approach that enables us to efficiently estimate the SFRD from mini-halos in a large box (that does not directly resolve these objects) using results from a small, high-resolution box. In Table 5.3 we summarize the key parameters for both the small (L10) and large (L210) box.

5.3.1. Calibrating scaling relations from the L10 box

Our starting point is the small ($L = 10h^{-1}$ cMpc) high-resolution (halo mass resolution of $M \sim 4.7 \times 10^5\ M_\odot$) simulation used in Chapter 3. When building a scaling relation

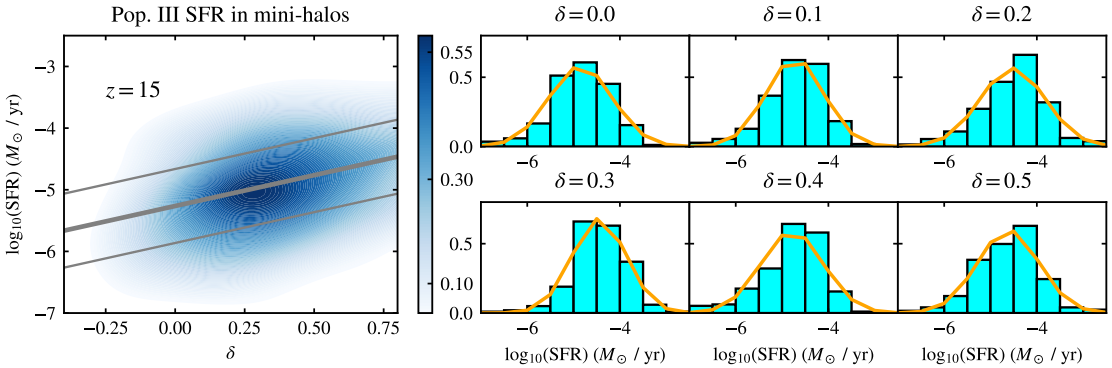

Figure 5.2: Left panel shows the density distribution of Pop. III star formation rate in mini-halos ($M_\odot\ yr^{-1}$ in logarithm scale) vs the dark matter overdensity δ for each pixel at $z = 15$. The thick grey line shows the analytical fit SFR $\propto e^{\delta}$ similar to the one adopted by Muñoz (2023) together with the 1σ deviation (thin lines). For different values of δ (highlighted with the black rectangles) we show the distribution of Pop. III SFR in mini-halos (in logarithm scale) together with the best Gaussian fit.

between SFR and other physical quantity, the first obvious choice is the dark matter density field δ. For instance Muñoz (2023) showed, as a first-order approximation, SFR scales as e^{δ_R} where δ_R is the density field smoothed over a certain radius R and this relationship works quite well for $\delta \sim 0$ and large R ($\geq$ 3Mpc). To link our SFR in mini-halos with the density field, we first compute density, $\delta(\mathbf{x}, z)$, and SFR grids for both Pop. III, $\mathrm{SFR}_{\mathrm{MC,III}}(\mathbf{x}, z)$, and Pop. II, $\mathrm{SFR}_{\mathrm{MC,II}}(\mathbf{x}, z)$, in the L10 box using the same grid resolution used in Balu et al. (2023a) to compute reionization ($\mathrm{L}_{\mathrm{pixel}} \sim 0.3$ cMpc) and accounting for the SFR within mini-halos. We highlight that our $\mathrm{L}_{\mathrm{pixel}}$ is quite small compared to the smoothing radius R adopted by Muñoz (2023), hence we expect a significant scatter in the above relation. We also split the contribution between Pop. III and Pop. II stars (a chemically enriched mini-halo will form Pop. II stars). In the left panel of Fig. 5.2 we show our Pop. III SFR distribution as a function of the overdensity δ and with the grey line we highlight the SFR $\propto e^{\delta_R}$ relation as in Muñoz (2023). Despite the significant scatter for the reasons outlined above ($\sigma \sim 0.65$), the analytical approximation agrees with our results. The results shown hereafter are obtained from our fiducial simulation in 3.3.

We start by investigating the distribution function of $\log_{10}$(SFR) at a fixed overdensity δ and redshift $\log_{10}(\mathrm{SFR}(\delta, z))$ finding that it follows a Gaussian distribution (or lognormal in the linear space).We show results for $\log_{10}(\mathrm{SFR}_{\mathrm{III}})$ and selected values of δ in the

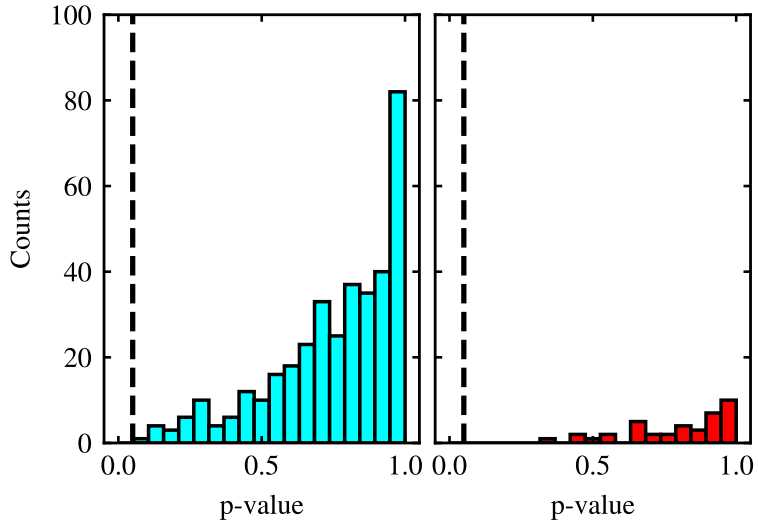

Figure 5.3: P-value distribution of K-S tests conducted on the Pop. III (left) and Pop. II (right) star forming pixels. Vertical line highlights the significant level of 0.05.

smaller panels in Fig. 5.2. Hence, we can write:

$$\Phi(\log_{10}(\mathrm{SFR_{MC}}|\delta,z)) = A(\delta,z)e^{\frac{(\log_{10}(\mathrm{SFR})-\log_{10}(\overline{\mathrm{SFR}}(\delta,z)))^2}{2\sigma(\delta,z)^2}} \tag{5.7}$$

where the normalization A, the mean $\log_{10}(\overline{\mathrm{SFR}})$ and the standard deviation σ all depend on the overdensity and redshift. The normalization is defined as the ratio between the number of SF pixels and the total number of pixels. We found the best fit parameters for each δ (grouped in bins of width = 0.1) and snapshot of the simulation. We tested whether the $\log_{10}(\mathrm{SFR})$ distribution function is indeed Gaussian by conducting a K-S test. P-values are calculated for each cell with SFR > 0 and taking a predefined significance level of 0.05 below which the null hypothesis will be rejected. Results are shown in Fig. 5.3 for both $\mathrm{SFR_{III}}$ and $\mathrm{SFR_{II}}$. P-values always exceed the significance level for both Pop. III (left panel) and Pop. II (right panel) SFR suggesting that the Gaussian distribution reproduces $\Phi(\log_{10}(\mathrm{SFR_{MC}}|\delta,z))$ both in the Pop. III and Pop. II cases. As expected, we see that there are far more Pop. III star forming pixels than Pop. II ones as mini-halos are more likely to form Pop. III stars.

The next step is to study how the mean, standard deviation and normalization evolve with δ and z. In Fig. 5.4 we show the redshift evolution of these parameters for $\delta = 0.5$ (black), 1.0 (grey), 1.5 (purple), 2.0 (red), 2.5 (green) and 3.0 (blue). $\overline{\mathrm{SFR}}_{\mathrm{MC,III}}$ exhibits

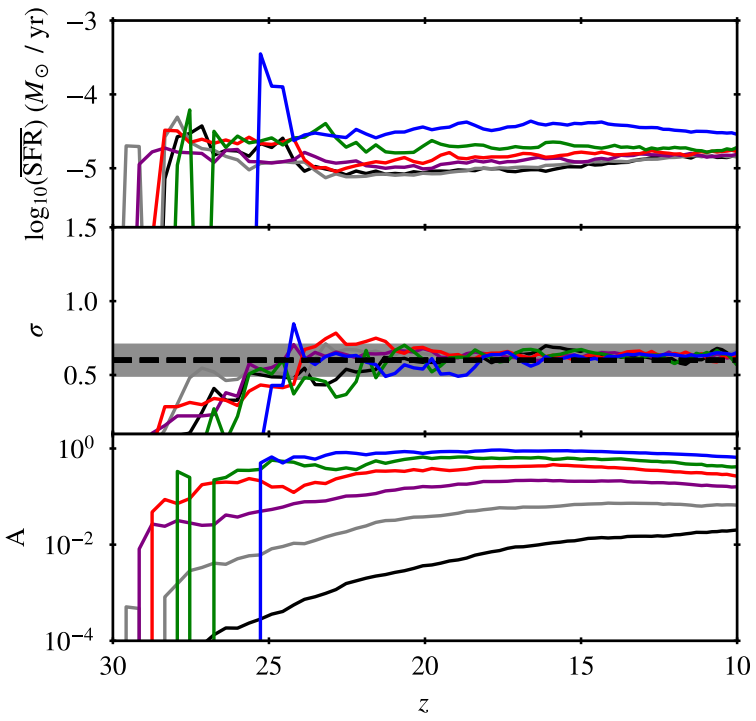

Figure 5.4: Redshift evolution of $\log_{10}(\overline{\mathrm{SFR}})$ (top panel), σ (mid) and A (bottom) for Pop. III for δ = 0.5 (black), 1.0 (grey), 1.5 (purple), 2.0 (red), 2.5 (green) and 3.0 (blue).

an almost constant trend in redshift and a correlation with δ (higher δ results in higher $\overline{\mathrm{SFR}}_{\mathrm{MC,III}}$). This demonstrates that $\overline{\mathrm{SFR}}_{\mathrm{MC,III}}$ is mostly determined by the number of Pop. III star forming halos in a pixel, which is higher for more overdense regions. Since Pop. III star formation episodes in mini-halos are often the first episode of star formation experienced by a galaxy, it is not impacted by supernova feedback[†] so the Pop. III SFR is almost constant at all redshift. This also explains why σ is constant for all z and δ ($\sigma_{\mathrm{MC,III}} \sim 0.65$). The parameter that is more sensitive to both δ and z is the normalization. For very overdense regions ($\delta \geq 2$) it is almost one, meaning that almost all the overdense pixels host Pop. III SF mini-halos. For lower δ there is also an evolution in z as, with cosmic time, lower density regions will host a larger number of mini-halos above the minimum mass for star formation. We repeated the same analysis for Pop. II star forming pixels (see Fig. 5.5). In this case the evolution is more scattered as Pop. II

[†]Even though supernova feedback can be neglected, this is not true for the Lyman-Werner background that halts star formation in mini-halos. For this reason we add a further condition that if a pixel is irradiated by a LW flux $J_{\mathrm{LW}} \geq J_{\mathrm{crit}}$ above a critical threshold defined as $M_{\mathrm{crit,MC}} = M_{\mathrm{ato}}$ (the atomic cooling threshold), $\Phi(\log_{10}(\mathrm{SFR_{MC}})) = 0$. M_{ato} is the virial mass correspondent to a halo with a virial temperature $T_{\mathrm{vir}} = 10^4$ K. while $M_{\mathrm{crit,MC}}$ is defined in Eq. 5.2.

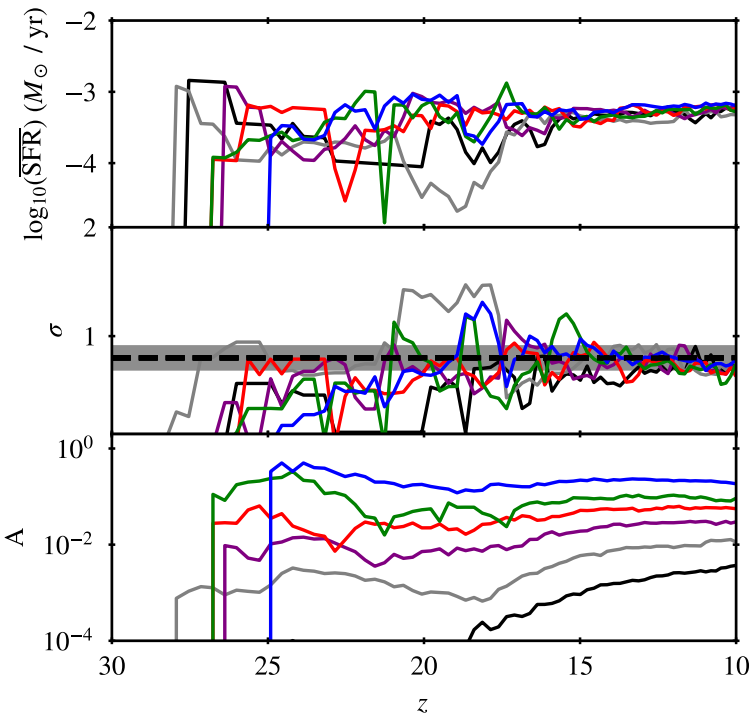

Figure 5.5: Same as Fig. 5.4 for Pop. II.

star formation episodes are not the first star forming episodes within a galaxy and so will be affected by both mechanical and chemical feedback from the previous history of the galaxy. This is also demonstrated by the larger standard deviation ($\sigma_{\mathrm{MC,II}} \sim 0.8$). The average value of $\overline{\mathrm{SFR}}_{\mathrm{MC,II}}$ is ~ 1 order of magnitude higher than for Pop. III. This reflects the higher Pop. II star formation efficiency. Finally, $\mathrm{A_{II}}$ is always smaller than $\mathrm{A_{III}}$ showing that it is less likely for a mini-halo to form Pop. II stars.

We test this parametrization on the small box by estimating the mini-halo contribution to the Pop. III and Pop. II SFRD from the matter density field. To do this, we read the density grid at each z and for each pixel assign a value of Pop. III SFR drawn randomly from $\Phi(\log_{10}(\mathrm{SFR_{MC,III}}))$ using δ of the pixel. We repeat the same procedure for $\mathrm{SFR_{MC,II}}$ adding the constraint that in order to have $\mathrm{SFR_{MC,II}} > 0$ that pixel needs to already have experienced a Pop. III star formation episode. This latter condition ensures a more realistic enrichment model (a pixel cannot have Pop. II star formation if it has not previously hosted Pop. III star formation). We ran twenty different realizations and for each realization estimated the $\mathrm{SFRD_{MC,III}}$ and $\mathrm{SFRD_{MC,II}}$ and compared with results of

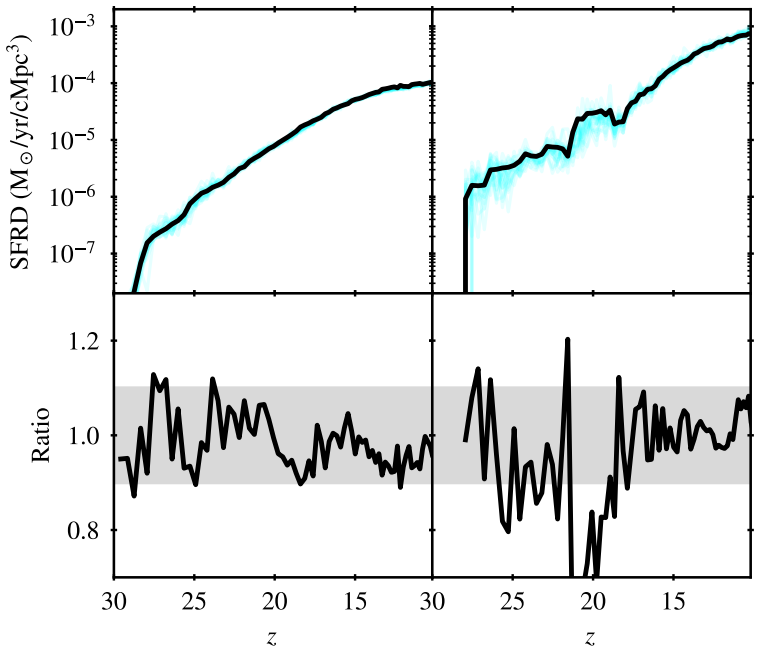

Figure 5.6: **(top)** Pop. III (left) and Pop. II (right) SFRD vs z from MERAXES (black) and estimated from the density field (cyan). **(bottom)** ratio between the average of the 20 realizations for the SFRD estimated from the density field and the SFRD from MERAXES.

the simulations. Results are shown in Fig. 5.6. In the upper panels we show the Pop. III (left) and Pop. II (right) SFRD from MERAXES output (black line) and from each realization using the method outlined above (cyan shaded lines). In the lower panels we show the ratio between the average of the 20 realizations and the true SFRD from MERAXES. All the realizations are in reasonable agreement with the data and the ratio is always lower than $\sim 10\%$ for both populations. This demonstrates the validity of the method outlined above.

The main advantage of this method is that it allows estimation of the SFRD from minihalos in a simulation where these are not directly resolved. Parametrizing SFRD with a Gaussian distribution enables us to account for stochastic star formation (different pixels with same δ can have different SFR), without losing the correlation with the matter density field ($\overline{\mathrm{SFR}}, \sigma$ and A all depend on δ). This method can be applied as long as the density field from both the low and the high resolution simulation share the same properties (mean, standard deviation) and it can be calibrated for any choice of parameters.

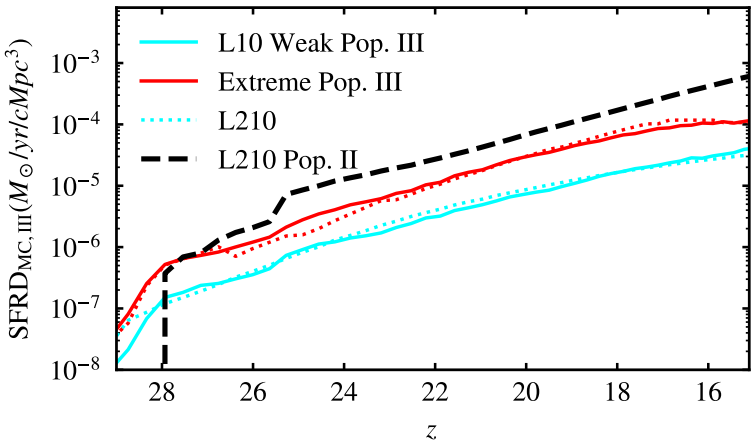

Figure 5.7: $\mathrm{SFRD_{MC,III}}$ vs z from the L10 (solid) and L210 (dotted) box for two different Pop. III star formation models (see more details in text and Table 5.4).

5.3.2. *Applying scaling relations to the L210 box*

We can now apply the methodology outlined in the previous section to the L210 box that can only resolve the atomic cooling halos by reading the density field and applying $\Phi(\log_{10}(\mathrm{SFR_{MC}}))$ calibrated on different models. In Fig. 5.7 the mini-halo contribution to the Pop. III SFRD shows a good agreement between the two different simulations.

We highlight that our scaling relations do not explicitly depend on the Lyman-Werner background (except for the regions that are strongly irradiated by LW flux for which $\Phi(\log_{10}(\mathrm{SFR_{MC}})) = 0$). This implicitly assumes that both the L10 and L210 box have similar LW backgrounds. We verify this assumption by computing the average LW background and LW maps in both simulations (See Fig. 5.8). In the bottom right panel we show the redshift evolution of the LW background (in units of 10^{-21} erg s^{-1} cm^{-2} Hz^{-1} sr^{-1}) in the L10 (black line) and in the L210 box (red line). The two lines share similar trends showing that both simulations have a similar average LW background. The left and top right panels show the 2D projections of the LW field in the large and small box. These maps illustrate that the LW background is roughly uniform (as expected given that the mean free path of LW photons is ~ 100 Mpc). These plots demonstrate that the LW fields in the small and large box are indeed comparable showing that the estimation of the star formation in mini-halos with the scaling relations accounts for the radiative

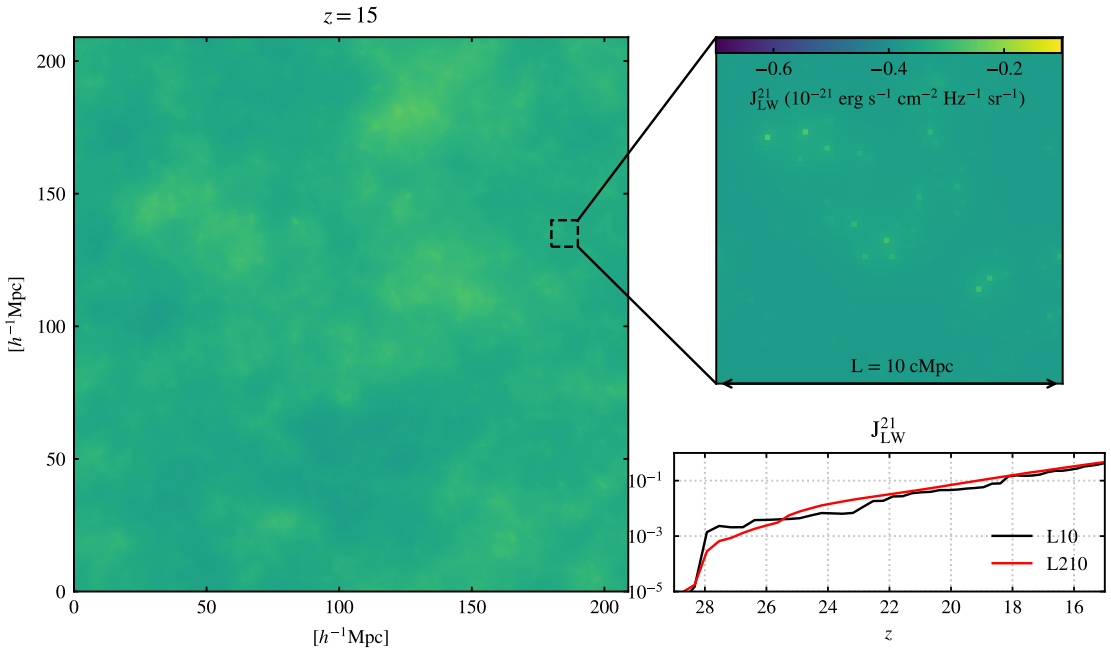

Figure 5.8: Left panel shows the 2D projections of the LW background (units of 10^{-21} erg s^{-1} cm^{-2} Hz^{-1} sr^{-1} in the L210 box at $z = 15$. Top right panel shows the same map but in the L10 simulation. Bottom right panel shows the redshift evolution of the average LW background (same units as above) in both the L10 (black line) and L210 (red line) simulation.

feedback[‡].

Differently from what has been done by Hazlett et al. (2024) who calibrated a semi-analytical model to the *Reinassance* simulation in order to account for Pop. III star formation by adding the previous star formation history to each atomic cooling galaxy resolved in the simulation, the methodology described in this section allows us to estimate only the *total* SFRD occurring in mini-halos within a certain pixel of the simulation. We also highlight that, a similar work was also performed by Feathers et al. (2025) using a neural network and investigating the impact of streaming velocity and LW background. In this work we focus on three models of Pop. III star formation by varying three main parameters: the star formation efficiency, the IMF and the specific Pop. III X-ray luminosity per unit star formation while all the other free parameters (e.g. the escape fraction) are fixed at the fiducial value (see Tables 5.1 and 5.2). We chose to focus only on these three parameters since these have the strongest impact on both the evolution of the Pop. III

[‡]In this discussion we neglected the UV photo-ionizing feedback. This is justified by the fact that this effect impacts more the low-mass atomic cooling halos at $z \lesssim 10$ rather than mini-halos.

Table 5.4: Pop. III model parameters.

Label	IMF type*	$\alpha_{\rm SF,III}$	$L_{\rm X<2keV,II}$/SFR
Weak Pop. III	Salpeter	0.008	3×10^{40}
Moderate Pop. III	Salpeter	0.008	3×10^{41}
Extreme Pop. III	logE	0.08	3×10^{42}
High SFE	Salpeter	0.08	3×10^{40}
LogE	logE	0.008	3×10^{40}

*see Table 3.2 for the details

SFRD and the amount of UV and X-ray photons emitted. The values chosen for the specific Pop. III X-ray luminosity per unit star formation are similar to those found in Sartorio et al. (2023) for the different IMFs explored in their work. Hereafter, we analyze three different Pop. III models designed to have the minimum, intermediate and maximum impact from Pop. III star formation in mini-halos, each model is summarized in Table 5.4. The IMFs considered in this model are a Salpeter between 1 and 500 solar masses and a log-Normal IMF centered at 60 $M_\odot$ (see 3.3 for more details). We highlight that in our extreme Pop. III model we enhance star formation efficiency, L_X/SFR and the top-heaviness of the IMF at the same time. Each of these parameters has a different impact on the evolution of the 21cm signal (see 5.4.1 for a more detailed discussion of how each Pop. III parameter changes the evolution of the 21cm global signal and power spectrum).

5.4. Impact of Pop. III star formation on 21cm physics

We can now estimate how different Pop. III star formation models in meraxes affect the 21cm signal. We started by verifying that, after introducing the additional Pop. III contribution to the fiducial Pop. II only model (Balu et al. 2023a) we still obtain reionization histories consistent with the observational constraints on the Thomson scattering optical depth τ_e (Fig. 5.9) and $\bar{x}_{\rm HI}$ (Fig. 5.10). The reionization histories from the models with Pop. III stars are only slightly modified and this negligible contribution comes from the secondary ionizations from X-rays. This is expected given that at $z \leq 15$ the Pop. III SFRD is at least one order of magnitude lower than Pop. II and their main contribution is expected from the X-ray emission rather than the UV.

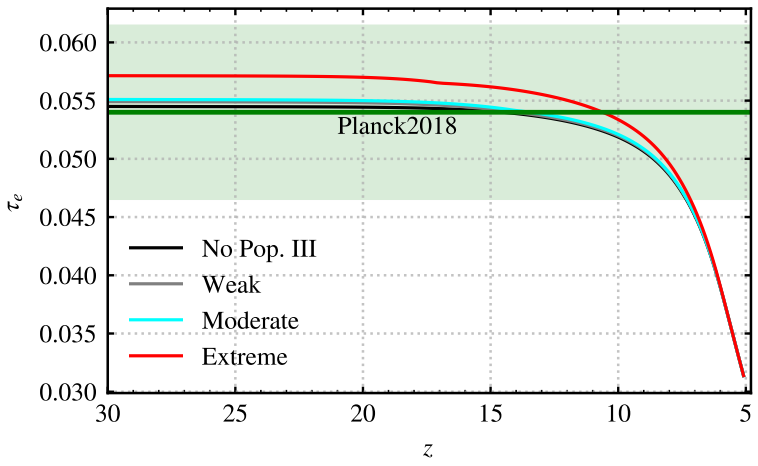

Figure 5.9: Integrated Thomson scattering optical depth τ_e computed for model with weak (grey), moderate (cyan), extreme (red) Pop. III and Balu et al. (2023a) (black). The green curve and shaded region show the measurement of τ_e from the Planck 2018 collaboration (Planck Collaboration et al. 2020)

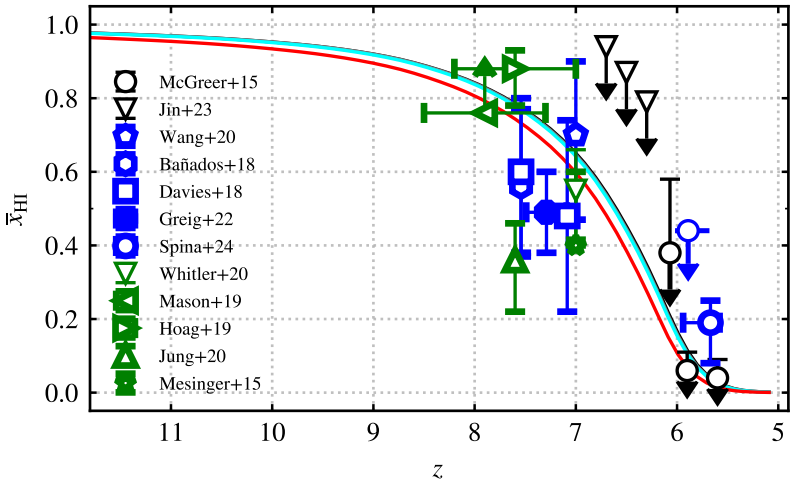

Figure 5.10: Constraints on the reionisation history (neutral hydrogen fraction vs z) for model with weak (grey), moderate (cyan), extreme (red) Pop. III and Balu et al. (2023a) (black). The observational data are from analyses of dark pixels (McGreer et al. 2015; Jin et al. 2023), damping-wing absorption in quasar spectra (Bañados et al. 2018; Davies et al. 2018; Wang et al. 2020; Greig et al. 2022; Spina et al. 2024) and equivalent width measurements (Mesinger et al. 2014; Hoag et al. 2019; Mason et al. 2019; Jung et al. 2020; Whitler et al. 2020)

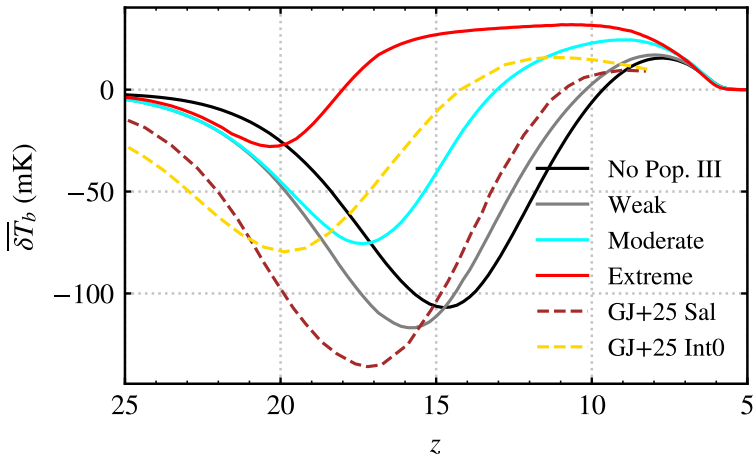

Figure 5.11: Effect of Pop. III star formation on the 21cm global signal ($\delta T_{\rm b}$ vs z). Pop. III models with small X-ray heating cause a stronger absorption at earlier times, while having a stronger Pop. III X-ray heating causes the signal to be seen in emission earlier. Color coding as in the previous figures. Brown and yellow dashed lines are taken from Gessey-Jones et al. (2025) for a Salpeter (*Sal*) and flat (*Int-0*) IMF.

We compute the sky-averaged 21cm global signal (see Fig. 5.11) without (black line) and with (grey, cyan and red line for weak, moderate and extreme Pop. III respectively) Pop. III star formation. As expected, introducing a Pop. III population with the same X-ray properties as Pop. II ones (i.e. weak Pop. III), simply shifts the absorption through to earlier epochs in virtue of the stronger coupling at higher-z (see also Ventura et al. 2023; Hegde & Furlanetto 2023). However, if Pop. III stars have a stronger X-ray emission (i.e. moderate and extreme models) as suggested by Sartorio et al. (2023), the absorption signal is quickly suppressed turning into an emission signal as early as $z \sim 18$ for the extreme Pop. III model and at $z \sim 13$ for the moderate Pop. III one. We note that a similar result has been found by a contemporaneous work by Gessey-Jones et al. (2025) who found an analogous variation in the timing ($\Delta z \sim 3$) and depth ($\Delta \delta T_b \sim 50$ mK) of the absorption trough when considering a stronger X-ray contribution from Pop. III stars (in their model the L_X/SFR is self-consistently modeled from the IMF so that the difference between their *Int-0* and *Sal* model is of 2 orders of magnitudes.)

As shown in Fig. 5.12 earlier coupling and heating from Pop. III impacts the 21cm power spectrum both at the large and small scales. The models considered here produce 21cm signals that are different not only during the coupling and heating epoch ($z \sim 10-20$), but also at lower redshift when the reionization is in progress. The impact is

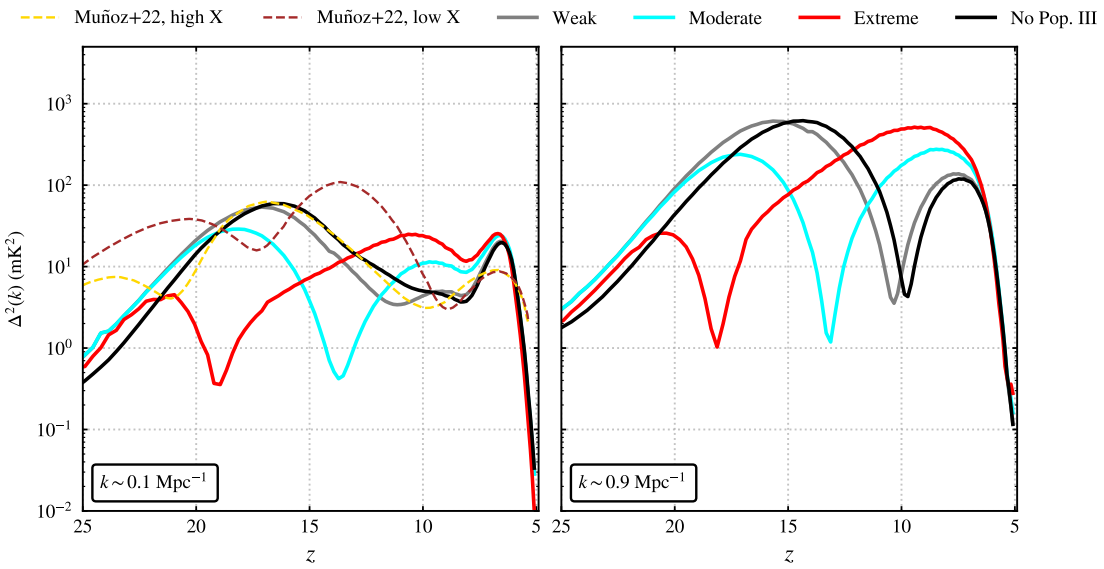

Figure 5.12: Effect of Pop. III star formation on the 21cm power spectrum (Δ_{21} vs z) at large (k $\sim$ 0.1 Mpc^{-1}) and small (k $\sim$ 0.9 Mpc^{-1}) scales. Color coding as in the previous figures. Brown and yellow dashed lines are taken from Muñoz et al. (2022) for $k = 0.23$ Mpc^{-1} assuming a weak and strong X-ray luminosity per unit of Pop. III SFR (bottom right panel of Fig. 17.)

stronger at smaller scales where models with a stronger heating exhibit a larger power spectrum at $z \sim 7-10$. This is of crucial importance as current and upcoming facilities are improving their observations at $z \leq 10$ (see more discussion in Section 5.5).

We compare our results with the ones in Muñoz et al. (2022) who studied how different Pop. III parameters impact the 21cm signal using 21cmFast. In the left panel of Fig. 5.12 the yellow and brown dashed lines are obtained by changing the specific Pop. III X-ray luminosity by a factor of 9. The global trends are similar with our models with stronger Pop. III X-ray emission (dashed yellow line and red/cyan lines) showing an earlier and weaker first peak compared to low X-ray models (dashed brown and grey lines). In their model, different Pop. III X-ray properties strongly impact the position and amplitude also of the second peak. In our models instead, the position of the second peak is only slightly anticipated in the strong X-ray models. This difference is likely due to the fact that our second peak occurs at much lower redshift ($z \sim 10$) when most of the emission comes from Pop. II stars. Finally, differently from Muñoz et al. (2022) at $z \sim 10$ simulations with a stronger Pop. III X-ray heating have a significantly larger power spectrum compared to weak X-ray models (a similar result has been found also by Gessey-Jones et al. 2025).

This analysis shows that Pop. III star formation not only impacts the 21cm global signal during the cosmic dawn as previously assessed (e.g. Qin et al., 2020; Gessey-Jones et al., 2022; Ventura et al., 2023; Hegde & Furlanetto, 2023; Cruz et al., 2024a) but also that an early ($z \geq 15$) heating of the IGM provided by this population leaves a strong signature on the power spectrum during the EoR ($z \leq 10$). The impact on the power spectrum is stronger for models that have a large Pop. III X-ray emissivity (i.e. moderate and extreme Pop. III models) while models with a milder X-ray emission (i.e. weak Pop. III) have a stronger effect on the global signal. Ultimately, this tells us that the power spectrum during the EoR can be used to disentangle different heating models and potentially constrain the properties of Pop. III stars. We highlight that here we considered only the X-ray emission from stellar remnants. While there might be other sources that significantly heat the IGM at $z \geq 15$ (see discussion at end of Section 5.2.3), the other effects are likely to be either subdominant, still related to Pop. III stars (e.g. cosmic rays) or dominant only at the dark-ages (e.g. dark matter annihilation).

Finally, we note that in this work we did not include the effect of the X-ray feedback on Pop. III star formation. As noted by Ricotti (2016); Park et al. (2021), X-rays have both a positive and negative effect on Pop. III star formation as they heat the gas and increase the electron fraction. The heating makes gas accretion more difficult (hence delaying star formation) and free electrons promote the formation of H_2 making the molecular cooling more efficient. In presence of a strong X-ray background this latter effect is dominant at $10 \lesssim z \lesssim 20$ (see e.g. Fig. 9 in Hegde & Furlanetto 2023). Hence, including the X-ray feedback would likely increase the Pop. III SFRD making the impact of Pop. III stars even stronger than what predicted here especially for the moderate and extreme models.

5.4.1. Impact of Pop. III star formation efficiency and IMF

While the 21cm power spectrum at $z \lesssim 10$ is mostly sensitive to the amount of X-ray photons from Pop. III remnants, changing the star formation efficiency and the shape of the IMF impacts the 21cm signal evolution during the coupling and heating epochs. In Fig. 5.13 and 5.14 we show the evolution of the 21cm global signal and power spectrum for the No Pop. III model (black line), Weak (grey line), Moderate (cyan line), high SFE

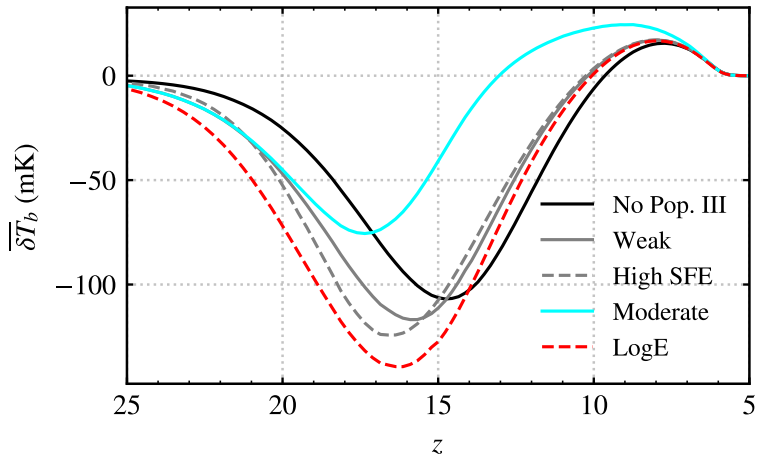

Figure 5.13: As Fig. 5.11 but showing also the High SFE (grey dashed line) and the LogE (red dashed line) models.

(dashed grey line) and LogE (dashed red line) models. Compared to the Weak Pop. III model, increasing the Pop. III star formation efficiency, increases both the amount of Lyman-α and X-ray photons (they are both linked to SFR), hence the absorption trough shifts towards higher-z ($\Delta z \sim 1$). Considering instead a top-heavy IMF, increases just the amount of Lyman-α photons hence the absorption trough becomes significantly deeper while still being at the same redshift compared to the weak Pop. III model. We note that this result is a consequence of the fact that we are considering the L_X/SFR and the shape of the IMF as two independent parameters. If, as shown in Sartorio et al. (2023), the X-ray emissivity is linked to the shape of the IMF, the LogE model is not realistic as we would need to enhance the X-ray emissivity as well.

We highlight that both the star formation efficiency and the shape of the IMF alone do not significantly affect neither the 21cm global signal nor the power spectrum at $z \lesssim 12$ so a future 21cm detection with SKA-low likely will not help to constrain these parameters if they are not linked to a significantly stronger X-ray emissivity.

5.5. Observability with SKA

In the previous section we showed that an early heating of the IGM significantly affects the 21cm power spectrum during the EoR. Now we want to investigate how our models compare with the currently available upper limits and whether their differences will be

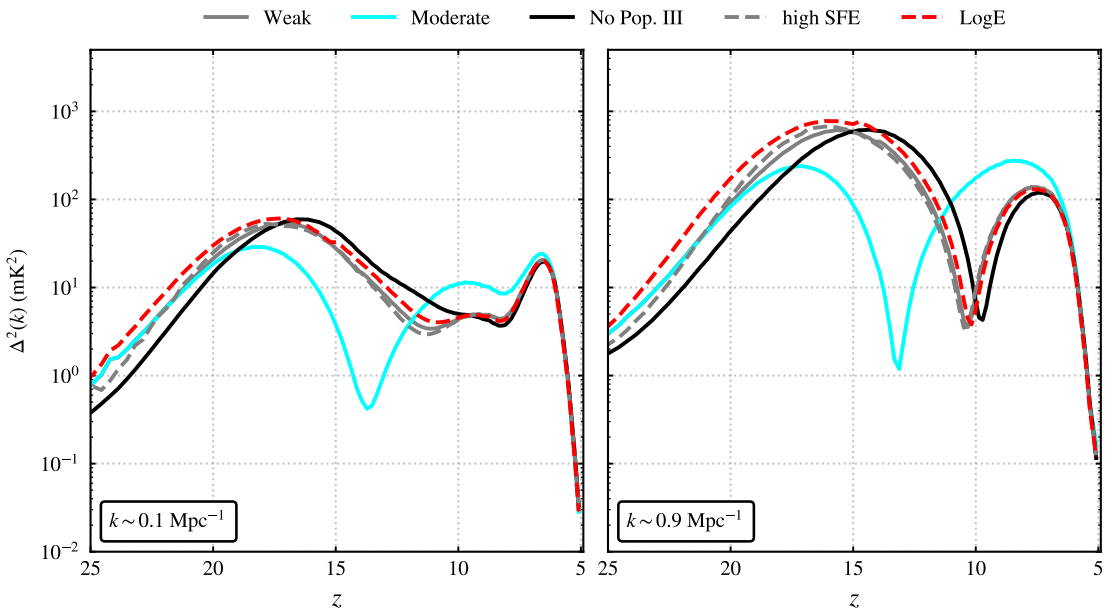

Figure 5.14: As Fig. 5.12 showing also the High SFE (grey dashed line) and the LogE (red dashed line) models.

observable with SKA. In this section we consider the power spectrum at $z \leq 10$ as the current and upcoming interferometers are significantly less sensitive at higher redshift. To better appreciate this, in Fig. 5.15 we show the power spectrum noise (mK^2) with SKA as a function of redshift at $k \sim 0.2$ and 0.9 cMpc^{-1} assuming a 1000 hours (solid lines) and 180 hours (dashed lines) observations with SKA. At higher redshift the noise steadily increases and already at $z \geq 10$ the noise is of the order of 10s to 100s mK^2 with 1000 hours observation.

Firstly, we compare our predictions with current upper limits from a number of facilities including MWA, LOFAR, GMRT, PAPER and HERA (we focus at $z = 7 - 10$ where most of the measurements have been taken). In Fig. 5.16 we show the 21cm power spectrum at $z = 10$, 9, 8 and 7 for all the four models together with the available upper limits (see label). All our models are below these upper limits. However, the moderate and extreme Pop. III models are closer to the current HERA constraints at $z = 8$ suggesting that soon these models can be either detected or ruled out. In our model the main effect of different Pop. III models is to change the timing and amplitude of the peaks in the 21cm power spectrum rather than introducing a specific feature. We note that we did not account for spatial variations in the velocity acoustic oscillations (see Section 5.2.1)

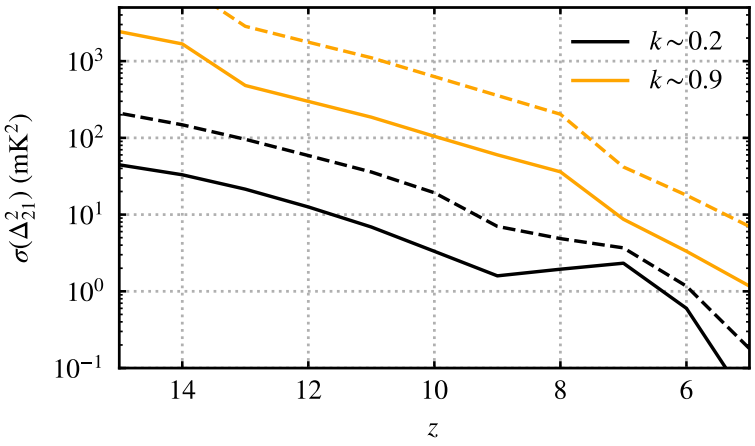

Figure 5.15: 21cm power spectrum sensitivity as a function of redshift $k \sim 0.2$ (black line) and 0.9 cMpc^{-1} (orange line) assuming a 1000 (solid lines) and 180 hours (dashed lines) observation with SKA.

which would introduce wiggles in the Δ^2_{21} at scales $k \sim 0.1$ Mpc^{-1} (Cruz et al. 2024a). While this effect can be important when focusing on the 21cm power spectrum during the coupling and heating epochs, these fluctuations are quickly washed out at $z \lesssim 13$ (see Fig. 13 and Section 6C in Cruz et al. 2024a).

We next consider the upcoming SKA. In order to estimate the observability of the four models analyzed so far, we perform a similar analysis as in Balu et al. (2023b) that we briefly summarize hereafter. The sensitivity of a radio interferometer is mostly regulated by the thermal noise (Δ_N) and the cosmic variance with the former dominating the noise at small scales and the latter at large scales. The thermal noise is related to the bandwidths of the instrument, beam factor (see Parsons et al. 2014), the integration time of the mode k and the temperature of the system (given as the sum of the sky and receiver temperature) (Morales 2005; McQuinn et al. 2006; Parsons et al. 2012). We can hence write the total noise by summing these two components:

$$\left[\frac{1}{\sigma[\Delta^2_{21}(k)]}\right]^2 = \Sigma_i \left(\frac{1}{\Delta^2_N + \Delta^2_{21}}\right)^2. \tag{5.8}$$

By doing so, we are effectively assuming that the errors are Gaussian distributed, which is reasonable for the relevant scales in this work (Qin et al. 2021a; Prelogović & Mesinger 2023). Finally, a 21cm detection is heavily limited by the ability of removing the fore-

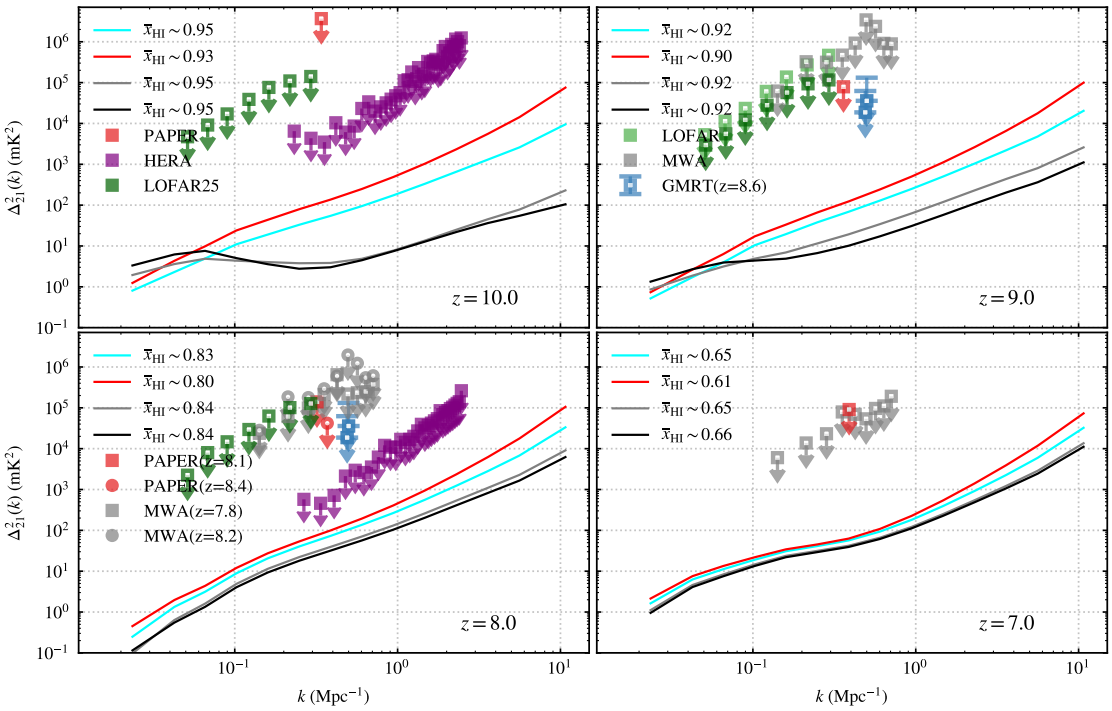

Figure 5.16: 21cm power spectrum at $z = 10, 9, 8$ and 7 as a function of k for different Pop. III star formation models. Color coding as in the previous figures. We show also current upper limits from PAPER at $z = 9.9, 8.7, 8.4, 8.1, 7.5$ (Kolopanis et al. 2019), LOFAR at $z = 10.1, 9.1, 8.3$ (Mertens et al. 2020, 2025), MWA at $z = 8.7, 8.2, 7.8$(Trott et al. 2020), GMRT at $z = 8.6$ (Paciga et al. 2013) and HERA (HERA Collaboration et al. 2023) at $z = 10, 8$.

grounds. We used the python package 21CMSENSE[§] (Pober et al. 2013, 2014) which, given the specifics of an interferometer, a mock 21cm power spectrum and an observational campaign, computes the interferometer sensitivity to the 21cm power spectrum under different assumptions of foreground removals. We used the assumption 'moderate' foreground removals and we focused on the first phase of SKA (i.e. SKA1-low), in particular we included the stations in the 'Central Area' of the SKA1-low[¶], resulting in 296 stations of diameter 35m distributed across a circular area with 1.7 km diameter. We assumed two different observational campaigns: one of 180 hours (six hours per night for 30 days) and another of 1080 hours (six hours per night for 180 days). Additionally, we avoid the modes that are contained within the foreground wedge (Datta et al. 2010) so that effectively we are limited to $k_{\rm min} = 0.16$ Mpc^{-1} for our analysis and $k_{\rm max} = 1.4$ Mpc^{-1} (the latter arises from a combination of the spatial scales that are probed by the SKA1-low and the shot noise from our simulation).

To quantify the detectability of a Pop. III model we compute by how many sigma its power spectrum differs from the one arising from the No Pop. III model:

$$D_i(k) = \frac{\Delta^2_{21,i}(k) - \Delta^2_{21,0}(k)}{\sqrt{\sigma^2[\Delta^2_{21,i}(k)] + \sigma^2[\Delta^2_{21,0}(k)]}}, \tag{5.9}$$

where the subscript i refers to the Pop. III model considered and 0 to the No Pop. III model. To detect a Pop. III model the difference between its power spectrum and the No Pop. III one needs to be at least of 1σ otherwise the model is not detectable. In Fig. 5.17 we show the evolution in redshift of this quantity at $k \sim 0.2$ (upper panel) and $k \sim 0.9$ Mpc^{-1} (lower panel) for each Pop. III model and assuming 1080 (solid lines) and 180 (dashed lines) observation hours. The weak Pop. III model (grey line) is different from the No Pop. III one by less than 1σ both at the small and large scales even with an observation of 1080 hours. The moderate Pop. III model is several σ away from the No Pop. III model at $7 \lesssim z \lesssim 10$ both at the small and large scales with a 1080 hours observation while with a 180 hours the model is detectable only at the large scales where the difference is between 1 and 2 σ. The extreme Pop. III model is the one with

[§] https://github.com/rasg-affiliates/21cmSense

[¶] See the official SKA1 System Baseline Design document in https://www.skao.int/en for further details

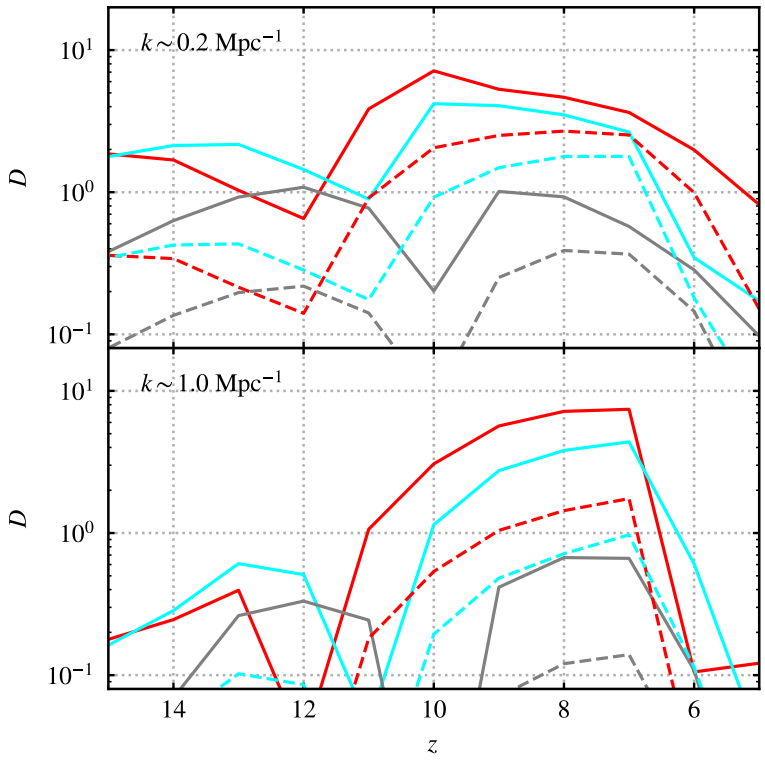

Figure 5.17: Detectability (see Eq. 5.9) vs z for each Pop. III model (color coding as in the previous figures) at $k \sim 0.2$ (upper panel) and 1.0 Mpc^{-1} (lower panel). Solid (dashed) lines assume a 1080 (180) hours observation with SKA1-low.

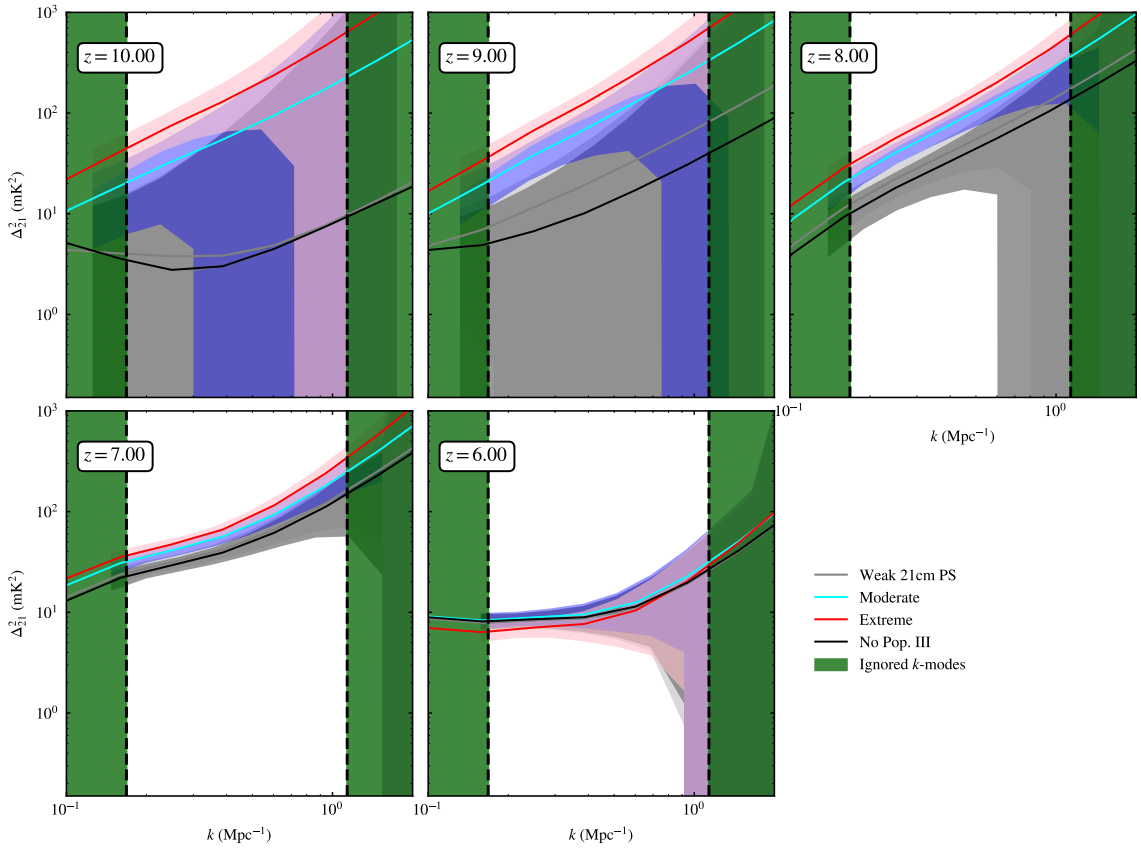

Figure 5.18: The black, grey, red and cyan curves show the 21cm power spectrum from all the models in Table 5.4. The shaded region of the correspondent color represents the sensitivity (including both thermal and cosmic variance noise) to the associated 21cm power spectrum for a 180 hours observation with the upcoming SKA1-low with the 'moderate' foreground removal case. We ignore (green shaded regions) all the k-modes falling within the 21cm foreground wedge (see text for further details).

the largest difference from the No Pop. III model being potentially detectable at both large and small scales even with a 180 hours observations.

Finally, we highlight the differences between each Pop. III model by showing their power spectrum noise (shaded regions) assuming 180 and 1080 hours of observations in Fig. 5.18 and 5.19. Models with stronger X-ray contribution (red and cyan lines) have a power spectrum that differs from the models with no or mild Pop. III contribution (dark and light grey regions) by more than the observational uncertainty. The 1σ region of its power spectrum (pink shaded region) is above the models with no or mild Pop. III contribution at z = 7 and 8 for all the k-modes, at z = 9 at $k \lesssim 0.7$ Mpc^{-1} and at z = 10 only at the largest scales considered ($k \lesssim 0.4$ Mpc^{-1}). With only 180 hours observations however, it is not possible to clearly distinguish between the intermediate and extreme

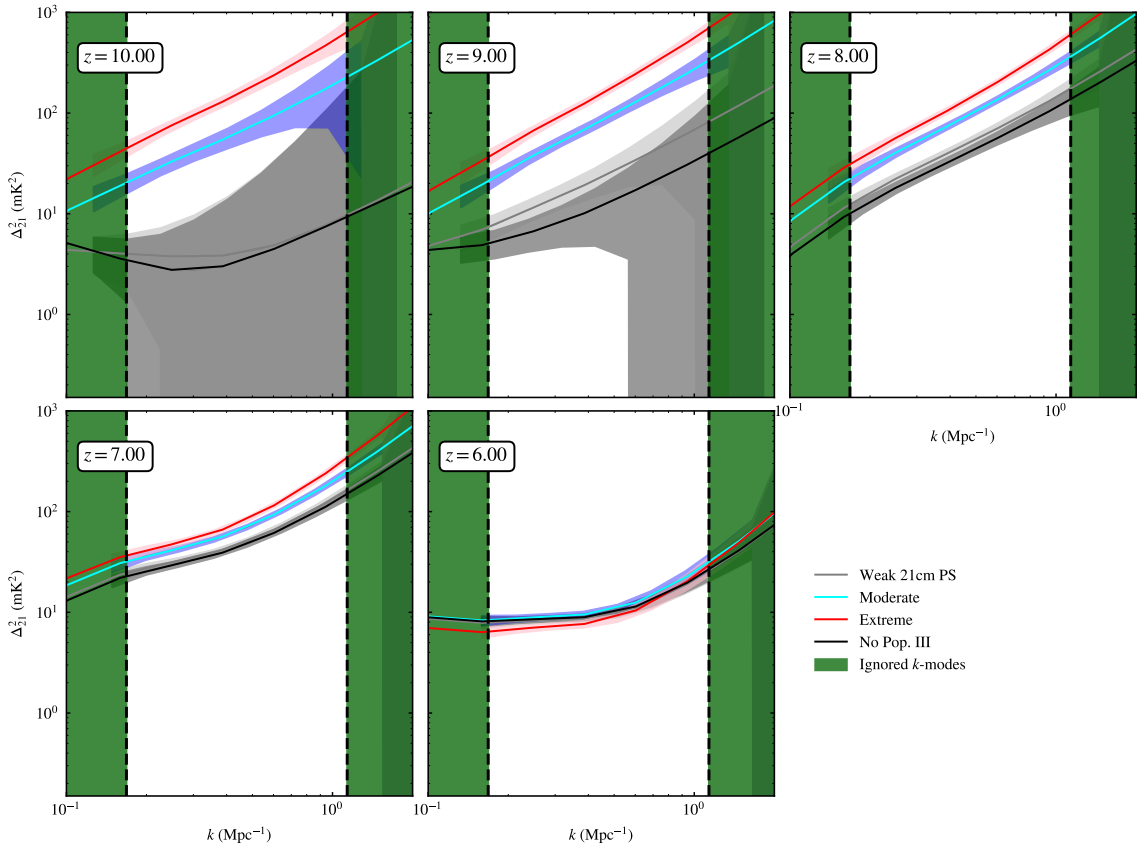

Figure 5.19: Same as Fig. 5.18 but assuming 1080 hours observation.

Pop. III model (blue an pink shaded regions). At $z = 6$ it is not possible to distinguish any of these models since at this redshift the power spectrum is mostly determined by the ionization state of the IGM which is identical for all the four models considered.

The sensitivity greatly improves for an observational campaign of 1000 hours (Fig. 5.19). In this case, models accounting for Pop. III early heating which is stronger than Pop. II are clearly distinguishable from models with no or mild Pop. III contribution. At $z = 10$, 9 and 8, it is even possible to distinguish between intermediate and extreme Pop. III models at all scales within $k_{\rm min}$ and $k_{\rm max}$, indicating that SKA observations of the 21cm power spectrum during the EoR are sensitive to the IGM heating occurred at $z \geq 15$. At $z = 7$, the difference between the various models are less evident but intermediate and extreme Pop. III models still fall outside the uncertainty regions of weak Pop. III and No Pop. III. This indicates that models with a harder Pop. III X-ray emission can be disentangled from models with no or mild Pop. III X-ray emission even at $z = 7$. Also Gessey-Jones et al. (2025) focused on the possibility of detecting difference

Pop. III models using 21cm observations. In their analysis they included both REACH (sensitive to the 21cm global signal) and SKA-Low confirming that an observation of $\sim$ 3000 hours with SKA-Low can constrain the Pop. III IMF due to their difference in the X-ray heating. Finally, we highlight that the impact of Pop. III stars is visible on the power spectrum as long as their X-ray contribution is boosted compared to Pop. II. The differences between the weak Pop. III and the No Pop. III scenario are so small they will not be visible even with 1000 SKA hours. This demonstrates that an upcoming 21cm power spectrum detection will shed light on the properties of the first sources establishing their contribution to the heating of the IGM.

5.6. Conclusions

In this work we investigated how the early ($z \geq 15$) heating of the IGM due to Pop. III stars impacts the 21cm power spectrum during the EoR ($z \leq 10$) which will be observable by the SKA. We developed a framework of scaling relations between Pop. III star formation rate in mini-halos and the density field within the semi-analytical model meraxes that allows us to account for the radiative contribution of mini-halos that cannot be directly resolved in a large (L = 210 h^{-1} cMpc) cosmological simulation. The scaling relations are calibrated on a smaller and higher resolution simulation able to resolve all the mini-halos. We then investigated three Pop. III models each with different IMF, star formation efficiency and specific X-ray luminosity. This formalism is both based on realistic galaxy population and it provides an accurate estimation of the Pop. III backgrounds yielding a computation of the ionization and thermal state of the IGM which is crucial to obtain a reliable estimation of the 21cm signal and power spectrum during the EoR ($z \lesssim 10$). The key results can be summarized as follows:

1. The inclusion of Pop. III stars does not significantly change the EoR history as their main contribution comes from the secondary ionizations from their X-ray emission. As a result, all the models that we considered give reionization histories consistent with the latest constraints on the neutral hydrogen fraction and the Thomson scattering optical depth.

2. As previously known, the evolution of the 21cm global signal during the Cosmic Dawn is significantly impacted by Pop. III stars. In a model where Pop. III and Pop. II have the same X-ray specific luminosity (weak Pop. III) the absorption through of the 21cm global signal is slightly deeper and occurs at higher-z. If instead Pop. III stars have a larger L_X / SFR, the signal is seen in emission at higher-z ($z \sim 14$ for the intermediate Pop. III model and $z \sim 18$ for the extreme Pop. III model).

3. The heating from Pop. III stars significantly increases the 21cm power spectrum during the EoR both at large and small scales. This is more evident for models with an increased specific X-ray luminosity where the difference can be of more than a factor of 4 at $z \gtrsim 7$. This shows that the 21cm power spectrum during the EoR is sensitive to the heating occurred at much higher redshift.

4. Focusing on a possible future detection of the 21cm power spectrum, we estimated the observational uncertainty of each model using the PYTHON package 21CMSENSE assuming an observational campaign with SKA1-low of 180 and 1080 hours respectively. We found that 180 hours are not enough to distinguish different Pop. III models but they already can confirm/exclude the presence of a stronger heating from Pop. III stars at high-z since their power spectra differs by more than 1σ from the No Pop. III model. However, using ~ 1000 hours of SKA, models with a stronger Pop. III contribution (stronger X-ray emission and/or higher Pop. III star formation efficiency) become clearly distinguishable at $z \gtrsim 7$. The power spectrum towards the end of the EoR ($z \lesssim 6$) does not distinguish Pop. III models.

CHAPTER 6

Conclusions

Grazie per gli applausi ma ho scelto l'amore
Questa è la mia vita non dimenticarlo.

Caparezza - La Scelta (2021)

In this thesis I presented a new SAM of galaxy formation and reionization that includes Pop. III star formation and mini-halo physics. Within this model, I have implemented key astrophysical processes such as molecular cooling, LW background, baryon-dark matter streaming velocity, H_2 self-shielding and metal evolution of the IGM in a high-resolution, small (L = $10h^{-1}$ cMpc) simulation. Following the IGM chemical evolution is essential for understanding how galaxies acquire metals. Most of the galaxies are self-enriched by their own star formation as a large fraction of the IGM remains pristine until $z \sim 10$. However, during the EoR, metal bubbles can grow to sizes of ~ 200 ckpc, reaching and contaminating low-mass halos ($M \lesssim 10^8$ $M_\odot$) that otherwise would not get any metals since their star formation is suppressed by photo-ionizing feedback. This has interesting implications for the expected metallicity of DLAs systems at $z \sim 6$ such as the one analysed in Sodini et al. (2024).

This model allowed me to demonstrate that the main parameters that determine the evolution of Pop. III SFRD and the properties of Pop. III star clusters are the IMF, star

formation efficiency and the critical metallicity. The former one is particularly important to determine the luminosity associated with these systems. For a very top-heavy IMF (log-normal centered at 60 $M_\odot$) and for a star formation efficiency similar to the Pop. II one, Pop. III systems of $\sim 10^5$ $M_\odot$ reach UV absolute magnitudes of ~ -18 at $z \sim 16$. Despite the caveat of having a small simulation box, this result supports the idea that JWST's unusually bright high-redshift galaxies could be explained by a top-heavy IMF that boosts the light-to-mass ratio at $z \gtrsim 12$. By $z \sim 12$, Pop. III galaxies are largely subdominant and all the brightest galaxies are Pop. II so the model still matches the observed UV luminosity function at $z \lesssim 12$.

Based on this new SAM, I then developed a framework that allows to estimate the Pop. III star formation in mini-halos within a large simulation box (L = 210 h^{-1} cMpc) that resolve only halos above the atomic cooling threshold. This algorithm is based on building scaling relations between the Pop. III SFR and the dark matter density field. With this model I then computed the 21cm global signal and evolution for different Pop. III models. While metal-free stars primarily influence the sky-averaged signal at $z \gtrsim 15$, their imprint on the power spectrum remains detectable down to $z \sim 7$. Using 21CMSENSE I estimated the 1σ error associated to each power spectrum assuming an observational campaign with SKA-low. With ~ 1000 hours, it is possible to distinguish different models that include Pop. III star formation, provided that their X-ray contribution is at least one order of magnitude higher than the Pop. II one. This demonstrates that a future 21cm detection with SKA-low (or even a non-detection) will place valuable constraints on the nature of the first stars.

6.1. What's next?

It is truly an exciting time to study the nature of the first stars and galaxies. In the first three years of JWST, we are approaching with big steps the first detection of Pop. III stars. It is now evident that numerical simulations are crucial to understand and interpret JWST observations and need to be updated in order to take into account the complex physics of the high-z Universe. In this sense, I am now updating MERAXES in order to follow different phases of the gas disk. This will be used to investigate the late

Pop. III star formation episodes occuring in metal-free pockets at $z \sim 6-10$. This will allow an accurate estimation of the observability of Pop. III stars during the EoR and to understand their origin. Ultimately this will shed light on the Pop. III candidates observed so far.

Even more information will be gathered in the next few years after SKA will finally see its first light. At the time of writing, this radio facility is being built in Western Australia and it is expected to improve the sensitive of one order of magnitude compared to the current state-of-the-art radio interferometers. While we are (hopefully) approaching the first 21cm detection, it is necessary to understand the unique features in the 21cm signal arising from different astrophysical processes. Even if this thesis has contributed to assess the impact of the first stars, other processes are still widely unconstrained. With MERAXES I am now exploring how the burstiness in star formation that has been observed with JWST, affects the 21cm power spectrum.

As we enter the era of precision 21cm cosmology, the combined power of theory and observation brings us closer than ever to unveiling the elusive first stars and their imprint on the cosmic dawn. Hopefully this thesis has taken a small but meaningful step toward this direction.

References

Abbott B. P., et al., 2016, Phys. Rev. Lett., 116, 061102

Abbott R., et al., 2021, ApJ, 913, L7

Abel T., Bryan G. L., Norman M. L., 2000, ApJ, 540, 39

Amati L., et al., 2018, Advances in Space Research, 62, 191

Angulo R. E., Springel V., White S. D. M., Jenkins A., Baugh C. M., Frenk C. S., 2012, MNRAS, 426, 2046

Asplund M., Grevesse N., Sauval A. J., Scott P., 2009, ARA&A, 47, 481

Atek H., et al., 2023, JWST's GLIMPSE: gravitational lensing & NIRCam imaging to probe early galaxy formation and sources of reionization, JWST Proposal. Cycle 2, ID. #3293

Bañados E., et al., 2018, Nature, 553, 473

Balu S., Greig B., Qiu Y., Power C., Qin Y., Mutch S., Wyithe J. S. B., 2023a, MNRAS, 520, 3368

Balu S., Greig B., Wyithe J. S. B., 2023b, MNRAS, 525, 3032

Balu S., Power C., Mutch S., Qin Y., Ventura E. M., 2024, doi:10.5281/zenodo.10608236, https://doi.org/10.5281/zenodo.10608236

Barkana R., Loeb A., 2001, Phys. Rep., 349, 125

Barkana R., Loeb A., 2005, ApJ, 626, 1

Becker R. H., et al., 2001, AJ, 122, 2850

Behling T., Hazlett R., Kulkarni M., Visbal E., 2025, arXiv e-prints, p. arXiv:2508.04808

Bera A., Datta K. K., Samui S., 2020, MNRAS, 498, 918

Bera A., Samui S., Datta K. K., 2023, MNRAS, 519, 4869

Bosman S. E. I., et al., 2022, MNRAS, 514, 55

Bovino S., Galli D., 2019, in Latif M., Schleicher D., eds, , Formation of the First Black Holes. World Scientific Publishing, pp 45–66, doi:10.1142/9789813227958_0003

Bowler R. A. A., McLure R. J., Dunlop J. S., McLeod D. J., Stanway E. R., Eldridge J. J., Jarvis M. J., 2017, MNRAS, 469, 448

Bowman J. D., Rogers A. E. E., Monsalve R. A., Mozdzen T. J., Mahesh N., 2018, Nature, 555, 67–70

Bromm V., 2013, Reports on Progress in Physics, 76, 112901

Bromm V., Coppi P. S., Larson R. B., 1999, ApJ, 527, L5

Bryan G. L., Norman M. L., 1998, ApJ, 495, 80

Bullock J. S., Kolatt T. S., Sigad Y., Somerville R. S., Kravtsov A. V., Klypin A. A., Primack J. R., Dekel A., 2001, MNRAS, 321, 559

Caffau E., et al., 2011, Nature, 477, 67

Carnall A. C., et al., 2023, Nature, 619, 716

Castellano M., et al., 2024, ApJ, 972, 143

Chandro-Gómez Á., et al., 2025, MNRAS, 539, 776

Chardin J., Haehnelt M. G., Aubert D., Puchwein E., 2015, MNRAS, 453, 2943

Charlot S., Fall S. M., 2000, ApJ, 539, 718

Chatterjee A., Dayal P., Choudhury T. R., Schneider R., 2020, MNRAS, 496, 1445

Chiaki G., Wise J. H., 2023, MNRAS, 520, 5077

Chiaki G., Yoshida N., 2022, MNRAS, 510, 5199

Chon S., Omukai K., Schneider R., 2021, MNRAS, 508, 4175

Chon S., Ono H., Omukai K., Schneider R., 2022, MNRAS, 514, 4639

Ciardi B., Salvaterra R., Di Matteo T., 2010, MNRAS, 401, 2635

Cohen A., Fialkov A., Barkana R., Lotem M., 2017, Monthly Notices of the Royal Astronomical Society, 472, 1915

Cole S., Lacey C. G., Baugh C. M., Frenk C. S., 2000, MNRAS, 319, 168

Croton D. J., et al., 2016, ApJS, 222, 22

Cruz H. A. G., Munoz J. B., Sabti N., Kamionkowski M., 2024a, arXiv e-prints, p. arXiv:2407.18294

Cruz H. A. G., Adi T., Flitter J., Kamionkowski M., Kovetz E. D., 2024b, Phys. Rev. D, 109, 023518

Cucchiara A., et al., 2011, ApJ, 736, 7

D'Odorico V., et al., 2023, MNRAS, 523, 1399

Das A., Mesinger A., Pallottini A., Ferrara A., Wise J. H., 2017, MNRAS, 469, 1166

Datta A., Bowman J. D., Carilli C. L., 2010, The Astrophysical Journal, 724, 526

Davies F. B., et al., 2018, The Astrophysical Journal, 864, 142

Dekel A., Sarkar K. C., Birnboim Y., Mandelker N., Li Z., 2023, MNRAS, 523, 3201

Dijkstra M., Haiman Z., Rees M. J., Weinberg D. H., 2004, ApJ, 601, 666

Dijkstra M., Haiman Z., Mesinger A., Wyithe J. S. B., 2008, MNRAS, 391, 1961

Dijkstra M., Ferrara A., Mesinger A., 2014, MNRAS, 442, 2036

Donnan C. T., et al., 2023, MNRAS, 518, 6011

Eide M. B., Graziani L., Ciardi B., Feng Y., Kakiichi K., Di Matteo T., 2018, MNRAS, 476, 1174

Eide M. B., Ciardi B., Graziani L., Busch P., Feng Y., Di Matteo T., 2020, MNRAS, 498, 6083

Einasto J., 1965, Trudy Astrofizicheskogo Instituta Alma-Ata, 5, 87

Eisenstein D. J., et al., 2005, ApJ, 633, 560

Elahi P. J., Cañas R., Poulton R. J. J., Tobar R. J., Willis J. S., Lagos C. d. P., Power C., Robotham A. S. G., 2019a, PASA, 36, e021

Elahi P. J., Poulton R. J. J., Tobar R. J., Cañas R., Lagos C. d. P., Power C., Robotham A. S. G., 2019b, PASA, 36, e028

Facchinetti G., Lopez-Honorez L., Qin Y., Mesinger A., 2024, J. Cosmology Astropart. Phys., 2024, 005

Fan X., Carilli C. L., Keating B., 2006, ARA&A, 44, 415

Farmer R., Renzo M., de Mink S. E., Marchant P., Justham S., 2019, ApJ, 887, 53

Feathers C. R., Visbal E., Kulkarni M., Hazlett R., 2023, arXiv e-prints, p. arXiv:2306.07371

Feathers C. R., Kulkarni M., Visbal E., Hazlett R., 2024, ApJ, 962, 62

Feathers C. R., Kulkarni M., Visbal E., 2025, J. Cosmology Astropart. Phys., 2025, 043

Ferrara A., Pallottini A., Dayal P., 2023, MNRAS, 522, 3986

Fialkov A., Barkana R., Tseliakhovich D., Hirata C. M., 2012, MNRAS, 424, 1335

Finkelstein S. L., et al., 2012, ApJ, 756, 164

Fragos T., et al., 2013, ApJ, 764, 41

Frebel A., Norris J. E., 2015, ARA&A, 53, 631

Fujimoto S., et al., 2025a, Vast Exploration for Nascent, Unexplored Sources (VENUS), JWST Proposal. Cycle 4, ID. #6882

Fujimoto S., et al., 2025b, arXiv e-prints, p. arXiv:2501.11678

Fukushima H., Yajima H., Sugimura K., Hosokawa T., Omukai K., Matsumoto T., 2020, MNRAS, 497, 3830

Furlanetto S. R., 2006, MNRAS, 371, 867–878

Furlanetto S. R., Loeb A., 2003, ApJ, 588, 18

Furlanetto S. R., Zaldarriaga M., Hernquist L., 2004, ApJ, 613, 1

Furlanetto S. R., Peng Oh S., Briggs F. H., 2006, Physics Reports, 433, 181–301

Gabrielpillai A., Somerville R. S., Genel S., Rodriguez-Gomez V., Pandya V., Yung L. Y. A., Hernquist L., 2022, MNRAS, 517, 6091

Galli D., Palla F., 1998, A&A, 335, 403

Gamow G., Teller E., 1939, Phys. Rev., 55, 654

Gelli V., Mason C., Hayward C. C., 2024, ApJ, 975, 192

Genel S., et al., 2014, Monthly Notices of the Royal Astronomical Society, 445, 175

Gessey-Jones T., et al., 2022, MNRAS, 516, 841

Gessey-Jones T., et al., 2025, arXiv e-prints, p. arXiv:2502.18098

Ghara R., Mellema G., Giri S. K., Choudhury T. R., Datta K. K., Majumdar S., 2018, MNRAS, 476, 1741

Gnedin N. Y., 2014, ApJ, 793, 29

Gnedin N. Y., Hui L., 1998, MNRAS, 296, 44

Gnedin N. Y., Madau P., 2022, Living Reviews in Computational Astrophysics, 8, 3

Gnedin N. Y., Shaver P. A., 2004, ApJ, 608, 611

Greif T. H., 2015, Computational Astrophysics and Cosmology, 2, 3

Greif T. H., Johnson J. L., Klessen R. S., Bromm V., 2008, MNRAS, 387, 1021

Greif T. H., White S. D. M., Klessen R. S., Springel V., 2011a, ApJ, 736, 147

Greif T. H., Springel V., White S. D. M., Glover S. C. O., Clark P. C., Smith R. J., Klessen R. S., Bromm V., 2011b, ApJ, 737, 75

Greig B., Mesinger A., Davies F. B., Wang F., Yang J., Hennawi J. F., 2022, Monthly Notices of the Royal Astronomical Society, 512, 5390

Gunn J. E., Gott III J. R., 1972, ApJ, 176, 1

Gunn J. E., Peterson B. A., 1965, ApJ, 142, 1633

HERA Collaboration et al., 2023, ApJ, 945, 124

Haiman Z., Bryan G. L., 2006, ApJ, 650, 7

Haiman Z., Abel T., Rees M. J., 2000, ApJ, 534, 11

Harikane Y., et al., 2023, ApJS, 265, 5

Harrison E. R., 1970, Phys. Rev. D, 1, 2726

Hartwig T., Bromm V., Klessen R. S., Glover S. C. O., 2015a, MNRAS, 447, 3892

Hartwig T., Glover S. C. O., Klessen R. S., Latif M. A., Volonteri M., 2015b, MNRAS, 452, 1233

Hartwig T., et al., 2018a, MNRAS, 478, 1795

Hartwig T., Bromm V., Loeb A., 2018b, MNRAS, 479, 2202

Hazlett R., Kulkarni M., Visbal E., Wise J. H., 2024, arXiv e-prints, p. arXiv:2403.05624

Hegde S., Furlanetto S. R., 2023, MNRAS, 525, 428

Hegde S., Furlanetto S. R., 2025, arXiv e-prints, p. arXiv:2507.19581

Hegde S., Wyatt M. M., Furlanetto S. R., 2024, J. Cosmology Astropart. Phys., 2024, 025

Heger A., Woosley S. E., 2002, ApJ, 567, 532

Heger A., Woosley S. E., 2010, ApJ, 724, 341

Henriques B. M. B., White S. D. M., Thomas P. A., Angulo R., Guo Q., Lemson G., Springel V., Overzier R., 2015, MNRAS, 451, 2663

Hirano S., Hosokawa T., Yoshida N., Umeda H., Omukai K., Chiaki G., Yorke H. W., 2014, ApJ, 781, 60

Hirano S., Hosokawa T., Yoshida N., Omukai K., Yorke H. W., 2015, MNRAS, 448, 568

Hirano S., Yoshida N., Sakurai Y., Fujii M. S., 2018, ApJ, 855, 17

Hoag A., et al., 2019, The Astrophysical Journal, 878, 12

Hou L., Mack K. J., 2024, arXiv e-prints, p. arXiv:2411.10626

Iliev I. T., Mellema G., Pen U. L., Merz H., Shapiro P. R., Alvarez M. A., 2006, MNRAS, 369, 1625

Iliev I. T., Mellema G., Ahn K., Shapiro P. R., Mao Y., Pen U.-L., 2014, MNRAS, 439, 725

Jaacks J., Thompson R., Finkelstein S. L., Bromm V., 2018, MNRAS, 475, 4396

Jaura O., Glover S. C. O., Wollenberg K. M. J., Klessen R. S., Geen S., Haemmerlé L., 2022, MNRAS, 512, 116

Jeans J. H., 1902, Philosophical Transactions of the Royal Society of London Series A, 199, 1

Jeena S. K., Banerjee P., 2024, The Open Journal of Astrophysics, 7, 83

Jin X., et al., 2023, The Astrophysical Journal, 942, 59

Johnson J. L., Dalla Vecchia C., Khochfar S., 2013, MNRAS, 428, 1857

Jung I., et al., 2020, ApJ, 904, 144

Kannan R., Garaldi E., Smith A., Pakmor R., Springel V., Vogelsberger M., Hernquist L., 2022, MNRAS, 511, 4005

Kauffmann G., 1996, MNRAS, 281, 475

Kaur H. D., Gillet N., Mesinger A., 2020, MNRAS, 495, 2354

Kaur H. D., Qin Y., Mesinger A., Pallottini A., Fragos T., Basu-Zych A., 2022, MNRAS, 513, 5097

Keller S. C., et al., 2014, Nature, 506, 463

Kennicutt Robert C. J., 1998, ApJ, 498, 541

Kennicutt Robert C. J., De Los Reyes M. A. C., 2021, ApJ, 908, 61

Klessen R. S., Glover S. C. O., 2023, ARA&A, 61, 65

Knebe A., et al., 2011, Monthly Notices of the Royal Astronomical Society, 415, 2293

Kobayashi C., Karakas A. I., Lugaro M., 2020, ApJ, 900, 179

Kokorev V., et al., 2025, ApJ, 983, L22

Kolb E. W., Turner M. S., 1990, The early universe. Boca Raton

Kolopanis M., et al., 2019, ApJ, 883, 133

Kroupa P., 2001, MNRAS, 322, 231

Kuhlen M., Faucher-Giguère C.-A., 2012, MNRAS, 423, 862

Kulkarni M., Visbal E., Bryan G. L., 2021, ApJ, 917, 40

Labbé I., et al., 2023, Nature, 616, 266

Lacey C., Cole S., 1993, MNRAS, 262, 627

Lagae C., Amarsi A. M., Rodríguez Díaz L. F., Lind K., Nordlander T., Hansen T. T., Heger A., 2023, A&A, 672, A90

Latif M. A., Whalen D., Khochfar S., 2022, ApJ, 925, 28

Lazar A., Bromm V., 2022, MNRAS, 511, 2505

Leitherer C., et al., 1999, ApJS, 123, 3

Liu A., Shaw J. R., 2020, Publications of the Astronomical Society of the Pacific, 132, 062001

Liu H., Slatyer T. R., 2018, Phys. Rev. D, 98, 023501

Liu B., et al., 2024, MNRAS, 534, 1634

Ma Q.-B., Ciardi B., Eide M. B., Busch P., Mao Y., Zhi Q.-J., 2021, ApJ, 912, 143

Madau P., Fragos T., 2017, ApJ, 840, 39

Magg M., Hartwig T., Agarwal B., Frebel A., Glover S. C. O., Griffen B. F., Klessen R. S., 2018, MNRAS, 473, 5308

Magg M., et al., 2022, MNRAS, 514, 4433

Maio U., Viel M., 2015, MNRAS, 446, 2760

Maiolino R., et al., 2024, A&A, 687, A67

Maity B., Choudhury T. R., 2022, MNRAS, 511, 2239

Mapelli M., Ferrara A., Rea N., 2006, MNRAS, 368, 1340

Marshall M. A., Mutch S. J., Qin Y., Poole G. B., Wyithe J. S. B., 2019, MNRAS, 488, 1941

Mason C. A., et al., 2019, Monthly Notices of the Royal Astronomical Society, 485, 3947

Matthee J., et al., 2017, ApJ, 851, 145

McGreer I. D., Mesinger A., D'Odorico V., 2015, MNRAS, 447, 499

McQuinn M., Zahn O., Zaldarriaga M., Hernquist L., Furlanetto S. R., 2006, ApJ, 653, 815

Mebane R. H., Mirocha J., Furlanetto S. R., 2018, MNRAS, 479, 4544

Mebane R. H., Mirocha J., Furlanetto S. R., 2020, MNRAS, 493, 1217

Mertens F. G., et al., 2020, MNRAS, 493, 1662

Mertens F. G., et al., 2025, arXiv e-prints, p. arXiv:2503.05576

Mesinger A., Furlanetto S., Cen R., 2011, MNRAS, 411, 955

Mesinger A., Aykutalp A., Vanzella E., Pentericci L., Ferrara A., Dijkstra M., 2014, Monthly Notices of the Royal Astronomical Society, 446, 566

Minoda T., Tashiro H., Takahashi T., 2019, MNRAS, 488, 2001

Miralda-Escudé J., Haehnelt M., Rees M. J., 2000, ApJ, 530, 1

Mittal S., Kulkarni G., 2021, MNRAS, 503, 4264

Mo H., van den Bosch F. C., White S., 2010, Galaxy Formation and Evolution. Cambridge University Press, doi:10.1017/CBO9780511807244

Mocz P., et al., 2020, MNRAS, 494, 2027

Molaro M., Davé R., Hassan S., Santos M. G., Finlator K., 2019, MNRAS, 489, 5594

Morales M. F., 2005, The Astrophysical Journal, 619, 678

Morales M. F., Wyithe J. S. B., 2010, ARA&A, 48, 127

Moriya T. J., Quimby R. M., Robertson B. E., 2022, ApJ, 925, 211

Muñoz J. B., 2023, MNRAS, 523, 2587

Muñoz J. B., Qin Y., Mesinger A., Murray S. G., Greig B., Mason C., 2022, MNRAS, 511, 3657

Muñoz J. B., Mirocha J., Chisholm J., Furlanetto S. R., Mason C., 2024, MNRAS, 535, L37

Murray S., Greig B., Mesinger A., Muñoz J., Qin Y., Park J., Watkinson C., 2020, The Journal of Open Source Software, 5, 2582

Mutch S. J., Geil P. M., Poole G. B., Angel P. W., Duffy A. R., Mesinger A., Wyithe J. S. B., 2016, MNRAS, 462, 250

Mutch S. J., Greig B., Qin Y., Poole G. B., Wyithe J. S. B., 2023, arXiv e-prints, p. arXiv:2303.07378

Mutch S. J., Greig B., Qin Y., Poole G. B., Wyithe J. S. B., 2024, MNRAS, 527, 7924

Naidu R. P., et al., 2025, arXiv e-prints, p. arXiv:2505.11263

Naoz S., Barkana R., 2007, MNRAS, 377, 667

Naoz S., Yoshida N., Gnedin N. Y., 2013, ApJ, 763, 27

Navarro J. F., Frenk C. S., White S. D. M., 1996, ApJ, 462, 563

Nebrin O., Giri S. K., Mellema G., 2023, MNRAS, 524, 2290

Nordlander T., et al., 2019, MNRAS, 488, L109

Nunhokee C. D., et al., 2025, arXiv e-prints, p. arXiv:2505.09097

Ocvirk P., et al., 2020, MNRAS, 496, 4087

Oh S. P., Haiman Z., 2002, ApJ, 569, 558

Omukai K., Nishi R., 1998, ApJ, 508, 141

Ouchi M., et al., 2010, ApJ, 723, 869

Paciga G., et al., 2013, MNRAS, 433, 639

Padmanabhan H., Loeb A., 2023, ApJ, 953, L4

Pallottini A., Ferrara A., Gallerani S., Salvadori S., D'Odorico V., 2014, MNRAS, 440, 2498

Parashari P., Laha R., 2023, MNRAS, 526, L63

Park J., Ricotti M., Sugimura K., 2021, MNRAS, 508, 6176

Parkinson H., Cole S., Helly J., 2008, MNRAS, 383, 557

Parsons A., Pober J., McQuinn M., Jacobs D., Aguirre J., 2012, ApJ, 753, 81

Parsons A. R., et al., 2014, The Astrophysical Journal, 788, 106

Peebles P. J. E., 1980, The large-scale structure of the universe. Princeton University Press

Pérez-González P. G., et al., 2023, ApJ, 951, L1

Planck Collaboration et al., 2016, A&A, 594, A13

Planck Collaboration et al., 2020, A&A, 641, A6

Pober J. C., et al., 2013, ApJ, 768, L36

Pober J. C., et al., 2014, ApJ, 788, 96

Prelogović D., Mesinger A., 2023, Monthly Notices of the Royal Astronomical Society, 524, 4239

Press W. H., Schechter P., 1974, ApJ, 187, 425

Pritchard J. R., Loeb A., 2012, Reports on Progress in Physics, 75, 086901

Prole L. R., Clark P. C., Klessen R. S., Glover S. C. O., 2022, MNRAS, 510, 4019

Qin Y., et al., 2017, MNRAS, 472, 2009

Qin Y., Mesinger A., Park J., Greig B., Muñoz J. B., 2020, MNRAS, 495, 123

Qin Y., Mesinger A., Bosman S. E. I., Viel M., 2021a, MNRAS, 506, 2390

Qin Y., Mesinger A., Bosman S. E. I., Viel M., 2021b, Monthly Notices of the Royal Astronomical Society, 506, 2390

Qin Y., Balu S., Wyithe J. S. B., 2023, MNRAS, 526, 1324

Qin Y., et al., 2024, arXiv e-prints, p. arXiv:2412.00799

Qiu Y., Mutch S. J., da Cunha E., Poole G. B., Wyithe J. S. B., 2019, MNRAS, 489, 1357

Raiter A., Schaerer D., Fosbury R. A. E., 2010, A&A, 523, A64

Reis I., Fialkov A., Barkana R., 2021, MNRAS, 506, 5479

Ricotti M., 2016, MNRAS, 462, 601

Robertson H. P., 1935, ApJ, 82, 284

Robertson B. E., Ellis R. S., Furlanetto S. R., Dunlop J. S., 2015, ApJ, 802, L19

Rosdahl J., et al., 2018, MNRAS, 479, 994

Rossi M., Salvadori S., Skúladóttir Á., 2021, MNRAS, 503, 6026

Salvadori S., Ferrara A., Schneider R., Scannapieco E., Kawata D., 2010, MNRAS, 401, L5

Santoliquido F., Mapelli M., Iorio G., Costa G., Glover S. C. O., Hartwig T., Klessen R. S., Merli L., 2023, MNRAS, 524, 307

Santos M., Ferramacho L., Silva M., Amblard A., Cooray A., 2010, SimFast21: Simulation of the Cosmological 21cm Signal, Astrophysics Source Code Library, record ascl:1010.025

Sarmento R., Scannapieco E., 2022, ApJ, 935, 174

Sarmento R., Scannapieco E., Cohen S., 2018, ApJ, 854, 75

Sartorio N. S., et al., 2023, MNRAS, 521, 4039

Sassano F., Schneider R., Valiante R., Inayoshi K., Chon S., Omukai K., Mayer L., Capelo P. R., 2021, MNRAS, 506, 613

Saxena A., et al., 2024, A&A, 684, A84

Schaerer D., 2002, A&A, 382, 28

Schaller M., Gonnet P., Draper P. W., Chalk A. B. G., Bower R. G., Willis J., Hausammann L., 2018, SWIFT: SPH With Inter-dependent Fine-grained Tasking, Astrophysics Source Code Library, record ascl:1805.020 (ascl:1805.020)

Schauer A. T. P., Drory N., Bromm V., 2020, ApJ, 904, 145

Schauer A. T. P., Glover S. C. O., Klessen R. S., Clark P., 2021, MNRAS, 507, 1775

Schaye J., et al., 2014, Monthly Notices of the Royal Astronomical Society, 446, 521

Schneider R., Omukai K., Inoue A. K., Ferrara A., 2006, MNRAS, 369, 1437

Schneider R., Omukai K., Bianchi S., Valiante R., 2012, MNRAS, 419, 1566

Seta A., Federrath C., 2021, Physical Review Fluids, 6, 103701

Sharda P., Federrath C., Krumholz M. R., Schleicher D. R. G., 2021, MNRAS, 503, 2014

Shen X., Vogelsberger M., Boylan-Kolchin M., Tacchella S., Kannan R., 2023, MNRAS, 525, 3254

Sheth R. K., Mo H. J., Tormen G., 2001, MNRAS, 323, 1

Sims P. H., Pober J. C., 2019, MNRAS, 492, 22

Singh S., et al., 2022, Nature Astronomy, 6, 607

Skinner D., Wise J. H., 2020, MNRAS, 492, 4386

Skúladóttir Á., Koutsouridou I., Vanni I., Amarsi A. M., Lucchesi R., Salvadori S., Aguado D. S., 2024, ApJ, 968, L23

Smidt J., Whalen D. J., Chatzopoulos E., Wiggins B., Chen K.-J., Kozyreva A., Even W., 2015, ApJ, 805, 44

Smith B. D., Wise J. H., O'Shea B. W., Norman M. L., Khochfar S., 2015, MNRAS, 452, 2822

Sobacchi E., Mesinger A., 2013, MNRAS, 432, 3340

Sobacchi E., Mesinger A., 2014, MNRAS, 440, 1662

Sobral D., Matthee J., Darvish B., Schaerer D., Mobasher B., Röttgering H. J. A., Santos S., Hemmati S., 2015, ApJ, 808, 139

Sodini A., et al., 2024, A&A, 687, A314

Somerville R. S., Davé R., 2015, ARA&A, 53, 51

Somerville R. S., Yung L. Y. A., Lancaster L., Menon S., Sommovigo L., Finkelstein S. L., 2025, arXiv e-prints, p. arXiv:2505.05442

Spina B., Bosman S. E. I., Davies F. B., Gaikwad P., Zhu Y., 2024, A&A, 688, L26

Springel V., et al., 2017, Monthly Notices of the Royal Astronomical Society, 475, 676

Stacy A., Bromm V., 2013, MNRAS, 433, 1094

Stacy A., Bromm V., Loeb A., 2011, ApJ, 730, L1

Stacy A., Bromm V., Lee A. T., 2016, MNRAS, 462, 1307

Stecher T. P., Williams D. A., 1967, ApJ, 149, L29

Sugimura K., Matsumoto T., Hosokawa T., Hirano S., Omukai K., 2020, ApJ, 892, L14

Sun G., Faucher-Giguère C.-A., Hayward C. C., Shen X., 2023, MNRAS, 526, 2665

Sutherland R. S., Dopita M. A., 1993, ApJS, 88, 253

Tanaka S. J., Chiaki G., Tominaga N., Susa H., 2017, ApJ, 844, 137

Tanvir N. R., et al., 2009, Nature, 461, 1254

Tegmark M., Silk J., Rees M. J., Blanchard A., Abel T., Palla F., 1997, ApJ, 474, 1

Tinker J., Kravtsov A. V., Klypin A., Abazajian K., Warren M., Yepes G., Gottlöber S., Holz D. E., 2008, ApJ, 688, 709

Toma K., Yoon S.-C., Bromm V., 2016, Space Sci. Rev., 202, 159

Totani T., et al., 2014, PASJ, 66, 63

Trac H., Chen N., Holst I., Alvarez M. A., Cen R., 2022, ApJ, 927, 186

Trenti M., Stiavelli M., 2009, ApJ, 694, 879

Trenti M., Stiavelli M., Shull J. M., 2009, ApJ, 700, 1672

Trinca A., Schneider R., Valiante R., Graziani L., Zappacosta L., Shankar F., 2022, MNRAS, 511, 616

Trinca A., Schneider R., Valiante R., Graziani L., Ferrotti A., Omukai K., Chon S., 2023, arXiv e-prints, p. arXiv:2305.04944

Trott C. M., et al., 2020, MNRAS, 493, 4711

Trussler J. A. A., et al., 2023, MNRAS, 525, 5328

Tseliakhovich D., Hirata C., 2010, Phys. Rev. D, 82, 083520

Tumlinson J., 2006, ApJ, 641, 1

Umeda H., Ouchi M., Nakajima K., Harikane Y., Ono Y., Xu Y., Isobe Y., Zhang Y., 2024, ApJ, 971, 124

Vanzella E., et al., 2023, A&A, 678, A173

Venditti A., Graziani L., Schneider R., Pentericci L., Di Cesare C., Maio U., Omukai K., 2023, MNRAS, 522, 3809

Venditti A., Bromm V., Finkelstein S. L., Graziani L., Schneider R., 2024, MNRAS, 527, 5102

Venditti A., Munoz J. B., Bromm V., Fujimoto S., Finkelstein S. L., Chisholm J., 2025, arXiv e-prints, p. arXiv:2505.20263

Ventura E. M., Trinca A., Schneider R., Graziani L., Valiante R., Wyithe J. S. B., 2023, MNRAS, 520, 3609

Ventura E. M., Qin Y., Balu S., Wyithe J. S. B., 2024, MNRAS, 529, 628

Visbal E., Haiman Z., Bryan G. L., 2015, MNRAS, 453, 4456

Visbal E., Haiman Z., Bryan G. L., 2018, MNRAS, 475, 5246

Visbal E., Bryan G. L., Haiman Z., 2020, ApJ, 897, 95

Walker A. G., 1937, Proceedings of the London Mathematical Society, s2-42, 90

Wang F., et al., 2020, ApJ, 896, 23

Wang X., et al., 2024, ApJ, 967, L42

Watson W. A., Iliev I. T., D'Aloisio A., Knebe A., Shapiro P. R., Yepes G., 2013, MNRAS, 433, 1230

Welch B., et al., 2022, Nature, 603, 815

Whalen D. J., et al., 2013, ApJ, 777, 110

White S. D. M., Frenk C. S., 1991, ApJ, 379, 52

White S. D. M., Rees M. J., 1978, MNRAS, 183, 341

Whitler L. R., Mason C. A., Ren K., Dijkstra M., Mesinger A., Pentericci L., Trenti M., Treu T., 2020, Monthly Notices of the Royal Astronomical Society, 495, 3602

Wise J. H., Abel T., 2008, ApJ, 685, 40

Witstok J., et al., 2025, Nature, 639, 897

Wollenberg K. M. J., Glover S. C. O., Clark P. C., Klessen R. S., 2020, MNRAS, 494, 1871

Woosley S. E., 2017, ApJ, 836, 244

Wouthuysen S. A., 1952, AJ, 57, 31

Xing Q.-F., et al., 2023, Nature, 618, 712

Xu H., Norman M. L., O'Shea B. W., Wise J. H., 2016, ApJ, 823, 140

Xu Y., Yue B., Chen X., 2017, ApJ, 844, 117

Yamaguchi N., Furlanetto S. R., Trapp A. C., 2023, MNRAS, 520, 2922

Yoon S. C., Dierks A., Langer N., 2012, A&A, 542, A113

Yoshida N., Abel T., Hernquist L., Sugiyama N., 2003, ApJ, 592, 645

Yung L. Y. A., Somerville R. S., Finkelstein S. L., Wilkins S. M., Gardner J. P., 2023, MNRAS,

Yung L. Y. A., Somerville R. S., Iyer K. G., 2025, arXiv e-prints, p. arXiv:2504.18618

Zackrisson E., Rydberg C.-E., Schaerer D., Östlin G., Tuli M., 2011, ApJ, 740, 13

Zackrisson E., et al., 2024, MNRAS, 533, 2727

Zeldovich Y. B., 1972, MNRAS, 160, 1P

Zier O., et al., 2025, arXiv e-prints, p. arXiv:2503.03806

Šoltinský T., Kulkarni G., Tendulkar S. P., Bolton J. S., 2025, MNRAS, 537, 364